

Southern Methodist University

SMU Scholar

Electrical Engineering Theses and Dissertations

Electrical Engineering

Spring 5-14-2022

Closed-Loop Brain-Computer Interfaces for Memory Restoration Using Deep Brain Stimulation

David Xiaoliang Wang

Southern Methodist University, xiaoliangw@smu.edu

Follow this and additional works at: https://scholar.smu.edu/engineering_electrical_etds



Part of the [Bioelectrical and Neuroengineering Commons](#), [Biomedical Commons](#), [Cognitive Neuroscience Commons](#), [Computational Neuroscience Commons](#), [Controls and Control Theory Commons](#), and the [Signal Processing Commons](#)

Recommended Citation

Wang, David Xiaoliang, "Closed-Loop Brain-Computer Interfaces for Memory Restoration Using Deep Brain Stimulation" (2022). *Electrical Engineering Theses and Dissertations*. 50.
https://scholar.smu.edu/engineering_electrical_etds/50

This Dissertation is brought to you for free and open access by the Electrical Engineering at SMU Scholar. It has been accepted for inclusion in Electrical Engineering Theses and Dissertations by an authorized administrator of SMU Scholar. For more information, please visit <http://digitalrepository.smu.edu>.

CLOSED-LOOP BRAIN-COMPUTER INTERFACES FOR MEMORY RESTORATION
USING DEEP BRAIN STIMULATION

Approved by:

DocuSigned by:

Carlos Davila

9C9215A8605C485...

Dr. Carlos E. Davila
Associate Professor

DocuSigned by:

Kevin Brenner

E984E3C43B3F43B...

Dr. Kevin Brenner
Assistant Professor

DocuSigned by:

Jungchih Chiao

B472692F696347E...

Dr. Jung-Chih Chiao
Mary and Richard Templeton Centennial
Chair Professor

DocuSigned by:

Bradley C. Lega

BC413E3AF5C1496...

Dr. Bradley C. Lega
Associate Professor

DocuSigned by:

Dinesh Rajan

EF0377D1F04E4D2...

Dr. Dinesh Rajan
Department Chair and Professor

CLOSED-LOOP BRAIN-COMPUTER INTERFACES FOR MEMORY RESTORATION
USING DEEP BRAIN STIMULATION

A Dissertation Presented to the Graduate Faculty of the

Bobby B. Lyle School of Engineering

Southern Methodist University

in

Partial Fulfillment of the Requirements

for the degree of

Doctor of Philosophy

with a

Major in Electrical Engineering

by

David Xiaoliang Wang

M.S., Electrical Engineering, Southern Methodist University
B.Eng., Telecommunication Engineering, Beijing Union University

May 14, 2022

Copyright (2022)

David Xiaoliang Wang

All Rights Reserved

ACKNOWLEDGMENTS

I was a third-string dreamer on a second-place team

But I was hell on wheels with a full head of steam

When coach put me in

And I'm still proud of that hit

...

And that might not mean much to you

But it does to me (1-10)

—Luke Combs, “Does To Me”

I cannot express enough thanks to my advisor, mentor, coach, and lifelong friend - Dr. Carlos Davila for his remarkable guidance and tutelage throughout my entire graduate study career. It seems yesterday we were having lunch on a campus bench talking about science and life when I first got here but it has been years, indeed. His knowledge, kindness and encouragement accompanied my journey all these years. I cannot describe how grateful I am to my co-advisor, mentor, boss, and role model - Dr. Bradley Lega for bringing me to the world of neuroscience. Working with him feels like the morning mountain breeze in a blazing summer day. His professionalism, ingenuity, and enormous trust empowered me to face all the challenges and undoubtedly uplifted my rapid growth. I am highly obliged to my committee member and the Department Chair - Dr. Dinesh Rajan for the admission and funding of my Ph.D. program. This gratitude extends to my rest of committee members - Dr. Jungchih Chiao and Dr. Kevin Brenner for letting me focus on my research. I want to thank all my committee members for their time, dedication, and constructive comments in shaping this dissertation. Needless to say, I feel privileged to be a part of Southern Methodist University

and the UT Southwestern Medical Center communities. I wish to thank all the faculty and staff members for their help day in and day out, especially Mrs. Christy Ahsanullah, who is one of the nicest people I ever met, for saving my butt countless times. I must shout out to all the past and current members of the Lega Lab for their immeasurable contributions and all the memorable moments we had. For sure, they rock!

I was the first man standing next to my best friend

The day the love of his life said "I do" to him

I was a couple beers deep

But I still remembered that speech

And that might not mean much to you

But it does to me (23-28)

I am lucky to be surrounded by a group of great friends. I do not remember how many times my pain was cured by those hunting and camping trips, barbeque parties, and deep conversations. The support and love from my brothers and sisters from another mother mean a world to me. My friends are amazing treasures that I am proud of, and I too am gratified, from the bottom of my heart, for their progress in life. I am thankful to my cute and beloved doggo, Sake the Shredder, for delighting my life. A day is not completed without him messily goofing around in the morning and his lovely gentle cuddles at night.

There's a worn-out blade that my Granddaddy gave me

My Mama's first Bible, Daddy's Don Williams vinyl

That first-fish-catching Zebco thirty-three

Well, that might not mean much to you

But it does to me (37-41)

I am forever indebted to my family for unconditional love and support, as well as for being my biggest fan ever since day one. Never has my family ever questioned about my talent and capability even occasionally I did. I am proud that I inherited the spiritual inspiration from generations of exploration and endeavor of my family. I appreciate their enlightenment, sacrifices and that best gift one person can ever ask for. I carry on our crest and rejuvenate our family's glory.

And I'm a damn hard working

One thing's for certain

I stand up for what I believe

And that might not mean much to you

But it does to me (48-52)

Certainly, I must take a time to recognize myself for being who I am and persisting in what I believe, even in the hardest time. Funny how it is my 30th birthday writing this, and I am more than thrilled to receive this precious present for all the hardship and endeavor. When I look back, it all pays off. It is not about the Ph.D. degree or how hard I was punched in the face by life; it is all about how I stood right up and struck back then moved forward. I sure am proud of myself that I did not compromise or surrender in chasing my dreams because giving in or giving up was never an option, ever. I am proud to say "life sometimes is tough but I always am tougher".

Wang, David Xiaoliang M.S., Electrical Engineering, Southern Methodist University
B.Eng., Telecommunication Engineering, Beijing Union University

Closed-Loop Brain-Computer Interfaces for Memory Restoration
Using Deep Brain Stimulation

Advisor: Dr. Carlos E. Davila

Doctor of Philosophy degree conferred May 14, 2022

Dissertation completed April 25, 2022

The past two decades have witnessed the rapid growth of therapeutic brain-computer interfaces (BCI) targeting a diversity of brain dysfunctions. Among many neurosurgical procedures, deep brain stimulation (DBS) with neuromodulation technique has emerged as a fruitful treatment for neurodegenerative disorders such as epilepsy, Parkinson’s disease, post-traumatic amnesia, and Alzheimer’s disease, as well as neuropsychiatric disorders such as depression, obsessive-compulsive disorder, and schizophrenia. In parallel to the open-loop neuromodulation strategies for neuromotor disorders, recent investigations have demonstrated the superior performance of closed-loop neuromodulation systems for memory-relevant disorders due to the more sophisticated underlying brain circuitry during cognitive processes. Our efforts are focused on discovering unique neurophysiological patterns associated with episodic memories then applying control theoretical principles to achieve closed-loop neuromodulation of such memory-relevant oscillatory activity, especially, theta and gamma oscillations.

First, we use a unique dataset with intracranial electrodes inserted simultaneously into the hippocampus and seven cortical regions across 40 human subjects to test for the presence of a pattern that the phase of hippocampal theta oscillation modulates gamma oscillations

in the cortex, termed cross-regional phase-amplitude coupling (xPAC), representing a key neurophysiological mechanism that promotes the temporal organization of interregional oscillatory activities, which has not previously been observed in human subjects. We then establish that the magnitude of xPAC predicts memory encoding success along with other properties of xPAC. We find that strong functional xPAC occurs principally between the hippocampus and other mesial temporal structures, namely entorhinal and parahippocampal cortices, and that xPAC is overall stronger for posterior hippocampal connections.

Next, we focus on hippocampal gamma power as a ‘biomarker’ and use a novel dataset in which open-loop DBS was applied to the posterior cingulate cortex (PCC) during the encoding of episodic memories. We evaluate the feasibility of modulating hippocampal power by a precise control of stimulation via a linear quadratic integral (LQI) controller based on autoregressive with exogenous input (ARX) modeling for in-vivo use. In the simulation framework, we demonstrate proposed BCI system achieves effective control of hippocampal gamma power in 15 out of 17 human subjects and we show our DBS pattern is physiologically safe with realistic time scales.

Last, we further develop the PCC-applied binary-noise (BN) DBS paradigm targeting the neuromodulation of both hippocampal theta and gamma oscillatory power in 12 human subjects. We utilize a novel nonlinear autoregressive with exogenous input neural network (NARXNN) as the plant paired with a proportional–integral–derivative (PID) controller (NARXNN-PID) for delivering a precise stimulation pattern to achieve desired oscillatory power level. Compared to a benchmark consisted of a linear state-space model (LSSM) with a PID controller, we not only demonstrate that the superior performance of our NARXNN plant model but also show the greater capacity of NARXNN-PID architecture in controlling both hippocampal theta and gamma power. We outline further experimentation to test our BCI system and compare our findings to emerging closed-loop neuromodulation strategies.

TABLE OF CONTENTS

LIST OF FIGURES	xii
LIST OF TABLES	xvi
CHAPTER	
1 INTRODUCTION	1
1.1. Distinctive Neural Oscillatory Activity During Episodic Memory	1
1.2. Closed-Loop Brain-Computer Interfaces in Treating Memory Conditions ...	6
1.3. Contribution and Objectives	9
2 BRAIN CONNECTIVITY AND FUNCTIONS DURING EPISODIC MEMORY	13
2.1. Introduction	13
2.2. Methods	15
2.2.1. Data Acquisition and Preprocessing	15
2.2.2. Phase Amplitude Coupling	17
2.2.3. Phase Synchrony and Oscillatory Power	19
2.2.4. Mixed Effects Models	20
2.3. Results	22
2.3.1. Significant xPAC Occurs in Memory Encoding	23
2.3.2. Detailed Examination of xPAC in the ERC and PHC.....	25
2.3.3. AH and PH Exhibit Different xPAC Properties	28
2.3.4. xPAC Is Not Confounded by Other Functional Measures	29
2.4. Discussion	32
2.5. Additional Analysis of Brain Functions	37
3 DEVELOPMENT OF BINARY-NOISE DEEP BRAIN STIMULATION.....	41

3.1.	Introduction	41
3.2.	Participants and Implantation	43
3.3.	Free-Recall Stimulation	44
3.4.	Binary-Noise Stimulation	47
3.5.	Unique Solution of the Stimulation System	51
4	A BRAIN-COMPUTER INTERFACE FOR MODULATING HIPPOCAMPAL GAMMA OSCILLATIONS VIA FREE-RECALL STIMULATION	58
4.1.	Introduction	58
4.2.	Materials and Methods	60
4.2.1.	Participants and Experimental Stimulation	60
4.2.2.	Data Acquisition and Processing	62
4.2.3.	Linear ARX Model	63
4.2.4.	LQI Servo-Controller	67
4.3.	Results	71
4.3.1.	Stimulation Effects on Hippocampal Gamma Power	71
4.3.2.	Model Validation and Performance	74
4.3.3.	Simulated Closed-Loop Control	80
4.4.	Discussion	81
4.5.	Conclusion	85
5	CLOSED-LOOP BRAIN-COMPUTER INTERFACES FOR MODULATING HIPPOCAMPAL OSCILLATORY ACTIVITY VIA BINARY-NOISE STIMU- LATION	87
5.1.	Introduction	87
5.2.	Materials and Methods	90
5.2.1.	Participants	90
5.2.2.	Binary-Noise Stimulation Paradigm and Data Acquisition	90

5.2.3.	Data Processing	92
5.2.3.1.	iEEG Denoising	92
5.2.3.2.	Hippocampal Oscillatory Power	93
5.2.4.	Linear State-Space Modeling	94
5.2.5.	Nonlinear Autoregressive-Exogenous Neural Network	95
5.2.6.	Proportional–Integral–Derivative Controller	101
5.3.	Results	105
5.3.1.	Stimulating the PCC Elicits Hippocampal Oscillatory Activity	105
5.3.2.	NARXNN Plant Outperformed LSSM Plant	109
5.3.3.	NARXNN-PID Architecture Is Superior In Modulating Oscillatory Power	114
5.4.	Discussion	118
5.5.	Conclusion and Significance	125
APPENDIX		
A	BN Stimulation Troubleshooting Procedure	126
	Bibliography	128

LIST OF FIGURES

Figure		Page
2.1	A. iEEG electrode maps: numbers of electrodes in each region from 40 subjects, with a minimum of 60 electrodes and a maximum of 201 electrodes contributing to 3767 hippocampal-cortical electrode pairs overall. B. Example trace of coronal plane T2 MR slices immediately to the front and back of the gyrus intralimbicus for ERC (upper, in red) and PHC (lower, in blue), respectively.	16
2.2	Example trace of an xPAC computing procedure. A. Instantaneous phase and amplitude from hippocampal and parahippocampal cortex (PHC) recordings. B. Analytical signals: complex-valued analytic signal in complex plane where red dot is the mean. Raw coupling magnitude M_{raw} is 9.8638 and preferred phase ϕ_{pf} is 268° . The green dot denotes the MI by z-scoring 250 surrogate (shuffled) samples with a magnitude M_{norm} of 0.8217.....	18
2.3	Schematic illustrations for the control analysis of xPAC, phase synchrony (PLV), cortical local PAC, and oscillatory power (gamma for cortices and theta for hippocampus). Functional effect (SuE versus UnsuE) of each connectivity/functional measure was computed by an independent mixed effects model.	20
2.4	Significant functional (SuE versus UnsuE) xPAC connections, identified by mixed effects models. For all significant connections, xPAC also had significantly greater magnitude than expected by chance (MI $Z > 1.96$). Left and right hemispheric connections are shown on each side of circle connectivity plots.....	24
2.5	MI functional effect for the ERC/PHC versus other regions. The observed MI functional effect (red line) was obtained by comparing the distributions of MI differences (MI during SuE - MI during UnsuE) for ERC/PHC and other five regions, and the null distribution H_0 was obtained by 1000 random shuffles.	25
2.6	Functional effects of xPAC in the theta-gamma spectrum, shown as the t-statistic at each frequency-frequency pixel from a mixed effects model. Red indicates greater magnitude during SuE, and blue indicates greater magnitude during UnsuE. Areas outlined in white indicate the significant xPAC patterns after FDR correction across theta/gamma spectrum ($Q = 0.05$) ...	26

2.7	Functional effects of xPAC at each theta frequency determined by mixed effects modeling. Results reflect aggregate values across regions of interest. Functional effects are represented by T statistics extracted from the MEM, where positive values indicate greater xPAC magnitudes during SuE than UnsuE, and vice versa.	27
2.8	Distribution of preferred phases of xPAC during successful encoding. Preferred phases were averaged (angular mean) across trials for each significant electrode pair. Color-mapping denotes the hippocampal theta frequencies, and ** indicates $p < 0.01$ via Watson-Williams test.....	27
2.9	Mean t-stats describing the functional xPAC effects for slow and fast theta bands in anterior versus posterior hippocampus in two hemispheres via ANOVA. * and ** denote $p < 0.05$ and $p < 0.01$, respectively.	29
2.10	A. Predicting models of xPAC magnitude during successful encoding using magnitudes of PLV, local PAC, and combined effects of PLV and PAC (PAC:PLV). The variance of xPAC magnitude explained by these predictors were all less than 5% (red line). B. Predicting models of xPAC functional effects. Baseline denotes the combined effects all predictors. The variance of xPAC functional effects explained by these predictors were all less than 1% (red line).	30
3.1	Example trace reconstructed locations of electrodes.	45
3.2	Example list of free-recall paradigm.....	46
3.3	Free-recall stimulation paradigm.....	47
3.4	Binary noise stimulation paradigm.	49
3.5	Illustration of proper configurations for bipolar and monopolar DBS.	50
3.6	BN stimulation procedure for the stimulation and EEG acquisition.	51
3.7	BN stimulation and EEG acquisition configuration.	53
3.8	Monitoring BN stimulation and EEG recordings.....	57
4.1	Simulation framework for control of RMS gamma power.	68
4.2	Linear quadratic integral servo-controller.....	69
4.3	Instantaneous RMS gamma power trials, $x_1(t), \dots, x_{10}(t)$ and their ensemble average $\bar{x}(t)$. The stimulation signal amplitude $u_s(t)$ is a 2 mA step function.	72

4.4	Impact of stimulation on mean gamma power.	73
4.4a	Percentage of trials with statistically significant increase in mean gamma power during stimulation.	73
4.4b	Increase in mean RMS gamma power $\Delta_\gamma\%$ during stimulation, derived from ensemble average.	73
4.5	Model quality metrics for identifying the ARX parameters for two different signals: an ARX process of order 6, $x_{ARX}(t)$, and a moving average (MA) process of order 29, $x_{MA}(t)$ having similar spectral features.....	76
4.5a	Mean squared prediction error.....	76
4.5b	Fit Percentage.	76
4.6	Model quality metrics for all subjects.	78
4.6a	Mean squared prediction error.....	78
4.6b	Fit percentage.....	78
4.7	Mean RMS gamma power level predictions by ARX model.	79
4.8	Comparison of averaged periodogram of instantaneous RMS gamma power (experimental) with theoretical power spectral density of identified ARX models, as given by (4.6) with $p = 6$	79
4.9	LQI controller simulations with control signal starting at $t = 0$ s for several subjects, showing mean and standard deviations over 100 independent trials.	81
4.10	Percent increase in RMS gamma power ($\Delta_\gamma\%$, see (4.3.1)) for open-loop (based on iEEG data) and closed loop conditions. The closed-loop results are based on simulated LQI control and had a mean of 22.8% across all subjects compared to 11.8% for the open loop condition.	81
4.11	Simulated closed-loop RMS gamma power versus desired RMS gamma power setpoint.....	82
4.12	Percent RMS gamma power increases for open-loop vs closed-loop stimulation. The dashed line has a slope of one.	84
5.1	Brain-computer interface framework for control of hippocampal RMS gamma/-theta power with Blackrock Cerestim stimulator and NSP module in the loop.	92

5.2	The architecture of NARXNN with one hidden layer and one output layer. d_x is the order delayed inputs and d_u is the order of delayed outputs. f_h is the sigmoid activation function and f_0 is a linear function.....	98
5.3	Illustration of batching I/O data into TA segments, where each batch is 40 ms long (20 samples), $u_i(1), u_i(2), \dots, u_i(n)$ and $y_i(1), y_i(2), \dots, y_i(n), i = 1, 2, 3, \dots, m$ are the input and output to the NARXNN model, respectively..	99
5.4	PID control structure with NARXNN and LSSM plants. TDL: tapered delay line.....	103
5.5	RMS gamma power trials in a time window of -400 ms to 1600 ms , where stimuli were applied at 0 ms	108
5.6	RMS theta power in a time window of -400 ms to 1600 ms , where stimuli were applied at 0 ms	108
5.7	Subsequent simulation effects (SSE) across subjects in four time windows for the theta and gamma bands.	109
5.8	Example trace of one-step-ahead predicted instantaneous theta and gamma RMS power via LSSM and NARXNN. $Error = y(t) - \hat{y}(t)$	110
5.9	Averaged Normalized mean squared error in one-step-ahead prediction of RMS gamma (left) and theta (right) power via NARXNN and LSSM.	111
5.10	Example trace of full input-driven predicted instantaneous theta and gamma RMS power via LSSM and NARXNN. $Error = y(t) - \hat{y}(t)$	112
5.11	Averaged Normalized mean squared error in full input-driven prediction of RMS gamma (left) and theta (right) power via NARXNN and LSSM. *, $p < 0.05$; **, $p < 0.01$; and *** $p < 0.001$	113
5.12	Example power trials from closed-loop control versus open-loop control using NARXNN-PID architecture.	115
5.13	Power increases in simulated closed-loop control of hippocampal theta and gamma power using NARXNN-PID versus LSSM-PID. Power increase = $(\bar{P}_{CL} - \bar{P}_{Exp})/\bar{P}_{Exp} \times 100\%$	117

LIST OF TABLES

Table	Page
4.1	Demographic information of participants in Free-recall stimulation paradigm. MTL: Medial temporal lobe, NTL: Neocortical temporal lobe, LH/RH: left/right hemisphere, B: bilateral. 61
5.1	Demographic information of participants in BN stimulation paradigm. MTL: Medial temporal lobe, NTL: Neocortical temporal lobe, LH/RH: left/right hemisphere, B: bilateral. 91
5.2	Ziegler-Nichols' PID tuning rules for K_p , K_i and K_d using the ultimate gain K_u and its oscillation period T_u 104
5.3	Averaged mean RMS gamma power across 2 s time window and across trials during stimulation (S) and no stimulation (NS). $\Delta Power$ denotes the mean RMS power difference, and T-stats is by one-tailed t-test. LB/RB and LC/RC are left/right anterior and posterior hippocampus, respectively. ... 106
5.4	Averaged mean RMS gamma power across 2 s time window and across trials during stimulation (S) and no stimulation (NS). 106

CHAPTER 1

INTRODUCTION

1.1. Distinctive Neural Oscillatory Activity During Episodic Memory

Episodic memory is triggered by contextual events. It recollects contextual information such as time, location, and emotion, associated with the specific event that has occurred. In 1972, Tulving described several properties and defined the term “episodic memory”, which has then been refined and elaborated by neuroscientists (Tulving, [1972](#)). Episodic memory is considered one of the major memory types due to its proven critical role in human cognitive processes. Other than the psychological features of episodic memory such as subjective sense of time, connection to the self, and autonoetic consciousness (Tulving, [2002](#); Gillund, [2012](#)), neuroscientists are also interested in brain functions that occur during such a process as well as mechanism linking memory to spatio-temporal contexts (Tulving, [1972](#); Tulving, [1983](#); Hasselmo, [2011](#); Burgess et al., [2002](#)). In clinical assessments, episodic memory tests involving behavioral tasks are often performed, as impairment of episodic memory in retrieving spatio-temporal context might indicate a symptom of neurodegenerative disorders such as Alzheimer’s disease and dementia (Hornberger and Piguet, [2012](#); Bäckman et al., [2001](#)). Importantly, such behavioral memory tests have also been used to analyze memory functions for the effects of other factors including memory encoding and pharmacological enhancement. Efforts to provide a quantification of memory function include the Wechsler Memory Scale developed in 1945, nearly 30 years prior to the Tulving’s study of episodic memory (Wechsler, [1945](#)). Currently, behavioral tasks with more details and specifications have been developed for human subjects. For instance, associated recognition (AR) tasks enable the subject to establish patterns of recognition novelty during retrieval by providing a series of

word pairs consisting of one novel word and one presented during encoding. Based on this paradigm, many have developed hippocampal models during memory retrieval (Norman and O'Reilly, 2003; Yonelinas et al., 2005; Eichenbaum, Yonelinas, et al., 2007). Another example is free-recall tasks, a paradigm commonly used among a wide variety of institutions and laboratories, with accessibility to a large amount of task lists, consisting of common noun words in various languages. During free-recall tasks, a subject is expected to remember and subsequently recall the words while brain electrophysiological signals and/or functional imaging data are collected for detailed quantitative assessment of memory functions. This type of data enables not only analyses on functional differences of memory conditions but also analyses on cognitive deficits using the serial position curve during memory retrieval (Baddeley and Warrington, 1970; Shallice and Warrington, 1970; Glanzer and Cunitz, 1966).

Neurological activity during behavioral tasks are recorded simultaneously via invasive or non-invasive approaches using neuroimaging such as positron-emission tomography (PET) and functional magnetic resonance imaging (fMRI), and electrophysiological recordings such as intracranial electroencephalogram (iEEG) and Electrocorticography (ECoG). With the emergence of these technologies, studies on memory mechanisms in humans and animals have established the importance of the hippocampus along with anatomically related regions in the medial temporal lobe (MTL) since the original reported impairment of episodic memory due to hippocampus damage (Scoville and Milner, 1957). Also, it has been demonstrated that prefrontal and parietal lobes serve as important supportive regions in the formation of new memories (Nolde et al., 1998; Fletcher et al., 1998; Wagner et al., 2005; M. A. Wheeler et al., 1995; Cabeza et al., 2008; M. A. Wheeler et al., 1997). Therefore, the formation of new memories requires the coordination of neural activity across widespread brain regions (K. Friston et al., 1997). For this reason, several functional and connectivity measures were developed for analyzing neural oscillations using iEEG. Oscillations in various frequency bands, namely, delta (4 Hz and below), theta (4-8 Hz), alpha (8-12 Hz), beta (12-30 Hz) and gamma (30-150 Hz), have been demonstrated to reflect significant functionalities in neu-

rocognitive processes. Theta and gamma waves are considered the most critical oscillations during memory processes. For example, theta band (4-8 Hz) oscillations are implicated in memory functions and cognitive control, and theta power is found to reveal functional differences during both encoding and retrieval of the episodic memory (Lin, Rugg, et al., 2017; J. F. Burke et al., 2014; Staudigl and Hanslmayr, 2013; B. C. Lega, Jacobs, et al., 2012; Nyhus and Curran, 2010; Sederberg, M. J. Kahana, et al., 2003a; Buzsáki, 2002). On the other hand, gamma band (30-150 Hz) oscillations are thought to be implicated in many perceptual processes, and the memory functionalities of gamma power are also observed in multiple brain regions (Lin, Umbach, et al., 2019; Vugt et al., 2010; Sederberg, Gauthier, et al., 2006; Sederberg, M. J. Kahana, et al., 2003a).

To incorporate neural oscillations in different frequency bands, several quantitative examinations of inner-regional functions and cross-regional connectivity have been developed. For example, phase synchrony describes a precise phase-locking phenomenon between two neuronal groups within a short period of time. Bullock and McClune used spectral coherence as a measure of phase synchrony and found 1-50 Hz oscillations are coherent across brain surfaces in rodents (Bullock and McClune, 1989). Bressler et al. reported increased broad-band coherence across multiple neocortices in 30-80 Hz gamma range (Bressler et al., 1993). Lachaux et al. described a measure of phase synchrony by separating amplitude and phase component, which can then be directly interpreted in the framework of neural integration, namely, phase locking value (PLV), by which he reported large-scale inter-regional synchronies in the gamma band between hippocampus and prefrontal gyrus as well as local synchronies within a limbic region (Lachaux et al., 1999). The modulation of high-frequency oscillatory activity according to the phase of a low-frequency oscillation is known as phase amplitude coupling (PAC). This pattern of brain oscillations has been established in both rodents and humans and is thought to be critical for properties of episodic memory such as temporal ordering (Squire, 1992), ensemble organization in working memory, and the phenomenon of phase coding (Buschman et al., 2012; Jensen and Lisman, 2000). In humans,

PAC within brain regions has been demonstrated in the hippocampus and neocortex, and the magnitude of coupling appears to predict memory encoding success (Canolty, Edwards, et al., 2006; B. Lega, J. Burke, et al., 2014).

A Review: High Gamma Power Is Phase-Locked to Theta Oscillations in Human Neocortex.

Canolty, Edwards, et al. observed a robust neuro-coordination that the phase of 4-8 Hz theta modulates the power in the 80-150 Hz high gamma (HG) in humans during behavioral tasks using ECoG signals (Canolty, Edwards, et al., 2006). Such coordination of oscillatory activity in two frequency bands within the cortex using both phase and amplitude information was termed phase-amplitude coupling (PAC). It is one of the approaches to analyze local neural activity, along with other cross-frequency coupling (CFC) measures. The study pointed out that distinctive PAC patterns exhibited in two specifically oscillatory frequencies, theta and high gamma, which have been extensively demonstrated in human cognition processes. There had been evidence that theta and gamma oscillations individually affect cognition and that CFC occurred in cortices prior to the study. For instance, theta is thought to manipulate the firing rate of a single neuron and to affect gamma power, where low and high gamma bands exhibited distinctive functional differences in various brain regions (Lin, Rugg, et al., 2017; Lin, Umbach, et al., 2019; B. C. Lega, Jacobs, et al., 2012; J. F. Burke et al., 2014; Sederberg, M. J. Kahana, et al., 2003a; Sederberg, Gauthier, et al., 2006; Buzsáki, 2002; Nyhus and Curran, 2010). However, there was no direct examination of theta to high gamma linkage from either scalp or cortical recordings. Canolty, Edwards, et al. reported a promising result that significant theta-HG PAC occurred (83.4% of the tested electrodes, each of which $p < 0.001$, FDR corrected) during various behavioral tasks (details are found in Canolty’s supplementary materials). Further, the statistical procedures showed that PAC exhibited positive correlation among similar behavioral tasks whereas negative or null correlations occurred across different tasks, contributing to the conclusion: “PAC modulates

network engagement, enabling a flexible control of cognitive processing". Summarizing these results:

1. HG power is modulated by theta phase during cognitive process, and such theta-HG PAC exhibited significant effects across a wide variety of brain cortices;
2. An increase in theta power strengthens theta-HG PAC, as the result of interacting neuronal populations;
3. The theta-HG PAC is task dependent, supporting the hypothesis that PAC between distinct brain rhythms (such as theta and gamma) facilitates the coordination of neuronal populations required for adaptive behavior in humans;

Canolty, Edwards, et al. promoted an oscillatory hierarchy process across spatial and temporal scales that may regulate the effective long-range communication, which requires precise matching of the relative phase of distinct rhythms to axonal conduction delay, between neuronal groups (Fries, [2005](#); Lakatos et al., [2005](#)). Importantly, to quantify such interactions between oscillatory activity, Canolty, Edwards, et al. described a metric with relevant statistical procedures that was inspired by a demonstrated methodology called PLV (Lachaux et al., [1999](#)). Although, this review is not intended to distinguish PAC from other CFC measures in a qualitative fashion, the proposed dissertation will compare typical CFC methodologies and multiple PAC metrics more comprehensively including numerical results of PAC from mostly commonly used metrics (Canolty's computation of PAC is illustrated in [Figure 2.2](#)).

1.2. Closed-Loop Brain-Computer Interfaces in Treating Memory Conditions

These functional and connectivity measures are ‘biomarkers’ for memory because they are representations of memory functions and some of them have been integrated with brain computer interfaces (BCIs) for clinical assessments and medical treatment. Such development of BCIs has drawn extensive attentions and has been transforming into a multi-million commercial market for both clinical/medical and personal uses (Vidal and JJ, 1973; Vidal, 1977; Musk et al., 2019; Jantz et al., 2017). Clinically, BCIs are often directed at assisting, repairing and enhancing human cognitive, sensory and, motor functions and are aimed at precise treatment for neurological and neuropsychiatric disorders with implementation of deep brain stimulation (DBS, i.e. applying electrical stimuli directly to the intracranial brain site). Nascent therapies for memory restoration exist, based on neuromodulation targeting Parkinson’s disease (Deuschl, Schade-Brittinger, et al., 2006; De Hemptinne et al., 2015), epilepsy (B. C. Lega, Halpern, et al., 2010), and depression (Mayberg et al., 2005; C. Zhou et al., 2018). Most of the DBS paradigms are in the form of open-loop stimulation, which rely on manually setting stimulation parameters from subject to subject via a trial-and-error procedure, guided by clinical assessment of symptoms (Deuschl, Schade-Brittinger, et al., 2006). In contrast, closed-loop DBS paradigms use feedback from neural activity in real time to adapt the stimulation pattern (e.g., amplitude, frequency, duration, etc.) and it has shown fruitful results. For instance, two closed-loop DBS systems have been granted FDA approval recently: the NeuroPace responsive neuromodulation system (RNS) for epilepsy treatment and the Percutaneous PC deep brain stimulation system for Parkinson’s Disease treatment (Nune et al., 2019; Tinkhauser et al., 2017). In the proposed dissertation, a BCI system for closed-loop DBS is studied in the context of episodic memory restoration. Preliminary experiments have shown promising outcomes in improving memory performance by accurate control of hippocampal gamma power, as the biomarker of episodic memories.

Ezzyat et al. described a classifier-based closed-loop DBS system to selectively assist poor memory performance during memory encoding (Ezzyat et al., 2018). Rather than modeling the dynamics of neural activity, the system sought to model functional networks during memory encoding using spectral features of the recordings. This system converted a complex neuromodulation problem into a simpler one: when to apply stimulation to the target regions (lateral temporal cortex versus a control target). Predictions of encoding success were based on a logistic classifier using spectral features of a wide range of 1-200 Hz oscillatory power via Morlet wavelet decomposition, specifically tuned for each subject. Recorded-only data (a subset of the free-recall lists) were used for training the classifier and the remaining lists were split into two groups: 1) a control group where no stimulation was applied to subjects during the task and 2) the experimental group based on the likelihood of successful encoding via the classifier, using estimated spectral power in the time-window of 0-1366 ms (relative to each encoding word) as features. If the classifier predicted the chance of successful encoding exceeded a threshold (probability of 0.5), the system triggered bipolar stimulation for 500 *ms*.

The stimulation sequences, on the other hand, were guided by safety considerations as well as clinical need. Although, biphasic pulses with multiple frequencies and amplitudes were tested for each subject *beforehand* to determine the best combination of frequency and amplitude that maximized subsequent memory effect (SME, i.e., greater brain activation during encoding for later successfully retrieval compared to unsuccessful retrieval (Paller and Wagner, 2002)). The amplitude and the frequency of the stimulation pattern was fixed throughout the stimulation paradigm for each subject. By using generalized linear mixed effect model (GLME) and other statistical procedures, the study reported three key findings:

1. There was 15% increase in memory performance on average across 40 subjects.
2. The classifier had a mean area under the receiver-operating characteristic curve (AUC) of 0.61 for predicting memory encoding success across multiple contacts.

3. Stimulation of lateral temporal cortex significantly influenced ($p < 0.001$) neural activity compared to other stimulation sites such as hippocampus, MTL, LPF, and parietal cortex.

Nevertheless, such closed-loop systems brought several concerns regarding the robustness and practicality. First, the reported logistic classifier can be easily out-performed using modern machine learning techniques (Arora et al., 2018). Second, the classifier used extensive recordings from multiple contacts for each subject. Its low generalizability would make it impractical for clinical devices. Moreover, the system was not intended to precisely stimulate a brain site based on neural dynamical feedback. The absence of adaptive amplitude or frequency modulation of the stimulation sequence made it an on-demand open-loop stimulation system.

Alternatively, Yang, Connolly, et al. proposed a control-theoretic system to modulated the neural dynamics (Yang, Connolly, et al., 2018). The system focused on dynamic input-output (IO) models for neural activity that were ideal for closed-loop control via the proposed system identification framework, which utilized open-loop stimulation dataset. The fitted model, a linear state-space model (LSSM), was then used for linear controller design. The study also raised a critical concern regarding the system identification process, that an optimal input should have a wide spectrum (such as white noise), which is capable of capturing frequency response across all frequencies of the system for accurate modeling (Ljung, 1999). For this purpose, Yang, Connolly, et al. designed a unique stimulation pattern termed binary noise (BN)-modulated stimulation, consisting of biphasic pulses with random alternating amplitudes and frequencies, to maximally enrich frequency components in the spectrum. With the use of linear quadratic Gaussian (LQG) controller, which had a recursive Kalman filter to estimate the biomarker (mood for depression) and a linear quadratic regulator (LQR) controller to manipulate it, the study reported precise controls of the biomarker in both random simulations (Monte-Carlo) and the clinical testbed without actual participants (via

a ECoG simulator). Along with other reported details, this system suggested that a control-theoretical system may be ideal for DBS for memory improvement due to its capability of modeling and then manipulating a complex dynamical system. Furthermore, it demonstrated white-noise-like open-loop stimulation patterns are critical in the system identification. With the same testing configuration, the BN pattern out-performed other ordinary stimulation sequences that have been used in open-loop stimulation paradigms (Eykhoff et al., 1974; H. J. Tulleken, 1990; Møller, 1986; Ljung, 2007; H. Tulleken, 1988).

1.3. Contribution and Objectives

It is well-established that high-frequency oscillation is modulated by the phase of a low-frequency oscillation. This neural pattern, known as phase-amplitude coupling (PAC), has been considered as an important property of episodic memory from numerous investigations in rodents and humans (Squire, 1992; Buschman et al., 2012; Jensen and Lisman, 2000). Cortical and hippocampal local PAC has shown potential in predicting memory encoding success in humans (Canolty, Edwards, et al., 2006; B. Lega, J. Burke, et al., 2014), and inter-regional PAC has been studied in rodents for hippocampus and extra-hippocampal regions. This inter-regional relationship has demonstrated that the phase of the hippocampal theta oscillation modulates gamma oscillatory power in the striatum (Tort, R. W. Komorowski, et al., 2009; Onslow et al., 2011). In addition, theta-gamma relationships have been reported for entorhinal-hippocampal communication within the medial temporal lobe, where the precisely timed arrival of entorhinal information (measured by gamma band activity) relative to the hippocampal theta oscillation in CA1 is associated with behavioral changes (Buzsáki, 2002; Hasselmo, 2005). These findings highlight that cross-regional phase amplitude coupling (xPAC) may be a mechanism by which an integrated representation of a memory is formed through precise coordination between brain regions. However, this behavioral pattern that the phase of the hippocampal theta oscillation modulates gamma oscillations in the cortex

had not been observed in human subjects. With this goal in mind, we aim to establish xPAC in human with following aspects:

1. Prove the presence of significant xPAC in human subjects.
2. Establish that the magnitude of xPAC predicts memory encoding success.
3. Describe specific frequencies within the broad 2-9 Hz theta range that govern hippocampal-cortical xPAC.
4. Compare anterior versus posterior hippocampal xPAC functional patterns.

The open-loop stimulation paradigm for treating memory dysfunctions only relies on manual setting of stimulation parameters that guided by typical stimulation protocol and safety concerns. Technically, such open-loop stimulation is insufficient for capturing the fast dynamics of electrophysiological neural activity during cognition. Although open-loop stimulation has been proven effective for movement and sensory disorders, it has largely failed to demonstrate a benefit in memory performance and even led to negative effects on memory (Mankin and Fried, [2020](#)). Conversely, the closed-loop stimulation paradigm has shown greater promise in improving memory performance due to its responsiveness and adaptiveness in modeling the neural activity and subsequently manipulating stimulation pulses. Recent studies highlighted the potential of closed-loop DBS for memory restoration, where the BCIs employed a wide variety of strategies. Prior to the design of the system, two important questions must be considered:

1. What brain signal can be used as an effective 'biomarker' for memory?
2. What stimulation strategy can modulate this biomarker safely and effectively?

Hippocampal oscillatory power in the theta and gamma bands are rational candidates since it is well-established that changes of oscillatory power in these frequencies predict memory

success from numerous studies in both human and animals (Sederberg, M. J. Kahana, et al., 2003a; Fries, 2009; Steinvorth et al., 2010; Sederberg, Schulze-Bonhage, et al., 2007; Kota et al., 2020; Jacobs, B. Lega, et al., 2017; Jacobs, 2014; Lin, Rugg, et al., 2017). Additionally, theta and gamma oscillatory power are critical components of neural activity in inner-regional phase synchrony and CFC (Sederberg, Schulze-Bonhage, et al., 2007; Solomon et al., 2017). For the second question, stimulation of the PCC has been demonstrated to reliably increase hippocampal gamma power and itself has shown dense connectivity to widespread brain regions (Natu et al., 2019; Bai et al., 2009; Khalsa et al., 2014). For safety considerations, even with long duration (20 seconds or more) of stimulation of the PCC, no seizures or symptoms related stimulation was reported.

In summary, this dissertation seeks to (i) test and explain a novel brain connectivity termed “xPAC” that supports the encoding of episodic memory, (ii) test the feasibility of a closed-loop brain-computer system for modulating hippocampal gamma power using the existing open-loop EEG data during PCC-applied free-recall stimulation paradigm, (iii) adapt and develop a new PCC-applied open-loop stimulation called “BN stimulation” using devices manufactured by Blackrock, and (iv) develop an advanced nonlinear BCI system targeting neuromodulation of hippocampal theta and gamma oscillatory power. The composition of the dissertation is shown as follows:

1. Chapter 2 reports our investigation of a novel brain connectivity measure named “cross-regional phase-amplitude coupling (xPAC)”, which is proven to support encoding of episodic memory (published in a journal paper, Wang, Schmitt, et al., 2021).
2. Chapter 3 describes our development of PCC-applied stimulation paradigm termed “binary-noise stimulation”. Our unique considerations and technical solutions have been adapted by a variety of research groups.

3. Chapter 4 unveils a closed-loop BCI for modulating hippocampal gamma power using PCC-applied DBS, based on an LQR controller via linear ARX modeling (presented at the 50th SfN Conference, and submitted revision to a journal, to date).
4. Chapter 5 discusses a closed-loop BCI targeting neuromodulation of hippocampal theta and gamma power using PCC-applied DBS, based on an advanced dynamic nonlinear ARX neural network (NARXNN) and the more comprehensive BN stimulation paradigm (in preparation for submission).

CHAPTER 2

BRAIN CONNECTIVITY AND FUNCTIONS DURING EPISODIC MEMORY

2.1. Introduction

The organization of high-frequency oscillatory activity according to the phase of a low-frequency oscillation is known as phase amplitude coupling (PAC). This pattern of brain oscillations has been established in both rodents and humans and is thought to be critical for properties of episodic memory such as temporal ordering (Squire, 1992), ensemble organization in working memory, and the phenomenon of phase coding (Buschman et al., 2012; Jensen and Lisman, 2000). In humans, PAC within brain regions has been demonstrated in the hippocampus and neocortex, and the magnitude of coupling appears to predict memory encoding success (Canolty, Edwards, et al., 2006; B. Lega, J. Burke, et al., 2014). In rodents, PAC has been extended to include interregional relationships between the hippocampus and extra-hippocampal regions-specifically, coupling between the hippocampus and striatum/PFC-by which the phase of the hippocampal theta oscillation modulates gamma oscillatory activity in the striatum and vice versa (Tort, R. W. Komorowski, et al., 2009; Onslow et al., 2011). Reported findings suggest that interregional phase amplitude coupling (xPAC) may be a mechanism by which an integrated representation of a memory is formed through precise coordination of local high-frequency oscillations.

Precise theta-gamma relationships have also been reported for entorhinal-hippocampal communication. In rats, the precisely timed arrival of entorhinal information (measured by gamma band activity) relative to the hippocampal theta oscillation in CA1 is associated with

Copyright clearance: this work has been published in Wang, Schmitt, et al., 2021 in the Hippocampus Journal (<https://onlinelibrary.wiley.com/doi/abs/10.1002/hipo.23309>). Permission of reuse of the published content in this dissertation is granted by the publisher (copyright holder). License ID: 5291590284992.

behavioral changes (Buzsáki, 2002; Hasselmo, 2005). Another study showed that the precise timing of ERC input into CA3 helps distinguish encoding versus retrieval-related activity and suggests that this temporal relationship is necessary for reversal of learning (Hasselmo et al., 2002). These findings highlight a point of clarification: xPAC-type relationships do not, in and of themselves, imply causality or directional information flow. Rather, xPAC implies a relative coordination relationship between brain regions.

To determine whether xPAC supports human episodic memory, we quantified interregional phase amplitude coupling using theta oscillations recorded in the hippocampus and gamma oscillations recorded in the cortex during episodic memory encoding. We utilized a unique dataset of 40 human subjects with intracranial electrodes implanted in both the anterior and posterior hippocampus and in seven cortical regions in both hemispheres: entorhinal cortex (ERC), parahippocampal cortex (PHC), lateral prefrontal cortex (LPF), lateral middle temporal gyrus (LMT), posterior cingulate cortex (PC), basal temporal cortex (fusiform and inferior temporal gyrus, BTL), and lateral parietal cortex (LP). Anatomical details governing how electrodes were aggregated into regions is available in the Methods section. The demarcation between the ERC and PHC followed established methods, incorporating the coronal plane of the gyrus intralimbicus along the parahippocampal gyrus.

Using the modulation index method described by Canolty (Canolty, Edwards, et al., 2006), we identified hippocampal-cortical connections for which 1) significant xPAC is present (i.e. there is significantly non-uniform distribution of gamma power across hippocampal theta phase) and 2) xPAC predicts memory encoding success (functional xPAC). This method is relatively robust to signal noise over the time segments available in the free recall task (Onslow et al., 2011). The parahippocampal cortex and entorhinal cortex in particular consistently showed significant functional xPAC in multiple significance tests; therefore, we sought to characterize hippocampal-ERC/PHC xPAC in more detail. For these regions in both hemispheres, we examined the preferred theta frequencies for hippocampal coupling and

compared anterior versus posterior hippocampal coupling strength. We examined the preferred theta phase angle at which xPAC occurs and compared this to local PAC measured in these regions, revealing regional and hemispheric differences. Furthermore, when examining this new measure of functional connectivity, we wanted to ensure that our measurement of xPAC was not confounded by other oscillatory patterns that characterize successful memory encoding, especially changes in cortical gamma power and interregional phase synchrony. We therefore integrated these measurements, along with local PAC, into a multivariate model to understand the relative impact of power modulation, xPAC, and phase synchrony on the prediction of encoding success. We place our findings in the context of existing theories of PAC regarding the organization of oscillatory activity during the representation of episodic memories.

2.2. Methods

2.2.1. Data Acquisition and Preprocessing

The intracranial electroencephalogram (iEEG) data were collected at UT Southwestern medical center while subjects performed the free recall task after seizure mapping surgery (stereo EEG electrode implantation). The free recall task we used consisted of 25 lists, each comprised of 12 common nouns. Each word was presented on the monitor for 1800 ms followed by 400 ms of blank screen. A 30 second interval in between every two lists was given for the subject to recall as many of the words as possible in any order. An example list of free-recall tasks is shown in Figure 3.2. In the study, seven regions of interests (ROIs) comprised of entorhinal cortex (ERC), parahippocampal cortex (PHC), lateral prefrontal (LPF), lateral middle temporal (LMT), posterior cingulate (PC), basal temporal lateral (BTL), and lateral parietal cortex (LP) were selected to construct xPAC connectivity for both anterior hippocampus (AH) and posterior hippocampus (PH) in both left and right hemispheres. Electrode localization was achieved by co-registration of the post-

operative computer tomography scans with pre-operative magnetic resonance images, which were evaluated by a member of the neuroradiology team to determine the final electrode locations. We utilized an iEEG database including 40 subjects, which contributed to 3767 hippocampus-to-ROI electrode pairs. All electrode pairs reflect signal recorded from the same subject. The iEEG recordings were down-sampled to 250 Hz, notch filtered at 60 Hz, time-aligned into individual trials (stimulus onset at 0 ms, 1800 ms per trial), and labeled as successful encoding (SuE, recalled items) or unsuccessful encoding (UnsuE, unrecalled items) based upon behavioral performance. Demarcation between the ERC and PHC in the parahippocampal gyrus was the gyrus intralimbicus, following established methods. Along with the iEEG electrode maps, this demarcation is shown in Figure 2.1, showing coronal plane T2 slices immediately to the front and back of the gyrus intralimbicus for ERC and PHC, respectively (Insausti et al., 2019; Maass et al., 2015).

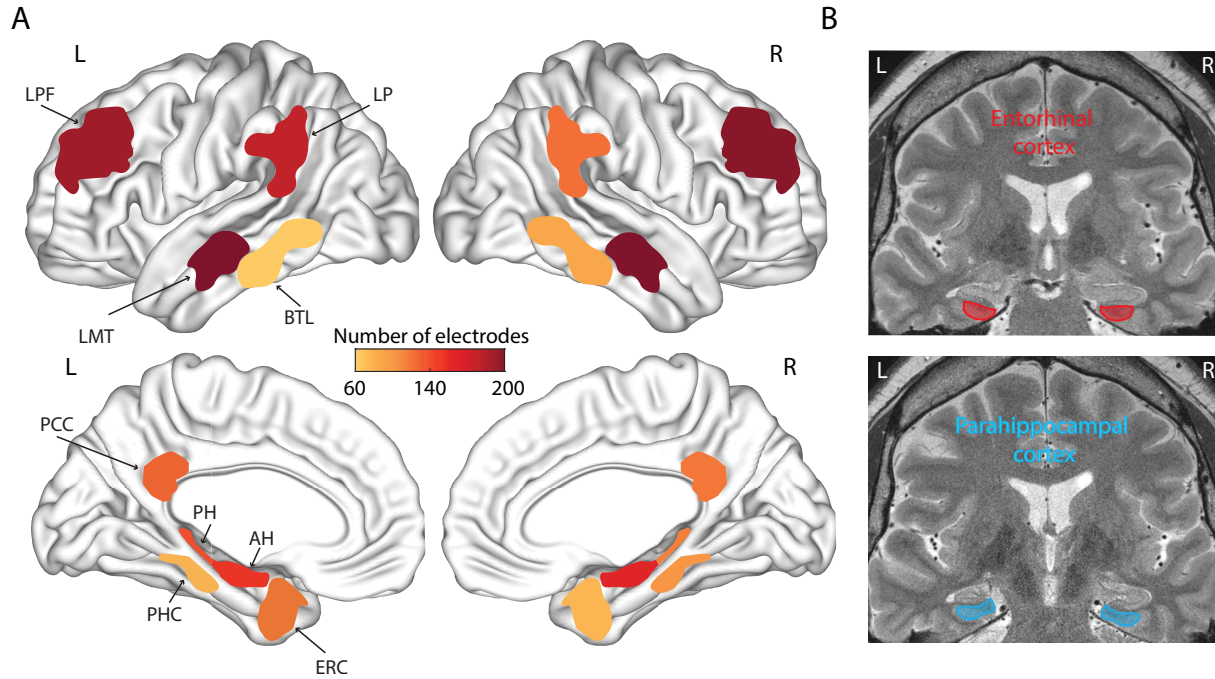


Figure 2.1: A. iEEG electrode maps: numbers of electrodes in each region from 40 subjects, with a minimum of 60 electrodes and a maximum of 201 electrodes contributing to 3767 hippocampal-cortical electrode pairs overall. B. Example trace of coronal plane T2 MR slices immediately to the front and back of the gyrus intralimbicus for ERC (upper, in red) and PHC (lower, in blue), respectively.

2.2.2. Phase Amplitude Coupling

The modulation index (MI) is a cross-frequency coupling measure of nested oscillations applied principally to theta and gamma bands (Canolty, Edwards, et al., 2006). xPAC expands the application of this measure by utilizing hippocampal theta phase with cortical gamma amplitude. The instantaneous theta phase of hippocampus and gamma amplitude (envelope) of the ROI can be obtained by $a_{ROI\gamma}[n] = |\mathcal{H}(x_{ROI}[n])|$, and $\phi_{H\theta}[n] = \arg(\mathcal{H}(x_H[n]))$ where \mathcal{H} denotes the Hilbert transform, and $x_{ROI\gamma}[n]$ and $x_{H\theta}[n]$ denotes the bandpass filtered signals of hippocampus in theta band and ROI in gamma band, respectively. The analytical signal of the two is obtained by:

$$z[n] = a_{ROI\gamma}[n] \exp(i\phi_{H\theta}[n]) \quad (2.1)$$

The magnitude of the mean vector, M_{raw} , denotes the coupling strength, whereas the phase angle of the mean, ϕ_{pf} , represents the preferred phase for coupling. They are given by:

$$M_{raw} = \left| \frac{1}{N} \sum_{n=1}^N z[n] \right| \quad \phi_{pf} = \arg\left(\frac{1}{N} \sum_{n=1}^N z[n] \right) \quad (2.2)$$

Shuffled data is then created by inserting a randomly generated time lag between the instantaneous theta phase and instantaneous gamma amplitude when forming the analytical signal. With iterations of this randomization procedure, a normalized magnitude is calculated:

$$M_{norm} = \frac{M_{raw} - \mu}{\sigma} \quad (2.3)$$

where μ and σ are the mean and the standard deviations of surrogate magnitudes, respectively. In this study, 250 surrogates are implemented for each trial (as presented in Figure

2.2B). The surrogate procedure normalizes the MI among different subjects and regions which most likely have various power levels. An MI has a magnitude of M_{norm} at the angle of preferred phase, denoting the asymmetry of the analytical signal in the complex plane. If an analytical signal is circularly symmetric, it indicates that no coupling is found, while significant coupling occurs at the phase at which the magnitude is larger. An example computing procedure of xPAC between AH and PHC is shown in Figure 2.2, where the unfiltered trace from the PHC is shown in row **A1**, bandpass filtered low gamma (30-70 Hz) oscillation from PHC and its corresponding amplitude are shown in row **A2**, bandpass filtered slow theta oscillation from AH and its corresponding phase are shown in row **A3**, and the real and imaginary components of the signal were used in the MI calculation are shown in row **A4**.

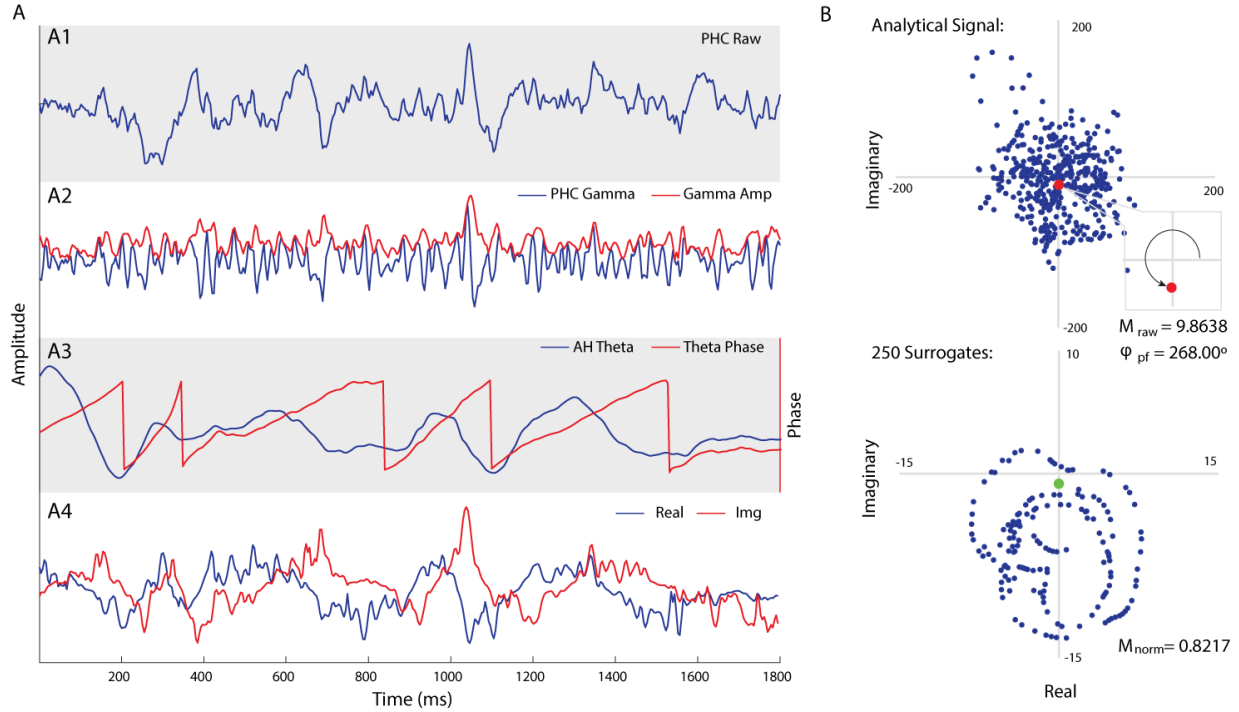


Figure 2.2: Example trace of an xPAC computing procedure. **A.** Instantaneous phase and amplitude from hippocampal and parahippocampal cortex (PHC) recordings. **B.** Analytical signals: complex-valued analytic signal in complex plane where red dot is the mean. Raw coupling magnitude M_{raw} is 9.8638 and preferred phase ϕ_{pf} is 268° . The green dot denotes the MI by z-scoring 250 surrogate (shuffled) samples with a magnitude M_{norm} of 0.8217.

To develop a model that test for functionally significant xPAC while accounting for possible functional effects of phase synchrony and differences in oscillatory power, hippocampal-cortical phase synchrony in theta band, cortical functional gamma oscillatory power, hippocampal functional theta oscillatory power, along with cortical local PAC were computed as part of the control analysis. The computation of local PAC remained the same but both instantaneous theta phase and gamma amplitude were from the same target region. The computations of phase synchrony and oscillatory power are described in following sections.

2.2.3. Phase Synchrony and Oscillatory Power

We sought to develop a model that tested for functionally significant xPAC while accounting for possible functional effects of phase synchrony and differences in gamma oscillatory power (the analysis described in Figure 2.3). For each hippocampal-cortical connection, we computed phase locking value (PLV, Lachaux et al., 1999; Siapas et al., 2005). Instantaneous phases for hippocampus and target cortex are obtained by the Hilbert transform of the bandpass filtered local signals. The PLV is given by:

$$PLV = \left| \frac{1}{N} \sum_{n=1}^N e^{i(\phi_{H\theta}[n] - \phi_{ROI\theta}[n])} \right| \quad (2.4)$$

We measured functional effects related to differences in oscillatory power by incorporating the normalized power for the frequency range of interest relative to the entire spectral power via the power spectral density estimation (PSD), such that:

$$Power_{\gamma} = \frac{\sum_{\gamma} \hat{P}_{xx}(\gamma)}{\sum_f \hat{P}_{xx}(f)} \quad (2.5)$$

where \hat{P}_{xx} is the PSD estimation via periodogram over the entire spectrum, γ denotes the gamma band in interests, and f is the entire bandwidth such that $0 \leq f \leq \frac{f_s}{2}$, where f_s denotes the sampling frequency of iEEG signals. These estimations were performed sepa-

rately for successful and unsuccessful encoding events and incorporated into our mixed effects models described below.

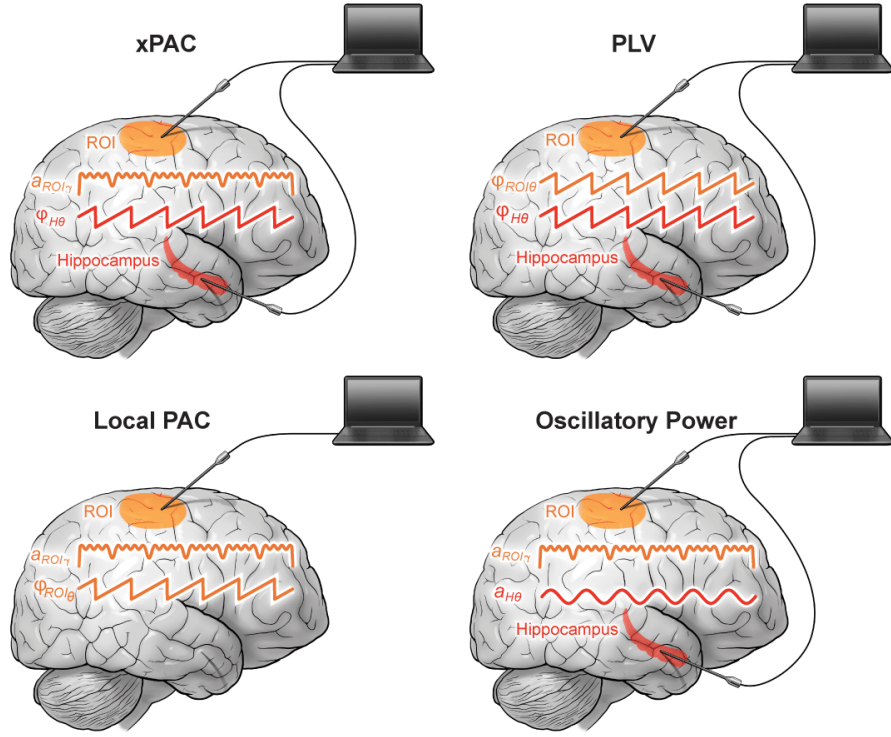


Figure 2.3: Schematic illustrations for the control analysis of xPAC, phase synchrony (PLV), cortical local PAC, and oscillatory power (gamma for cortices and theta for hippocampus). Functional effect (SuE versus UnsuE) of each connectivity/functional measure was computed by an independent mixed effects model.

2.2.4. Mixed Effects Models

We used mixed effects modeling (MEM) to assess for functional significance of observed SuE/UnsuE differences in observed xPAC (as extracted by MI). Measured MI values were separately entered for the SuE and UnsuE conditions for each observed electrode pair (which for xPAC included theta phase information measured in the hippocampus and gamma amplitude information measured in the cortical region of interest). Subject was included as a

random effect in the model. Such a model can be written as:

$$y = X\beta + Zu + \epsilon \quad (2.6)$$

where y is the responding variable (e.g. encoding successes for functional effects and xPAC for predicting), β is a coefficient vector of fixed effects, u is a vector of random effects, ϵ is a vector of random errors, X is the regressor matrix (a.k.a. design matrix) associated with the independent variables, and Z is the regressor matrix associated with subject labels. We followed best linear unbiased estimates (BLUE) and predictors (BLUP) to solve the mixed effects equations (MME, as in C. R. Henderson, 1973; Pinheiro and Bates, 1996).

In our analysis of xPAC at each frequency-frequency pixel as in Figure 2.6, hippocampal-ERC/PHC xPAC was computed using continuous frequency values, by which theta oscillations were split into bins with 1 Hz resolution and gamma activity was divided into bins with 2Hz resolutions. Functional effects were modeled (using the same MEM approach) at each frequency-frequency pixel, and the t-stats of the fixed effects were represented as functional patterns of the xPAC.

For the analysis presented in Figure 2.3 (testing for the impact of inter-regional synchrony, locally measured phase amplitude coupling, and gamma power differences on xPAC), we employed two methods, one of which used the functional xPAC effects (Sue/UnsuE differences) and the other that used the measured values (such as MI) themselves. First we modeled xPAC using magnitudes observed for these values across recording locations using the same mixed effects approach. The explained variance using these magnitudes is plotted in Figure 2.10A. Then, we modeled the *functional* effects of xPAC differences using the functional effects for these other predictors (i.e., local PAC, inter-regional PLV, and cortical gamma and hippocampal theta oscillatory power) using the mixed effects approach. We show the explained variance for each predictor in Figure 2.10B. The purpose of this analysis was to

test whether and how these other factors explained the magnitude and functional effects of xPAC using explained variance.

We used an n-way ANOVA to test for differences in the magnitude of xPAC (across all cortical locations) when the theta signal was recorded from the anterior versus posterior hippocampus. The purpose of this analysis was to test whether anterior or posterior xPAC exhibits a larger functional effect across all connections. This was done separately for the left and right hemisphere. The predicting models were built region by region with xPAC information in all four theta/gamma combinations (as presented in Figure 2.9). We used the T-statistics describing the functional xPAC effect (SuE vs UnsuE) from the MEM and aggregated these across electrode pairs. We tested for a primary effect of frequency band and hippocampal location.

In a separate convergent analysis approach meant to demonstrate the robustness of our principal findings, functional effects were also examined by comparing the distribution of t-statistics between SuE and UnsuE incorporating 1000 permutations, followed by false discovery rate (FDR) correction ($q=0.05$) across connections. The individual t-stats from the hypothesis testing are included in Supplemental Materials¹. This method did not utilize the MEM to assess significance - but rather a t-test applied to the distribution of MI values for the SuE and UnsuE conditions across electrodes comprising the data for each region of interest.

2.3. Results

Our analysis aimed to understand how the organization of gamma band activity in the cortex relative to hippocampal theta oscillations (as quantified by phase amplitude coupling) can predict memory encoding success, hypothesizing that this hippocampal-cortical relationship represents another form of interregional coordination along with phase-phase

¹Supplemental Materials are published with the original paper (Wang, Schmitt, et al., 2021), available at <https://onlinelibrary.wiley.com/doi/abs/10.1002/hipo.23309>

and amplitude-amplitude coupling that has been described in human systems (Lachaux et al., 1999; Aru et al., 2015). We calculated inter-regional phase-amplitude coupling (xPAC) using intracranial data across 40 patients who performed the free recall episodic memory task. Subjects recalled $23.62\% \pm 12.12\%$ of items with a rate of list intrusions of 4.82%. The phase of theta frequency oscillation was recorded in the hippocampus while the amplitude of gamma oscillation was obtained from one of seven cortical regions (ERC, PHC, LPF, LMT, PC, BTL, and LP) in each hemisphere. We quantified the magnitude of xPAC present in these signals with the modulation index developed by Canolty, Edwards, et al. Example data showing the implementation of this method are shown in Figure 2.2. We also performed a confirmatory analysis using the KL-distance method, included in the Supplemental Materials section (Tort, R. Komorowski, et al., 2010).

2.3.1. Significant xPAC Occurs in Memory Encoding

For the initial quantification of xPAC, we utilized two different theta and gamma frequency bands based upon previous observations (B. C. Lega, Jacobs, et al., 2012; B. Lega, J. Burke, et al., 2014). We separately extracted phase information for the slow-theta (2-5 Hz) and fast-theta (5-9 Hz) frequency bands in the hippocampus and amplitude information for the high gamma (70-100 Hz) and low gamma (30-70 Hz) bands in the cortex then calculated xPAC separately for successfully and unsuccessfully encoded memory items for each hippocampal-cortical electrode pair. We used a mixed effects model (MEM, subject as random effect) to contrast xPAC measured during SuE and UnsuE. Results in 2.4 show significant connections (FDR corrected $p < 0.05$ in MEM). We additionally required that all connections shown in 2.4 remained significant when including only individual connections for which the larger magnitude condition (e.g., SuE for red connections) exhibited MI values significantly greater than chance (z value of 1.96). This criterion was used to ensure functional effects were not driven by non-significant xPAC. Plots of MI values by region are available in

Supplemental Materials. The functional effects for hippocampal-ERC/PHC identified by our MEM, are shown in the bar plots in Figure 2.4, split for anterior and posterior hippocampus. Additionally, we used another, convergent method to characterize xPAC patterns across the cortex. Functional xPAC between hippocampus and ERC/PHC were also shown to be significant using this alternative approach in which we compared distributions of MI values for SuE vs UnsuE at the subject level using a t-test with associated shuffle procedure (FDR corrected $p < 0.05$). These results are found in Supplemental Materials.

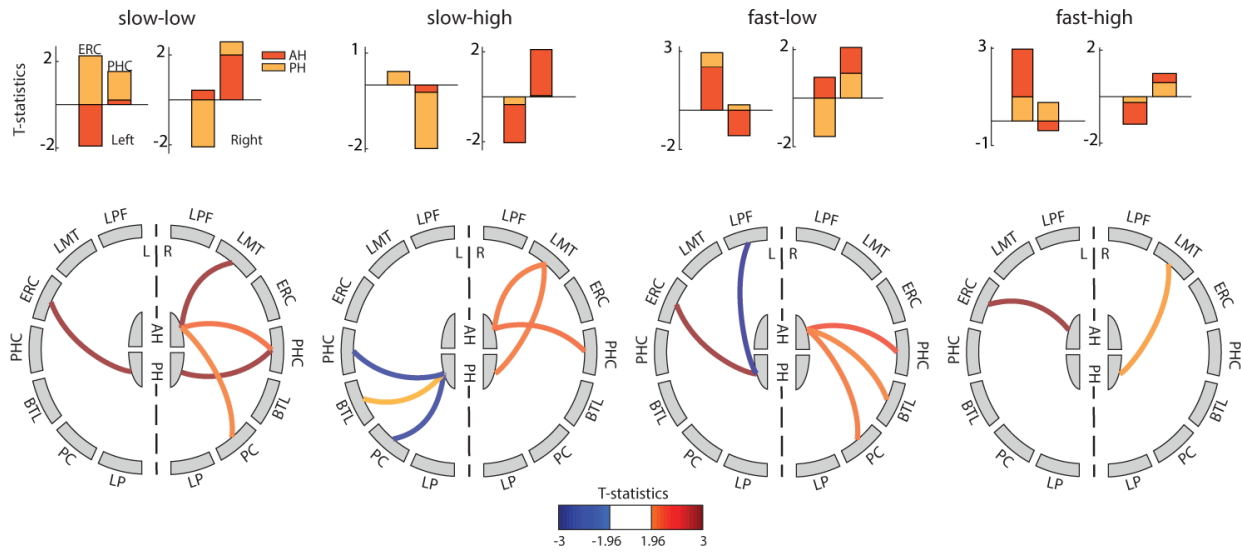


Figure 2.4: Significant functional (SuE versus UnsuE) xPAC connections, identified by mixed effects models. For all significant connections, xPAC also had significantly greater magnitude than expected by chance (MI $Z > 1.96$). Left and right hemispheric connections are shown on each side of circle connectivity plots.

We further tested the functional xPAC effects for the ERC/PHC as compared to other brain regions. We computed the MI difference (MI during SuE - MI during UnsuE) for ERC and PHC versus the five other regions across all theta-gamma connections using a permutation procedure. Results showed hippocampal-ERC/PHC connections had significantly greater functional MI difference as compared to all other regions ($p = 0.002$, MI differences with shuffle procedure). This result is visible in Figure 2.5. Moreover, we calculated the proportion of hippocampal-ERC/PHC electrode pairs that exhibited significant effects when

contrasting SuE/UnsuE distributions within each electrode pair (FDR correct $p < 0.05$, comparing distribution of trial-level xPAC values between encoding conditions). On average, $62.17\% \pm 17.04\%$ of the subjects had at least one electrode pair that exhibited significant hippocampus-ERC/PHC xPAC effects. Results for all connections and frequency bands are included in the Supplemental Materials section.

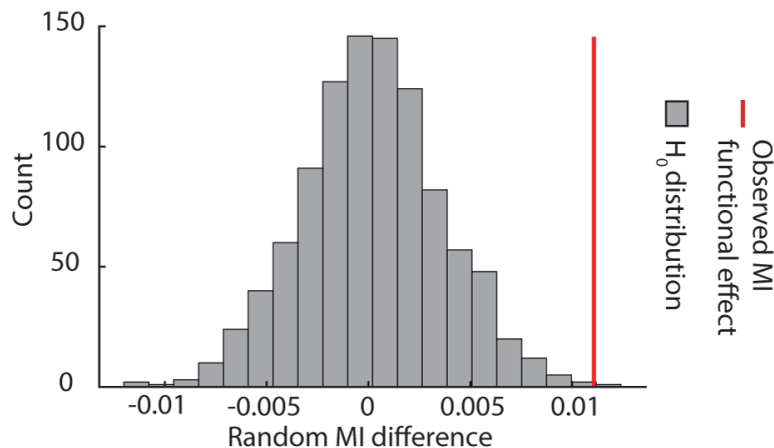


Figure 2.5: MI functional effect for the ERC/PHC versus other regions. The observed MI functional effect (red line) was obtained by comparing the distributions of MI differences (MI during SuE - MI during UnsuE) for ERC/PHC and other five regions, and the null distribution H_0 was obtained by 1000 random shuffles.

2.3.2. Detailed Examination of xPAC in the ERC and PHC.

Given the robust functional xPAC we observed between the hippocampus and ERC/PHC, we performed a more detailed analysis of the frequency/frequency interactions during successful and unsuccessful encoding as well as of the distribution of the preferred theta phase at which coupling occurs for these connections. We computed the xPAC magnitude (modulation index value) during the SuE and UnsuE conditions at each frequency-frequency pixel and compared these between memory conditions. The resulting pattern of functional effects was identified using a mixed effects model. This is shown in in Figure 2.6. We then

summarized the functional effects across the 2-9 Hz frequency spectrum, which suggest that (in aggregate) lower theta frequencies centered at 3-6 Hz exhibited decreased connectivity, as quantified by lower xPAC magnitude, for the SuE condition, while higher theta frequencies exhibited greater xPAC connectivity for SuE (in Figure 2.7). We show these more detailed data to provide a comprehensive picture of xPAC for the ERC/PHC, though these specific frequency-frequency interactions remain exploratory as compared to our principal, hypothesis-driven results which were obtained using band-limited data, as presented in Figure 2.4.

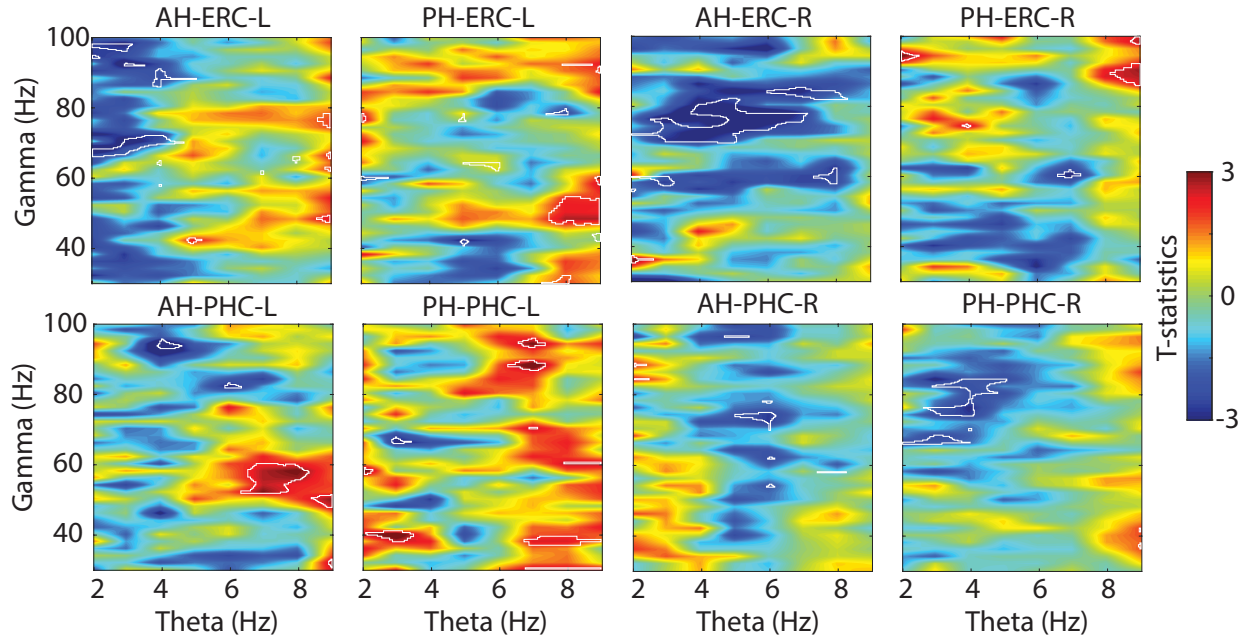


Figure 2.6: Functional effects of xPAC in the theta-gamma spectrum, shown as the t-statistic at each frequency-frequency pixel from a mixed effects model. Red indicates greater magnitude during SuE, and blue indicates greater magnitude during UnsuE. Areas outlined in white indicate the significant xPAC patterns after FDR correction across theta/gamma spectrum ($Q = 0.05$)

We further described ERC/PHC xPAC by identifying the preferred phase angle for cross-frequency coupling (Figure 2.8). We observed significant non-uniformity of the preferred phase angles for hippocampal xPAC (FDR corrected $p < 0.05$, Rayleigh test applied to the distribution of phase angles across all theta frequencies). In all cases, the phase distributions

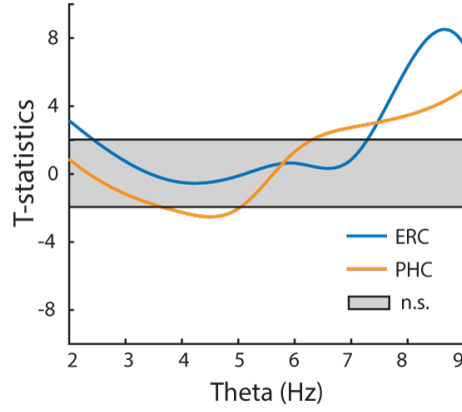


Figure 2.7: Functional effects of xPAC at each theta frequency determined by mixed effects modeling. Results reflect aggregate values across regions of interest. Functional effects are represented by T statistics extracted from the MEM, where positive values indicate greater xPAC magnitudes during SuE than UnsuE, and vice versa.

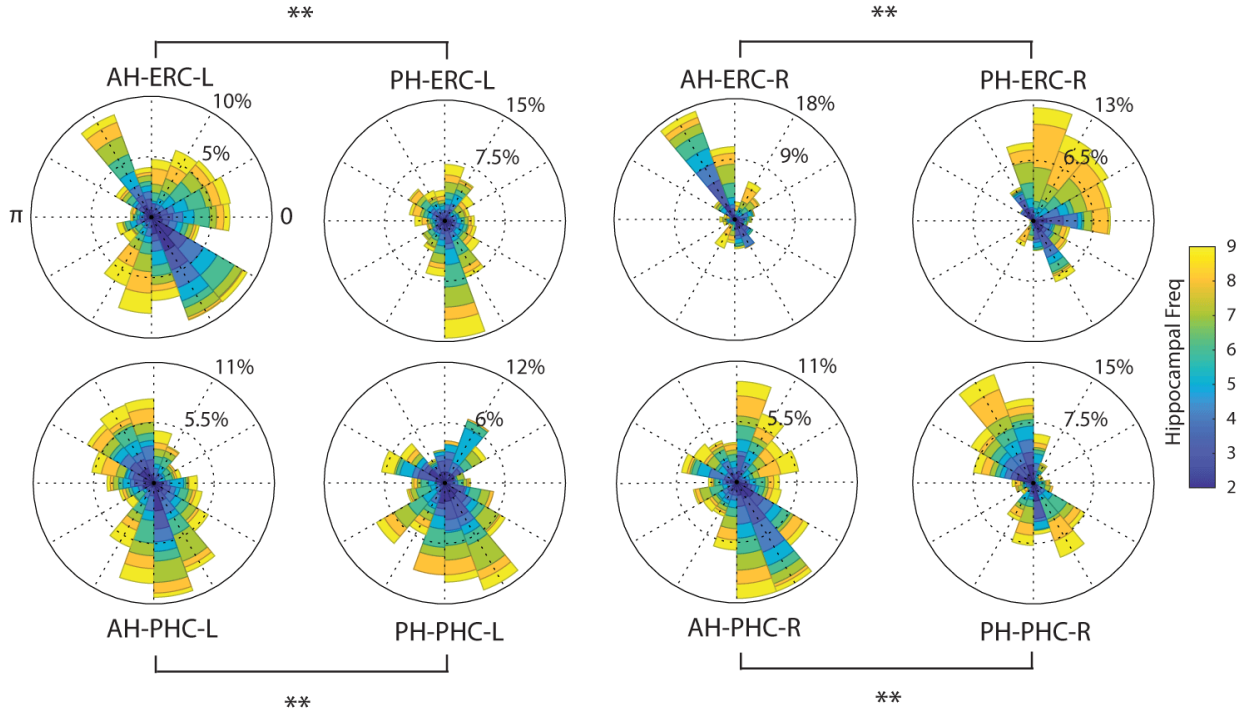


Figure 2.8: Distribution of preferred phases of xPAC during successful encoding. Preferred phases were averaged (angular mean) across trials for each significant electrode pair. Color-mapping denotes the hippocampal theta frequencies, and ** indicates $p < 0.01$ via Watson-Williams test.

were non-uniform. Figure 2.8 shows the phase distribution for significant ERC/PHC xPAC electrode pairs during SuE with both the anterior and posterior hippocampus. We then compared the distributions of preferred phase for anterior versus posterior hippocampus using the Watson-Williams test. Results showed phase distributions were significantly different between AH/PH for all ERC and PHC in two hemispheres. ($p < 0.01$, FDR corrected). In the right hemisphere, the mean preferred phase angles for anterior versus posterior hippocampus were 0.5485π vs 0.1995π for ERC connections, and -0.1655π vs 0.8296π for PHC connections. In the left hemisphere, AH coupling with the ERC clustered at phases around $\frac{2}{3}\pi$ and $\frac{5}{3}\pi$ while PH-ERC coupling clustered at phases around $\frac{3}{2}\pi$, and the mean preferred phase angles for PHC connections in the left hemisphere were clustered similarly in anterior and posterior hippocampus (-0.6511π for AH versus -0.4900π for PH).

2.3.3. AH and PH Exhibit Different xPAC Properties

Based upon models suggesting different roles for anterior versus posterior hippocampus in episodic memory, functional xPAC values along the longitudinal locations of hippocampus were compared via an n-way ANOVA, separately for each hemisphere and for the slow and fast theta frequency band, testing for an interaction between hippocampal location and memory condition (Poppenk et al., 2013; Lin, Umbach, et al., 2019). As a result, posterior hippocampal xPAC values were stronger for successful encoding (greater functional effects represented by t-statistics via ANOVA for posterior hippocampus), which was significant in the left but not right hemisphere, ($F(1, 562) = 7.65$, $p = 0.0059$ and $F(1, 351) = 1.27$, $p = 0.26$, respectively). Mean t-statistics (across regions) from the MEM are shown for anterior/posterior locations in Figure 2.9.

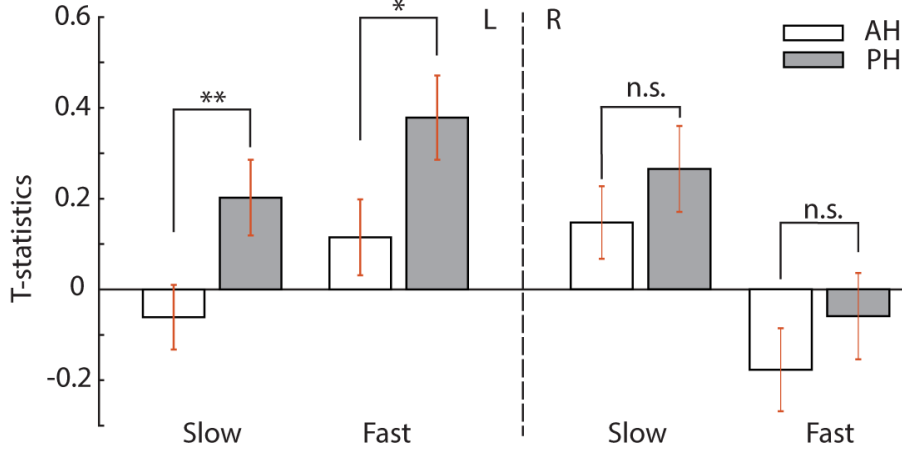


Figure 2.9: Mean t-stats describing the functional xPAC effects for slow and fast theta bands in anterior versus posterior hippocampus in two hemispheres via ANOVA. * and ** denote $p < 0.05$ and $p < 0.01$, respectively.

2.3.4. xPAC Is Not Confounded by Other Functional Measures

We tested the impact of other oscillatory properties known to affect memory encoding that could explain our observations of xPAC, both in terms of magnitude and observed functional effects. Schematic illustrations showing the procedures for these connectivity/-functional measures are shown in Figure 2.3, as the details are found in Method section. We constructed a multivariate model to test how much the factors of phase synchrony between the hippocampus and ERC/PHC and *local* PAC *within* the ERC/PHC predicted xPAC magnitude. Results are shown in Figure 2.10A, where a model was built for each cortical region (ERC/PHC in both hemispheres) with aggregation across anterior and posterior hippocampus. Figure 2.10A reports the R^2 for each predictor in each region by constructing independent models along with an interaction model (shown as PAC:PLV). Results (a minimum R^2 of 0.0009 for PLV in ERC-L, and a maximum R^2 of 0.0286 for PAC:PLV in PHC-R) showed that 1) local PAC and synchrony each account for a small fraction of the variance of xPAC across all significant connections and 2) these factors were mostly independent, as the interaction model reflects the sum of the variance explained by each factor separately.

This finding suggests that, in terms of xPAC magnitude, our observations of xPAC are not readily explained by the factors of phase synchrony and local PAC.

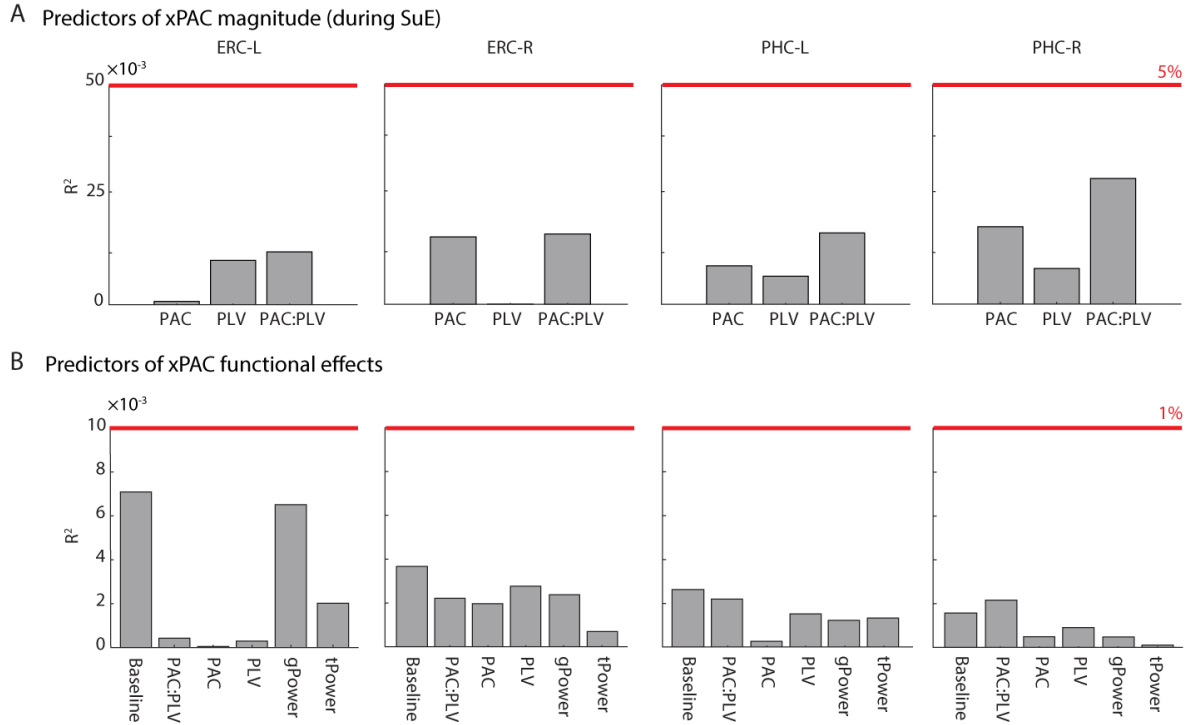


Figure 2.10: **A.** Predicting models of xPAC magnitude during successful encoding using magnitudes of PLV, local PAC, and combined effects of PLV and PAC (PAC:PLV). The variance of xPAC magnitude explained by these predictors were all less than 5% (red line). **B.** Predicting models of xPAC functional effects. Baseline denotes the combined effects all predictors. The variance of xPAC functional effects explained by these predictors were all less than 1% (red line).

Additionally, we tested how well the functional effects (SuE vs UnsuE differences) of PLV, local PAC, cortical gamma power differences (in the ERC/PHC), and hippocampal theta power differences (in the AH/PH) predicted our functional xPAC observations for the ERC and PHC (xPAC SuE vs UnsuE differences). Models were built for individual cortical regions with data (xPAC, PLV, and theta power differences) aggregation across hippocampi. Results are shown in Figure 2.10B, where baseline R^2 indicates the coefficient of determination of the full model (including all predictors), and R^2 for each predictor was

computed by an independent predicting model (also including a local PAC/PLV interaction model). As with prediction of xPAC magnitude described above, the variance explained by these factors was quite modest (a minimum R^2 of 0.0001 for PAC in ERC-L, and a maximum R^2 of 0.0071 for the full model in ERC-L), for both full and individual models.

We also tested for the impact of spurious xPAC attributable to the nature of the underlying theta waveform (in the hippocampus) used for computing xPAC. Lozano-Soldevilla et al. recently raised concerns about the effect of non-sinusoidal (clipping distorted theta) waveforms on measured PAC (Lozano-Soldevilla et al., 2016). We note that for xPAC, this effect is diminished (assuming a lack of hippocampal-ERC/PHC theta phase synchrony for xPAC recording locations, as demonstrated above) because gamma oscillatory measurements are performed at a separate brain location than theta measurements, meaning that spuriously detected theta/gamma relationships, due to theta harmonics, are less likely to occur. Stated another way, local PAC is more susceptible to this issue than xPAC, since the signal from which phase is calculated (theta oscillations) and the signal from which amplitude is calculated (gamma oscillations) are not recorded from the same place. Nonetheless, we implemented a recently published method for morphological characterization of input oscillatory data by computing the sample entropy as described in Vaz et al., 2017 and Richman and Moorman, 2000 to test how often our data include 'sharp oscillations' that can lead to spurious PAC measurement (characterized by low sample entropy). We found that 86.83% of our trials had a sample entropy greater than 0.4, and 3.41% of trials had a sample entropy less than 0.25 (in practical terms, a sample entropy exceeding 0.4 is likely to indicate nested oscillations while less than 0.25 indicates sharp oscillations in Vaz et al., 2017). The sample entropy for our trials were 0.7782 ± 0.3100 . We then recalculated our xPAC results excluding 20% of electrode pairs (17.5 ± 5.9 out of 86.8750 ± 29.06) that had lowest sample entropy. Using a linear regression model for comparing the recomputed xPAC with our original xPAC, we found that the functional effects of xPAC in the theta-gamma spectrum were minimally impacted. Resulting R^2 was 0.8388 ± 0.0577 (a minimum of 0.7248 for AH-PHC in the right,

and a maximum of 0.8961 for PH PH-ERC in the left) for the relationship between our original results and the xPAC excluding lower sample entropy pairs. Thus, we believe our quantification of xPAC was primarily based on hippocampal-cortical nested oscillatory relationships rather than sharp oscillations or any higher order harmonics of theta frequencies in the gamma band.

2.4. Discussion

We describe the phenomenon of cross regional phase amplitude coupling (xPAC) between the hippocampus and 7 neocortical regions as human subjects encode episodic memories. Our key findings are that: 1) significant xPAC occurs between the hippocampus and cortex, especially for other mesial temporal regions (ERC and PHC) 2) xPAC supports successful memory encoding, including when using methods that account for potential confounding effects such as phase synchronization, gamma power changes, and within-region PAC 3) in the left hemisphere, posterior hippocampal xPAC with the ERC and PHC was stronger than for the anterior hippocampus and 4) the preferred phase of coupling for xPAC differs between the anterior and posterior hippocampus for several connections.

The appeal of the xPAC phenomenon is that it provides a mechanism for the organization of activity across brain regions. PAC within the hippocampus and neocortex has been reported in numerous rodent and human studies, with an important distinction between slow and fast gamma activity observed during memory behavior (Colgin, 2015). PAC in general is thought to be important partially because the timing of spiking activity relative to the theta cycle influences long term potentiation (Dan and Poo, 2006; Feldman, 2012) and so xPAC between regions may promote the appropriate integration of item information into context or facilitate the ‘indexing’ function central to the hypothesized role of the hippocampus in memory formation (Preston and Eichenbaum, 2013; Backus et al., 2016; Schlichting and Preston, 2015). This conception of xPAC matches rodent data demonstrating that hippocampal theta phase may organize memory-related prefrontal spiking activity

(Jones and Wilson, 2005; Hyman et al., 2005). For this reason, the identification of xPAC represents an important contribution to the study of human memory. We believe it is noteworthy that we observed strong xPAC for ERC/PHC with the hippocampus because of the direct anatomical pathways that facilitate communication between these regions (Witter et al., 2000; Canto et al., 2008). Hippocampal-cortical xPAC beyond these regions may be less apparent in our results secondary to the inclusion of these regions for which coupling was quite strong, but the robust ERC/PHC xPAC fits with a priori expectations based on predicted interactions between these regions. Indeed, the characterization of ERC/PHC to *cortical* xPAC in subsequent investigations will further elucidate how this mechanism supports episodic memory (Eichenbaum, Schoenbaum, et al., 1996; Preston and Eichenbaum, 2013; J. Basu and Siegelbaum, 2015). We note that the existence of xPAC does not necessarily imply directional *causal* control. The version of interregional xPAC described by Knight and Canolty (Canolty and Knight, 2010) proposes a model by which synchronous theta oscillations and local PAC organize cortical activity relative to the hippocampus, with interregional xPAC observed as a subsidiary consequence of this organization. However, we did not observe especially strong overlap between functionally synchronous connections in the cortex and the magnitude of xPAC (Figure 2.10). More selective filtering of cortical contacts based upon PLV values may however reveal such connectivity (consistent with the Knight and Canolty model). The ERC/PHC xPAC relationships we observed in the absence of functionally significant synchrony may be consistent with a model in which xPAC reflects the previously reported mechanism of memory encoding modulation via the precise timing of the arrival of information from the ERC (as represented by gamma band activity) relative to the hippocampal theta oscillation (Hasselmo et al., 2002; Schomburg et al., 2014). Further characterization of this hypothesis includes extension of our xPAC analysis to the period of memory retrieval, potentially incorporating alternative (cued) paradigms better suited to the analysis of retrieval-related oscillations. This may reveal differential preferred phase values for coupling, consistent with the separate phases at encoding and retrieval, or

SPEAR model, articulated by Hasselmo (Hasselmo et al., 2002) and supported by evidence in rodents (Manns et al., 2007; Colgin et al., 2009). Data from an animal model point to hippocampal modulation of memory-relevant spiking activity in the frontal cortex, a result suggesting that testing for xPAC in prefrontal regions (which were not well represented in our sample) may provide more definitive evidence consistent with the SPEAR model (Hyman et al., 2005).

Our analysis separated the theta band into two sub-bands (termed 2-5Hz 'slow theta' and 5-9Hz 'fast theta') to account for potential differences across this spectrum seen in previous human investigations (B. C. Lega, M. Kahana, et al., 2011; Rutishauser, Ross, et al., 2010; Steinvorth et al., 2010; Fell et al., 2011; Watrous et al., 2013). Memory-related effects in the 2-5 Hz range have previously been reported during episodic memory encoding (Lin, Rugg, et al., 2017; B. C. Lega, Jacobs, et al., 2012), spatial memory encoding and retrieval (Ekstrom et al., 2005), and recognition memory tasks (Rutishauser, Ross, et al., 2010). However, phase locking of single unit activity in the 5-9 Hz range reportedly may differ according to rated confidence in a recognition memory paradigm (Rutishauser, Ye, et al., 2015), and oscillatory differences in this band (such as phase reset and cross frequency coupling) may support working memory (Chaieb et al., 2015; Mormann et al., 2005; Axmacher et al., 2010). A slow/fast theta distinction is further supported by recent findings incorporating spatial memory data, which specifically delineate separate functional properties for oscillations in the slow versus fast theta frequency range (Goyal et al., 2020), as well as hippocampal connectivity data supporting the existence of distinct fast versus slow theta oscillation networks (Choi et al., 2020). However, not all previous studies have used a demarcation exactly at 5 Hz; Goyal, for example, uses 4.5 Hz as a cutoff and extends the fast theta range to 11 Hz, while others do not segregate data into bands. We note that the slow theta frequency range, including for example the oscillations as shown in Figure 2.2, are lower in frequency than typical PAC measurements in rodents. Our results can help further

explicate inter-species differences in memory-relevant hippocampal theta activity (Jacobs, 2014).

One of the key limitations of our study is the relatively coarse regional aggregation we performed. Further investigations using more precise anatomical localization may reveal more subtle xPAC patterns. We note however that this aggregation did not influence results for the ERC/PHC as strongly given the smaller volume occupied by these regions (with presumably less inter-subject heterogeneity in the underlying signals). This may explain why we observed stronger effects for those regions. Our dataset did not contain sufficient anatomical specificity to examine medial versus lateral ERC/PHC effects, which rodent data suggest may reveal important functional differences (Kerr et al., 2007; Furtak et al., 2007). This is an important point to address in future experimentation, as rodent findings suggest differential lateral versus medial ERC modulation of spiking activity by theta oscillations (Deshmukh et al., 2010), which may have implications for the integration of item (LEC) and contextual (MEC) information in the hippocampus (Knierim, 2015).

In our results, functional xPAC occurs across the theta frequency spectrum. We believe this further supports the idea that human memory requires the dynamic interaction of both slow and fast theta oscillations, influenced by regional and hemispheric factors (Canolty, Edwards, et al., 2006; B. Lega, J. Burke, et al., 2014; Axmacher et al., 2010; Backus et al., 2016). This finding of theta heterogeneity is also supported by findings from Tort indicating that hippocampal-striatal xPAC occurs at multiple frequencies from 3 to 11 Hz (Tort, R. W. Komorowski, et al., 2009). Certainly, we acknowledge that the choice to demarcate fast versus slow theta oscillations at 5 Hz risks missing more subtle patterns that may be observable using a case-by-case identification of preferred theta frequencies for memory-related activity. Future investigations of xPAC may incorporate updated oscillation detection algorithms to delineate frequency ranges for fast and slow theta oscillations on an electrode-by-electrode basis, which could uncover more subtle patterns (Cole and Voytek, 2019).

Using a multivariate model, we attempted to differentiate memory-related effects attributable to xPAC versus those attributable to local PAC. We note that the existence of local PAC in the absence of phase synchrony does not explain xPAC, and if local PAC and hippocampal xPAC occur at slightly different frequencies, this finding may provide an explanatory mechanism for observed divergence between preferred hippocampal theta frequencies exhibiting mnemonically-relevant properties (2-5 Hz) and cortical regions exhibiting properties across a broader range of theta frequencies (B. Lega, J. Burke, et al., 2014; Backus et al., 2016; Canolty and Knight, 2010; Axmacher et al., 2010; Foster and Parvizi, 2012). Overall, the specific interactions between local PAC and xPAC remains a fruitful avenue for further investigation, especially for noteworthy xPAC connections seen in Figure 2.4 such as hippocampus-PHC.

We specifically compared xPAC for the anterior versus posterior hippocampus. In the left hemisphere, the stronger functional xPAC effects in the posterior hippocampus may reflect more spatially coherent theta oscillations within the posterior hippocampus (leading to clearer identification of xPAC across electrodes) or a preferred septo-temporal propagation for these oscillations. The latter idea is further supported by the phase offset for preferred PAC coupling phase shown in Figure 3, as AH coupling mostly occurred later in the theta cycle (although the phase offset was greater than previously seen for coherent AH vs PH theta oscillations Zhang and Jacobs, 2015). We note also that the lack of AH/PH distinction in the right hemisphere may reflect the verbal memory task we used, although hemispheric differences in hippocampal activity have mostly not been observed in free recall (J. F. Burke et al., 2014; Sederberg, M. J. Kahana, et al., 2003a), and therefore further examination of xPAC using spatial memory paradigms may prove insightful to explicate these differences. A recently articulated model of memory processing, the posterior medial/anterior temporal model (PMAT), posits that the PRC and ERC participate in different cortical networks, and if one extends this model to AH/PH distinctions, our findings of functionally significant PH/ERC coupling would seem surprising as the ERC is clearly identified within the AT but

not PM network (Ranganath and Ritchey, 2012; Ritchey et al., 2015). However, it is also possible that the entire hippocampus, both AH and PH, participate in both networks given its central role in mnemonic processing (Choi et al., 2020). Furthermore, this model relies mostly on non-invasive data collected during item retrieval and therefore may not apply as strictly to data collected during memory encoding, as we present here.

The quantification of PAC has been the topic of extensive discussion in the human electrophysiology literature. Several different methods have been used in high profile publications. While our main findings follow the MI calculation described by (Canolty, Edwards, et al., 2006), we also tested our results using other methods for PAC quantification, namely MI by KL-distance as a measure of the dependence of hippocampal theta and cortical gamma, and implemented recommended steps in PAC calculations such as filter bandwidth (Tort, R. Komorowski, et al., 2010; Aru et al., 2015; Vaz et al., 2017; Richman and Moorman, 2000; Lozano-Soldevilla et al., 2016). Our main findings regarding xPAC between hippocampal theta oscillations and ERC/PHC gamma oscillations were mostly supported by results performed using KL distance, although KL methods were less effective at establishing functional patterns. In addition, the coupling phase in KL-distance was difficult to track precisely due to the estimation of amplitude-phase distribution. Furthermore, we attempted to directly test and control for the impact of theta waveforms leading to spurious detection of PAC activity in our data. As discussed in the Results section, in xPAC the underlying waveform in theta does not influence the measurement of the phase dependence of gamma oscillations in the non-hippocampal region (ERC/PHC). Therefore, we believe xPAC is less sensitive to this concern than local PAC as long as one accounts for possible effect of phase synchrony (established in Figure 2.10). However, using published criteria for exclusion of sharp oscillations and clipping distortion in the hippocampus, we still observed significant xPAC. Certainly, methods to account for non-sinusoidal underlying waveforms remain an active area of investigation.

2.5. Additional Analysis of Brain Functions

Distinct Neurophysiological Correlates of the fMRI BOLD Signal in the Hippocampus and Neocortex.

The blood oxygenation level-dependent (BOLD) signal forms the basis of functional magnetic resonance imaging (fMRI) but provides only an indirect measure (i.e. no measure of neural, electrical or chemical changes) of neural activity. Task-related modulation of BOLD signals are typically equated with changes in gamma-band activity; however, relevant empirical evidence comes largely from the neocortex. We examined neurophysiological correlates of the BOLD signal in the hippocampus, where the differing neural architecture might result in a different relationship between the respective signals. We identified a positive relationship between encoding-related changes in BOLD and gamma-band activity in the frontal and parietal cortices. This effect was reversed in the hippocampus, where BOLD and gamma-band effects negatively correlated. These results suggest regional variability in the transfer function between neural activity and the BOLD signal in the hippocampus and neocortex.

In the study, 15 patients with medically resistant temporal lobe epilepsy (TLE) implanted with depth electrodes performed a free recall task while iEEG was recorded simultaneously from hippocampal and neocortical sites. Then, the same patients subsequently performed a similar version of the free recall task in a later fMRI session (Hill, King, et al., 2020). Then, subsequent memory effects (SMEs) were computed from the fMRI BOLD, iEEG gamma band, and iEEG theta-to-gamma phase-amplitude coupling, as patterns of encoding-related brain activity. SME is a measure of standardized mean difference of a neural activity between

Copyright clearance: this is a joint work with Dr. Paul F. Hill, the Department of Psychology, University of Arizona, Tucson, Arizona. This work has been published in Hill, Seger, et al., 2021 in the Journal of Neuroscience (<https://www.jneurosci.org/content/41/29/6343>). Permission of reuse of the published content in this dissertation is granted by the publisher (copyright holder). License ID: 1211866-1.

subsequently recalled (R) and not recalled (NR) memory items, given by:

$$SME = \frac{\mu_R - \mu_{NR}}{\sqrt{(\sigma_R^2 + \sigma_{NR}^2)/2}} \quad (2.7)$$

where μ and σ^2 are the across trial mean and variance, respectively. We used mixed effects modeling (as described in 2.2) for investigating the correlation between fMRI BOLD and a variety of neural activity including oscillatory power in the delta (2–4 Hz), theta (4–8 Hz), alpha (8–12 Hz), beta (12–30 Hz), low gamma (30–70 Hz), and high gamma (70–150 Hz), as well as phase-amplitude coupling between theta and low/high gamma bands, in the hippocampus, frontal lobe, medial temporal lobe, parietal lobe, and temporal lobe. By analyzing the functional effects via MEM between BOLD and LFP power and PAC in hippocampus and neocortices, we found

1. Coupling between BOLD and LFP SMEs varies across brain regions and frequency bands.
2. BOLD and gamma band SMEs are negatively correlated in the hippocampus and parahippocampal gyrus.
3. Coupling between memory-related BOLD and iEEG activity in the MTL and parietal cortex is moderated by the direction of BOLD effect.
4. Frontal BOLD effects are differently predicted by early and late components of delta- and theta-band activity.
5. Theta-to-gamma phase amplitude coupling predicts unique variance in neocortical BOLD SMEs.

In conclusion, we identified a robust positive relationship between encoding-related BOLD and high gamma activity in the frontal and parietal cortex, replicating findings from numerous prior studies (Ekstrom, 2021; Ojemann et al., 2013). It is important to note that this

relationship was reversed in the hippocampus, where BOLD SMEs negatively covaried with both low and high gamma SMEs. Future research will be required to address the interesting question of whether these findings vary at the level of hippocampal subfields. Nonetheless, the present results suggest that the neurophysiological correlates of the BOLD signal in the hippocampus differ from those in the neocortex.

CHAPTER 3

DEVELOPMENT OF BINARY-NOISE DEEP BRAIN STIMULATION

3.1. Introduction

As a neurosurgical and therapeutic procedure, deep brain stimulation (DBS) has provided invaluable benefits for patients who suffer from a diversity of neurological conditions. Through implanted electrodes, DBS therapy is achieved by a neurostimulator, sending electrical pulses to specific target brain region(s). In the past two decades, DBS has been FDA-approved for clinical use and has been found effective in treating a variety of brain dysfunctions such as Parkinson’s disease (Deuschl, Schade-Brittinger, et al., 2006; Benabid, 2003), depression (Malone Jr et al., 2009), obsessive compulsive disorder (Greenberg et al., 2006), and epilepsy (Fisher et al., 2010). While the basic principle of DBS is to evoke and excite neural activities (e.g. spikes) within a certain group of neurons surrounding the intracranial contact(s), the underlying mechanisms are not fully understood. Thus, DBS studies are often done in a controlled manner and sometimes with blinded studies (Dostrovsky and Lozano, 2002; Kringelbach et al., 2007). For movement disorders such as Parkinson’s disease, DBS targeting subthalamic nucleus (STN) or the internal segment of the globus pallidus (GPi) has been a routine procedure to restore neuromotor function thanks to the strong anatomical and pathophysiological understanding of the basal ganglia (Kringelbach et al., 2007; Breit et al., 2004; Perlmuter and Mink, 2006). However, for neurodegenerative and neuropsychiatric conditions such as Alzheimer’s disease, epilepsy, memory loss, and depression, the underlying neural circuitry is more complex and difficult to predict anatomically. Thus, a point of departure of our understanding the effectiveness in these dysfunctions is to compare the therapeutic outcomes with a particular DBS strategy, which includes determination of

target area and stimulation parameters such as stimulus amplitude, frequency, waveform, etc.(Kringelbach et al., 2007; Hickey and Stacy, 2016). This raises a general question of whether DBS excites or inhibits a neural activity targeting the treatment of a particular brain condition.

For treating memory dysfunction, DBS techniques have come a long way ever since the first attempt in patients with Alzheimer’s disease in 1985 (Turnbull et al., 1985) and a tried-and-true strategy has yet to be established. With a range of stimulation targets including fornix, entorhinal cortex, hippocampus, cingulate, precuneus, frontal cortex, and basal nucleus (Toda et al., 2008; Stone, Teixeira, DeVito, et al., 2011; Stone, Teixeira, Zaslavsky, et al., 2011; Laxton, Tang-Wai, et al., 2010; Suthana et al., 2012; Jacobs, J. Miller, et al., 2016), results in memory performance are mixed. For instance, Suthana et al. describes a DBS strategy targeting spatial memory enhancement by stimulating the entorhinal cortex versus the hippocampus via charge-balanced biphasic rectangular pulses. While participants were performing a behavioral paradigm of spatial navigation, stimuli were applied to one of the controlled target regions for 5 s on and 5 s off. They reported memory was enhanced by stimulating the entorhinal cortex whereas hippocampal stimulation was not effective (Suthana et al., 2012). Interestingly, in a similar behavioral paradigm, Jacobs, J. Miller, et al. reported that stimulating the entorhinal area and the hippocampus with different stimulation parameters worsened both spatial memory and episodic memory, whereas stimulating the hippocampus significantly decreased the chance of memory encoding (Jacobs, J. Miller, et al., 2016). Moreover, in rodents, Heschem et al. applied a combination of stimulus frequencies and amplitudes for testing the DBS effects on memory against scopolamine and reported that stimulus current density might be more critical than stimulus frequency in restoring memory functions, in a controlled configuration (Heschem et al., 2013). Despite the stimulation parameters, individual tolerance and sensitivity to electrical stimulation may be as important and such DBS in open-loop format may require custom sessions for determining DBS parameters, if proven effective in the first place.

Here, our goal is not to develop an open-loop DBS paradigm for restoring memory functions directly, rather, we seek to provide a DBS strategy that benefits our subsequent development of a closed-loop brain-computer interface system for precisely governing the DBS applied to the target region in order to achieve neuromodulation of memory-relevant brain functions. From a preliminary study, the posterior cingulate cortex (PCC) has been shown to have a distinct role in modulating hippocampal activity and stimulating PCC affects hippocampal theta and gamma oscillatory power during a memory task (Natu et al., 2019). Thus, it is reasonable for us to expand this direction by implementing a recently reported stimulation waveform called binary-noise, due to its superior performance in identifying a dynamic system, compared to a traditional rectangular or sinusoidal waveform (Yang, Connolly, et al., 2018). In this dissertation, stimulation applied to the PCC during a free recall (FR) paradigm was used as described in Chapter 4. A binary-noise (BN) stimulation was applied to the PCC in the study described in Chapter 5. This chapter aims to unveil our development and implementation of BN stimulation using devices manufactured by Blackrock Neurotech in a preclinical research configuration. More importantly, we wish to address technical challenges in implementing this stimulation paradigm and expose our hardware and software configurations for inspiring development of similar randomized stimulation patterns.

3.2. Participants and Implantation

The human participants in the stimulation tasks were medication-resistant epilepsy patients from Dr.Lega’s epilepsy surgery practice with the goal of identifying their ictal onset region(s) and recruited at the epilepsy monitoring unit (EMU) at the University of Texas, Southwestern Medical Center, Dallas. A variate of memory-relevant behavioral tasks (such as ordinary free-recall and associated recognition tasks) were performed during a stay span of approximately a week with their informed consent. The participants were implanted with stereo-electroencephalography (sEEG) platinum-iridium recording electrodes to detect seizure location. The number and location of the intracerebral electrodes implanted in the

patients were determined exclusively based on the clinical need (an example of reconstructed electrodes locations is found in Figure 3.1), and only patients who had electrodes implanted in the posterior cingulate cortex participated in stimulation cognitive tasks (FR or BN stimulation). Patients' activity and intracranial-electroencephalogram (iEEG) were monitored via surveillance cameras and Nihon Kohden NueroFax clinical EEG system, respectively, by technicians and nurses at the EMU. Research protocols were approved by the UT Southwestern Medical Center Institutional Review Board on Human Subjects Research. Following patients' implantation, localization of electrodes was performed by stereotactic placement of depth electrodes and postoperative fusion of computer tomography (CT) scans with the preoperative high resolution magnetic resonance (MR) images (MPRAGE, coronally acquired 1 mm slices), and the cortical location of contacts were identified using the FLIRT auto segmentation software (<https://fsl.fmrib.ox.ac.uk/fsl/fslwiki/FLIRT>). The co-registered images were evaluated by a member of the neuroradiology team to determine the final contact locations. For stimulation tasks, all electrodes were targeted to the retrosplenial region of the PCC, using the splenium of the corpus callosum as a landmark for placement. This incorporated Brodmann areas 26, 29, 30, and the ventral aspect of area 23. On average, a participant had 2-3 contacts in the PCC and 4-8 contacts in the hippocampus, combining both anterior and posterior hippocampi.

3.3. Free-Recall Stimulation

The FR stimulation protocol was developed based on the free-recall study of the episodic memory task. In general, a session of the free-recall paradigm consists of 25 word lists, each of which comprises of 12 common English nouns. The words used in the word lists were chosen from a pool of high-frequency nouns. The entire list is available at <https://memory.psych.upenn.edu/WordPools>. There were a total of 20 lists and each list comprised of 10 words. In each list, as shown in Figure 3.2, each word is presented on a PC monitor for 1800 ms followed by a jitter time. After a distraction (math questions for 20 second and an

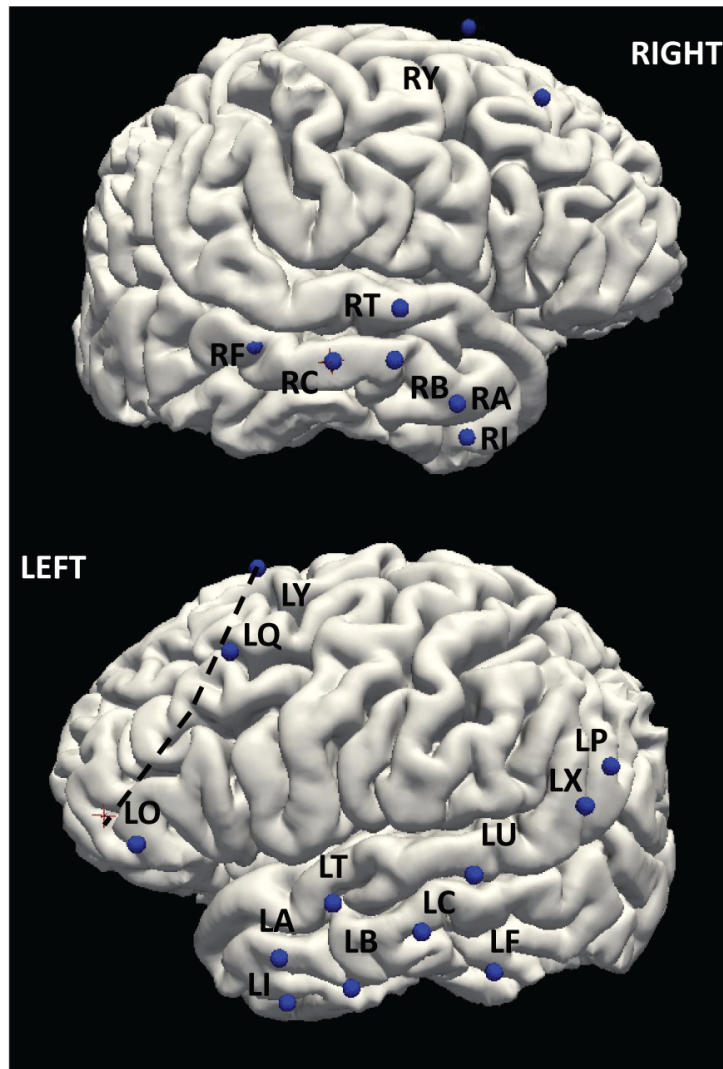


Figure 3.1: Example trace reconstructed locations of electrodes.

auditory tone of 300 ms), a 30 second interval is given for the subject to recall as many of the words as possible in any order. Vocal responses are then digitally recorded and segmented offline using Penn TotalRecall (<http://memory.psych.upenn.edu/TotalRecall>). Then, the iEEG during the encoding period are labeled as successful encoding corresponding to the recalled words and unsuccessful encoding corresponding to the not-recalled words, and only iEEG corresponding to the corrected recalled words during a retrieval period are labeled as retrieval by an annotator.

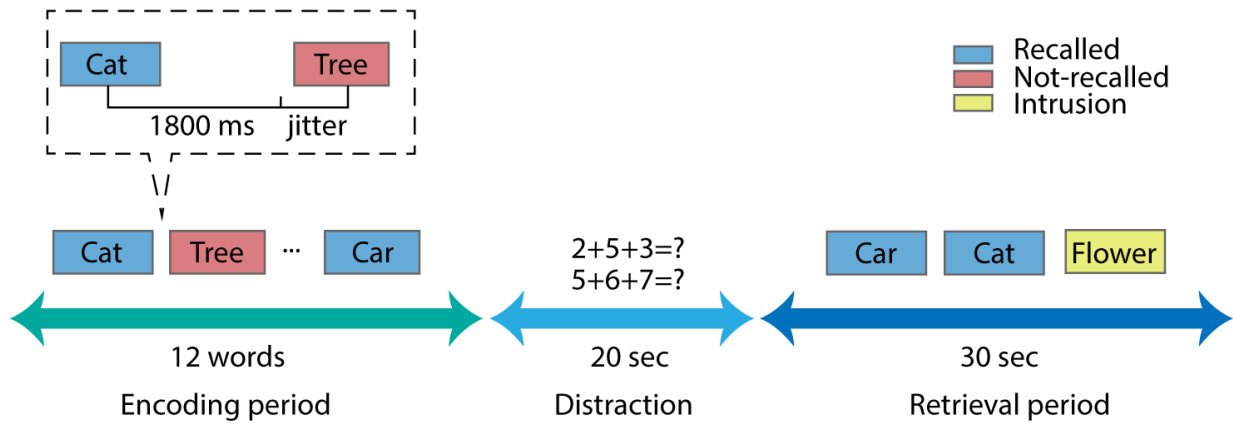


Figure 3.2: Example list of free-recall paradigm.

The free-recall stimulation paradigm applied biphasic charge-balanced electrical pulses in rectangular waveform to the PCC in a bipolar configuration during the encoding period of every other list of free-recall task. Using the Grass s88 (Grass technologies), which is a current-source stimulator, anode and cathode were connected to the deepest contacts of which had been localized to the PCC (LX1/RX1 and RX2/LX2) via a jumper cable and the stimulus was set to 2 *mA* at 100 *Hz*. The illustration of our FR stimulation using the s88 stimulator is shown in Figure 3.3. This setup of stimulation parameters was determined using a well accepted safety guideline for DBS drawn from initial work (Butson et al., 2007), and by incorporating typical parameters used for a variety of DBS development (Suthana et al., 2012; Jacobs, J. Miller, et al., 2016). The critical safety threshold for DBS that is widely accepted is 30 $\mu C/cm^2$ for short-term and 57 $\mu C/cm^2$ for long-term stimulation (Agnew and McCreery,

1990; Gordon et al., 1990). Given the surface area of implanted depth electrode of 0.05 cm^2 and with pulse width of $200 \mu\text{s}$ per phase, the electrical charge was $8 \mu\text{C}/\text{cm}^2$ per phase, which was well below the safety threshold. Stimuli were applied during the entire duration of

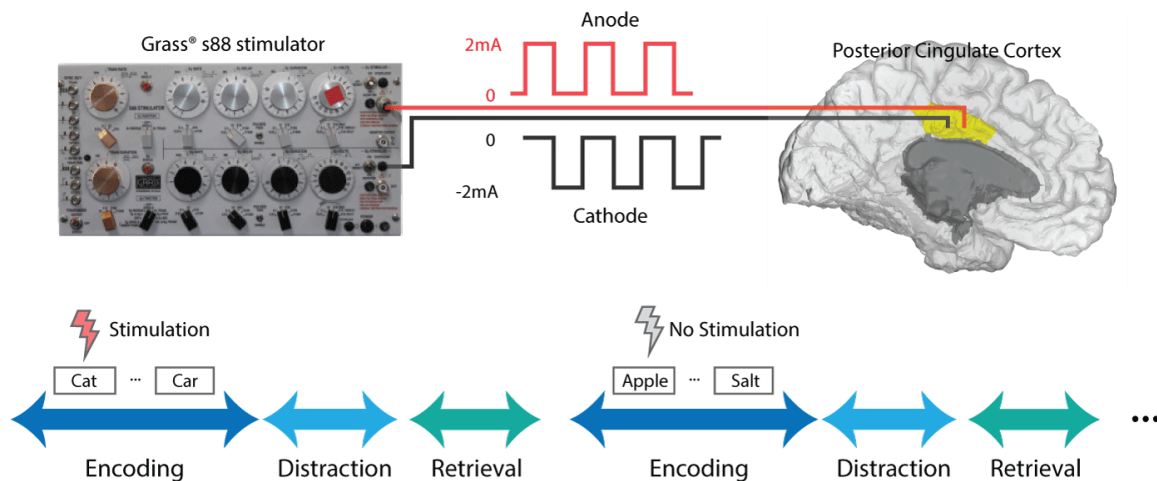


Figure 3.3: Free-recall stimulation paradigm

the encoding phase of 50% of the study lists. Stimulation to PCC was synchronized with the onset of the first word in each stimulation list and was delivered throughout the encoding period to largely avoid concerns of post-stimulation electrophysiological changes affecting oscillatory patterns of nearby items. To maintain equivalence between stimulation and non-stimulation trials, both types of trials were interleaved throughout the experimental session and items from the word pool were randomly assigned to stimulation and non-stimulation word lists with no differences in semantic content.

3.4. Binary-Noise Stimulation

With the success of modulating hippocampal oscillatory activity using DBS of the PCC, we investigated and adopted the binary noise stimulation pattern developed by Yang, Connolly, et al. specifically for dynamic modeling. This BN scheme utilizes a randomized waveform by switching stimulation parameters in the safe range to generate a white-noise-like electrical pulse pattern (Yang, Connolly, et al., 2018). Unlike a traditional rectangular wave-

forms (such as FR stimulation and theta burst stimulation), this BN pattern is constructed by alternating both amplitude and frequency between two values, following a particular distribution of a random variable. This achieves a broader and ‘flatter’ power spectral density. Assume the BN pattern has two amplitude levels A_{high} and A_{low} , at any given time $tT_{sw}(t = 1, 2, 3, \dots)$, the pattern has an equal possibilities of either remaining the current amplitude level or changing to other level such that

$$P\left(u(t) = u(t-1)\right) = P\left(u(t) \neq u(t-1)\right) = 0.5 \quad (3.1)$$

The advantage is to allow manipulation of the frequency spectrum, which is distributed equally across frequencies. One can show the asymptotic discrete-time frequency spectrum of such pattern is (H. J. Tulleken, 1990)

$$\Phi(\omega) = T_{sw}, \quad \forall \omega \in [0, \pi] \quad (3.2)$$

where ω denotes discrete-time frequency and T_{sw} is the switching time. This theoretical “white-noise” characteristic in the frequency band of interest makes BN patterns ideal for identifying a process/plant model or a test signal since all relevant process frequencies are tested with equal power levels for a more accurate frequency response of the process or system. For this reason, the BN pattern has been used extensively in industrial practices of system identification and process testing (Eykhoff et al., 1974). Thus, using this input pattern as the stimulation waveform enhances our ability to accurately model the hippocampal oscillatory power in response to PCC-applied stimulation, even without knowing the neurophysiological processes involved.

In the implementation of the BN stimulation pattern, we incorporated the Cerestim neurostimulator and neural signal processor (NSP) module, both manufactured by Blackrock Neurotech (<https://blackrockneurotech.com/research/products/>). Unlike FR stimula-

tion with the Grass s88 stimulator, which was triggered by TTL signals using a custom script integrated with our FR paradigm in Python, the BN stimulation requires randomized stimulation sequences that need to be programmed for the Cerestim. We used its software API and created a script for a pseudo-random process of switching stimulus amplitudes from 1 *mA* and 2 *mA* and frequencies from 100 *Hz* and 150 *Hz*, with a pulse width of 200 μs and a interphasic interval of 55 μs (minimum in Cerestim). This was done because it has been shown that these amplitudes were well below a clinical safety boundary (Agnew and McCreery, 1990; Gordon et al., 1990), and our primary frequency band of interest were theta and sub-100 *Hz* gamma. Our configuration for the BN stimulation paradigm is shown in Figure 3.4. It is critical to point out that the Cerestim has a memory limit, which only accepts

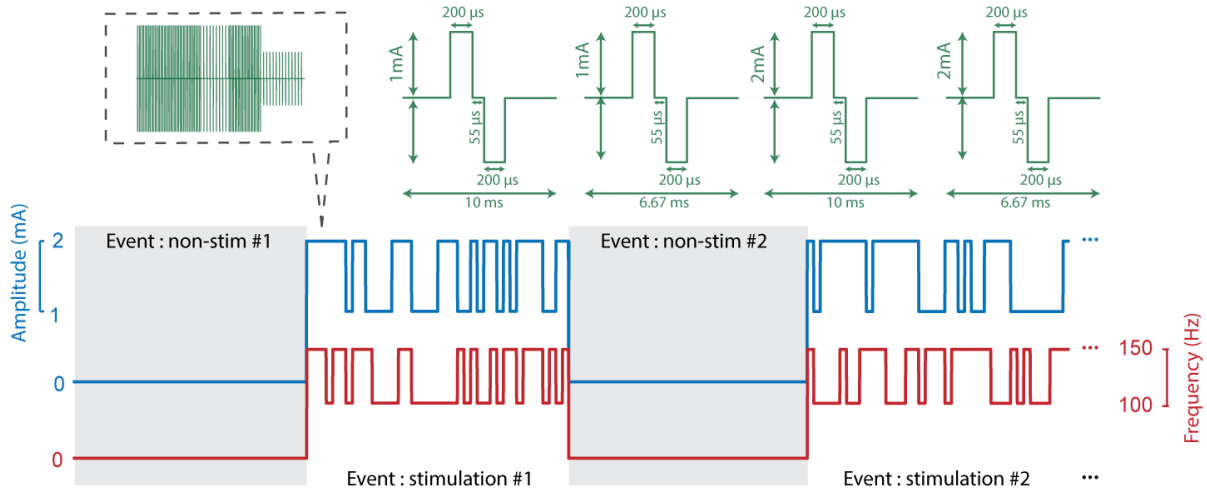


Figure 3.4: Binary noise stimulation paradigm.

and delivers a limited number of parameter-changing stimulation patterns in the API. Our best practice was to create a uniformly distributed random sequence as indicators for the stimulator to assign the predetermined stimulation parameter into the incoming pulse train. Unfortunately, there is no way to avoid this issue to date and the limitation is associated with the stimulation duration T and the minimum switch time T_{sw} , such that $T \times T_{sw} \leq 126$. Therefore, we used a minimum switch time T_{sw} of 0.02 *s* with our stimulation period of 2 *s*. In addition, a stimulator like the Grass s88 requires separate anode and cathode to deliver

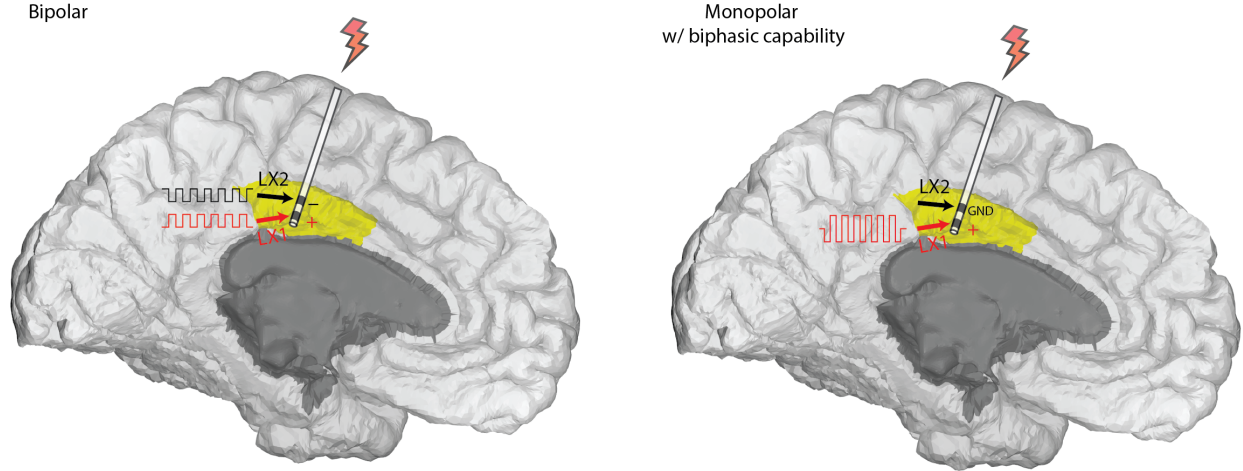


Figure 3.5: Illustration of proper configurations for bipolar and monopolar DBS.

biphasic pulse trains (i.e. bipolar) to two adjacent contacts so the charge-balanced electrical current flow through the tissues surrounding the cylindrical contacts. However, the digital Cerestim stimulator is capable of delivering biphasic pulses within each individual contact (i.e. monopolar) so that a bipolar setup introduces interference and severe artifacts if no nearby grounding is provided. To solve this, one solution is to apply two equal pulse trains to the adjacent contacts but with 180 degrees of pulse phase shift, which serves as the anode and cathode in a traditional bipolar setup (Zelmann et al., 2020). We found that this setup still exhibited enormous undesired artifacts, which might due to the system internal delay in the stimulator and API when alternating pulse phase. Our solution is to use the adjacent channel of the stimulation target as a grounding port, which sinks out excessive current. As a result, we found this approach guaranteed effective stimulation to the designated site with a similar spacial scale as using a traditional bipolar configuration, as well as eliminating the vast majority of stimulation artifact. An illustration of the proper bipolar and monopolar setups for stimulation is found in Figure 3.5.

For neural recordings, we used the Blackrock NSP module that runs in parallel to the Nihon Kohden clinical EEG monitoring system via custom made adapters and cables. The Cerestim stimulator and the NSP module were on a PC caster and bridged

by integrated software and our MATLAB scripts for simultaneously recording, stimulating, and monitoring (see Figure 3.6). We selected our regions of interest, especially for

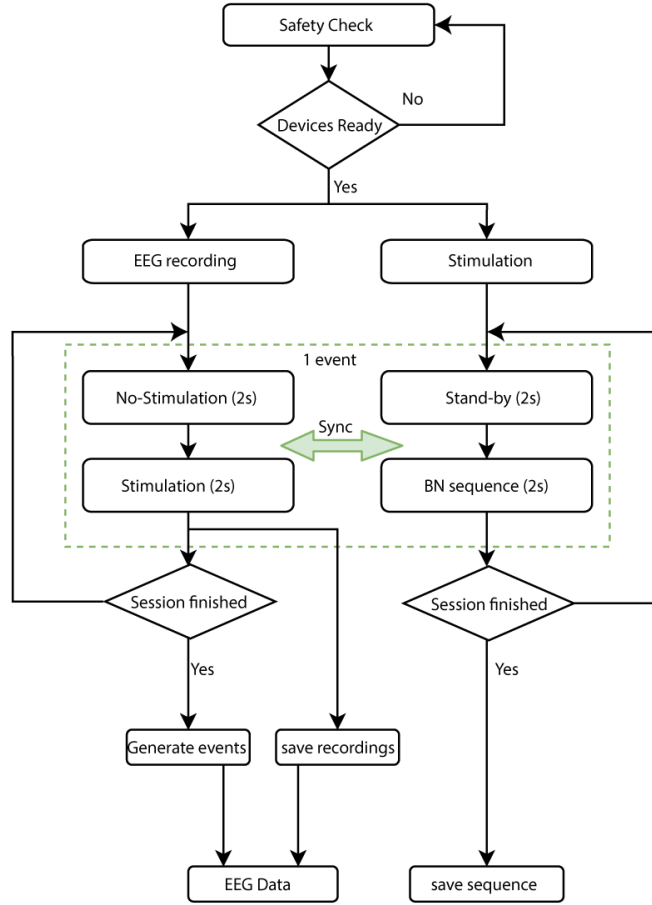


Figure 3.6: BN stimulation procedure for the stimulation and EEG acquisition.

ipsilateral regions with respect to the PCC being stimulated, using 128-channel recordings. While there was no memory-relevant task in the paradigm, participants were asked to maintain calm and have minimal physical movements while acquiring resting-state EEG signals during stimulation sessions. The EEG recordings during the paradigm were synchronized with stimulation events (i.e. stimulation versus no-stimulation) via the sync ports on both devices, then were segmented into event trials using Blackrock NMPK package (<https://github.com/BlackrockNeurotech/NPMK/tree/master/NPMK>), by referencing the sync pulse train.

3.5. Unique Solution of the Stimulation System

As mentioned, we incorporated a unique randomly generated stimulation pattern with our existing stimulator and EEG acquisition devices in conjunction of the EEG monitoring system at the EMU. We developed software and scripts on the Blackrock devices and N.K NeuroFax EEG system in the patients’ unit for this task. First, we eliminated the use of the “splitter box” made by Blackrock, which was designed to achieve both stimulation and data acquisition simultaneously within the same “modified N.K. cables” (by Blackrock as well), for stimulation tasks. This was done because this integrated splitter-cable was, in some way, an afterthought solution that allowed both stimuli and EEG signals traveling inside the cable without designated pathways, thus it dramatically failed both tasks. We came up with an isolated approach for stimulation and acquisition tasks. The EEG acquisition via the Blackrock NSP module used a “splitter box” and modified cable exclusively for recording clean EEG signals in parallel to the N. K. EEG system. Moreover, we placed a grounding on patient’s mastoid, which was connected to the GND port on the front amplifier of the NSP module, along with the “z” port (a intracranial referencing site for EEG monitoring). On the other hand, the stimulation via Cerestim used a DB44-to-jumpers adapter (a “dangle” cable) for applying BN stimulation patterns directly to individual contacts in the N.K. Jackbox (a contact hub). Besides, we highly recommend the use of an adjacent channel as the ground for stimulation as discussed previously. Our stimulation solution requires a full disconnection of the stimulation channel (with the adjacent channel) from the Jackbox for minimal artifact. The complete hardware configuration diagram is shown in Figure 3.7.

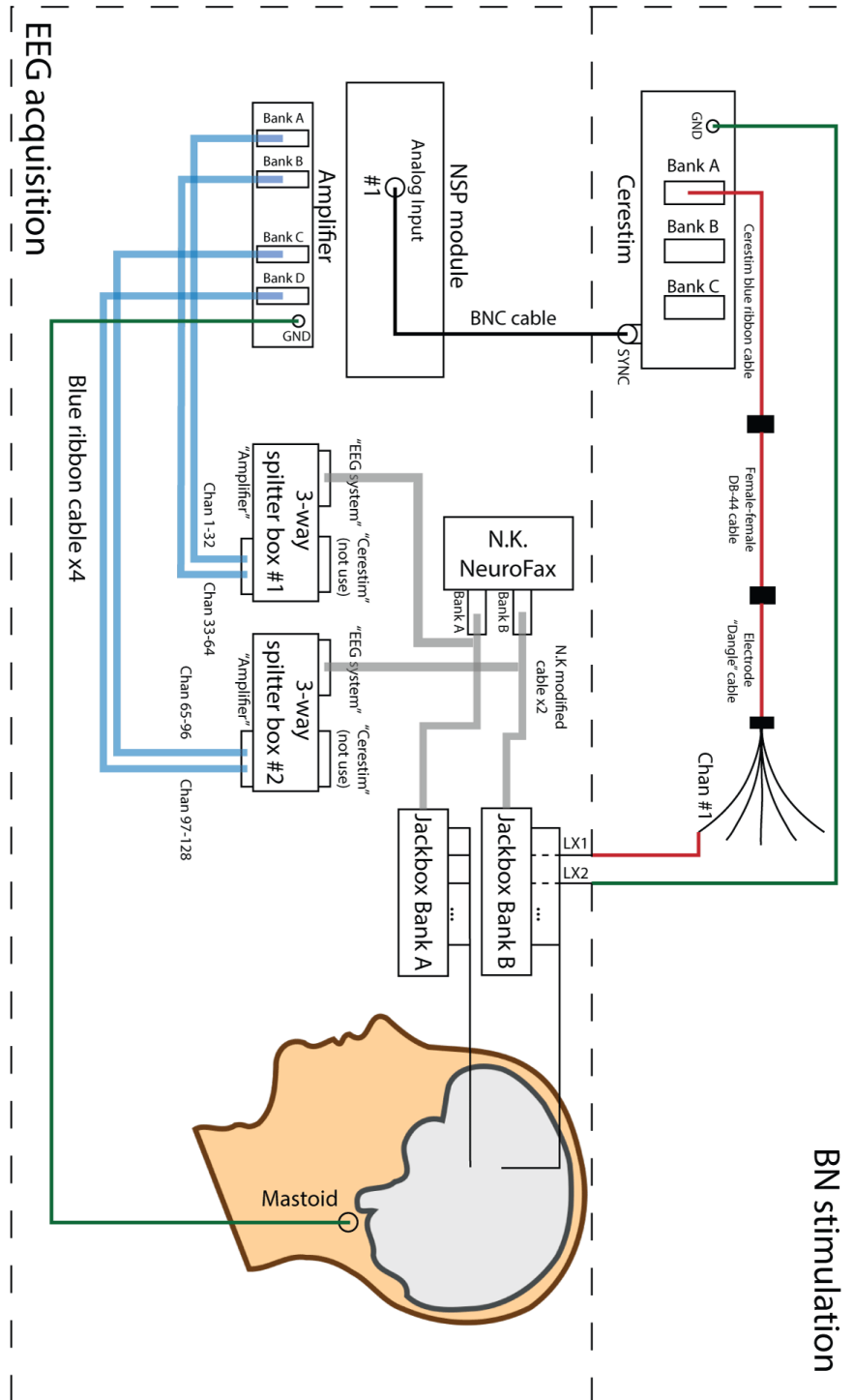


Figure 3.7: BN stimulation and EEG acquisition configuration.

The hardware set up procedure is as follows:

1. Set up Blackrock NSP module with N.K. NeuroFax system for EEG acquisition:
 - (a) Swap out the N.K. cables in between the N.K. NeuroFax and Jackboxes with modified N.K. cables for Jackbox bank A and B.
 - (b) Connect the modified N.K. cables (2 DB44 connectors for each bank) to the “EEG system” ports of both 3-way splitter boxes.
 - i. N.K. Bank A 1st DB44 – “EEG system” port 1-32 (upper) on the splitter box labeled “1-64”.
 - ii. N.K. Bank A 2nd DB44 – “EEG system” port 33-64 (lower) on the splitter box labeled “1-64”.
 - iii. N.K. Bank B 1st DB44 – “EEG system” port 1-32 (upper) on the splitter box labeled “65-128”.
 - iv. N.K. Bank B 2nd DB44 – “EEG system” port 33-64 (lower) on the splitter box labeled “65-128”.
 - (c) Connect the 3-way splitter boxes (“amplifier” ports) to the amplifier via the Blue Ribbon cables.
 - i. Amp bank A – channel 1-32
 - ii. Amp bank B - channel 33-64
 - iii. Amp bank C - channel 65-96
 - iv. Amp bank D - channel 97-128
 - (d) Place surface grounding on patient’s mastoid then connect it to the GND port on amplifier via a jumper cable.
2. Set up Blackrock Cerestim for BN stimulation:

- (a) Connect the female-female DB44 cable (as an extension) to the Cerestim blue ribbon cable (from the back panel of the Cerestim) bank A.
 - (b) Connect the DB44-to-jumper adapter (the “dangle” cable) to the other end of female-female DB44 extension.
 - (c) Unplug the jumper connector of stimulation site (e.g. LX1 for left PCC stimulation) from the Jackbox then connect it to the “dangle” cable channel 1 via a jumper connector. Note, stimulation target (e.g. LX1) and the “dangle” channel 1 should have no contact with the Jackbox now.
 - (d) Unplug the adjacent jumper connector of stimulation site (e.g. LX2 for left PCC stimulation) from the Jackbox then connect it to the GND port on the back of Cerestim. This adjacent electrode (LX2) and the GND should have no contact with the Jackbox.
3. Connect the SYNC port on Cerestim to NSP analog input port 1 via a BNC cable for sync pulses. Make sure BNC cable sits properly on both ends.

For each session, the BN stimulation paradigm was operated via our MATLAB scripts with the Cerestim API package, meanwhile, 128-channel EEG signals were recorded using the integrated Blackrock Central software. Our software configuration and procedure for the paradigm is shown as follows:

1. EEG recording via NSP central (electrode referencing is normally unnecessary, see troubleshooting section for excessive stimulus artifacts). A global Central configuration is:
 - (a) For digital channel 1-128:
 - i. Enable line-noise cancellation. LNC method: NSPIF sync, estimate time constant: 1s

- ii. Continuous Acquisition: LP 250 Hz
 - iii. Sampling rate: 1kS/s
 - iv. Spike processing: *< None >*
 - v. Disable channel referencing.
 - (b) For analog input 1 (sync pulses):
 - i. Continuous Acquisition: *< None >*
 - ii. Sampling rate: 30kS/s
 - iii. Disable rest of features
2. BN stimulation paradigm via MATLAB scripts:
- (a) Establish connection between Cerestim and PC by running script *Cerestim_connect.m*
 - (b) Set ID info for the subject and session in the stimulation script *BlackRock_BN_stim.m*
 - (c) Use 2000 (2 mA) for HighAmp and 1000 (1 mA) for LowAmp for *session_0* or other parameters for additional sessions depending on the task.

Finally, we performed the recording prior to the start of stimulation scripts. Electrophysiological activity and patient’s status were constantly monitored by our research assistant, EMU technician and nurses. Meanwhile, stimulation and EEG recording status were monitored using the built-in oscilloscope panel in the Central software for which the LC1 or LB1 channel was selected for Trace 1, and ainp1 (analog input 1) was selected for Trace 2. By doing so, we were able to monitor the hippocampal EEG and the appearance of sync pulses, and investigate any stimulation artifact leakage. With everything set up properly as we recommend, EEG recordings should look clean or with a minimal amount of stimulation artifact or line-noise during both stimulation and no-stimulation. An example is shown in Figure 3.8 and a troubleshooting procedure is shown in Appendix A.

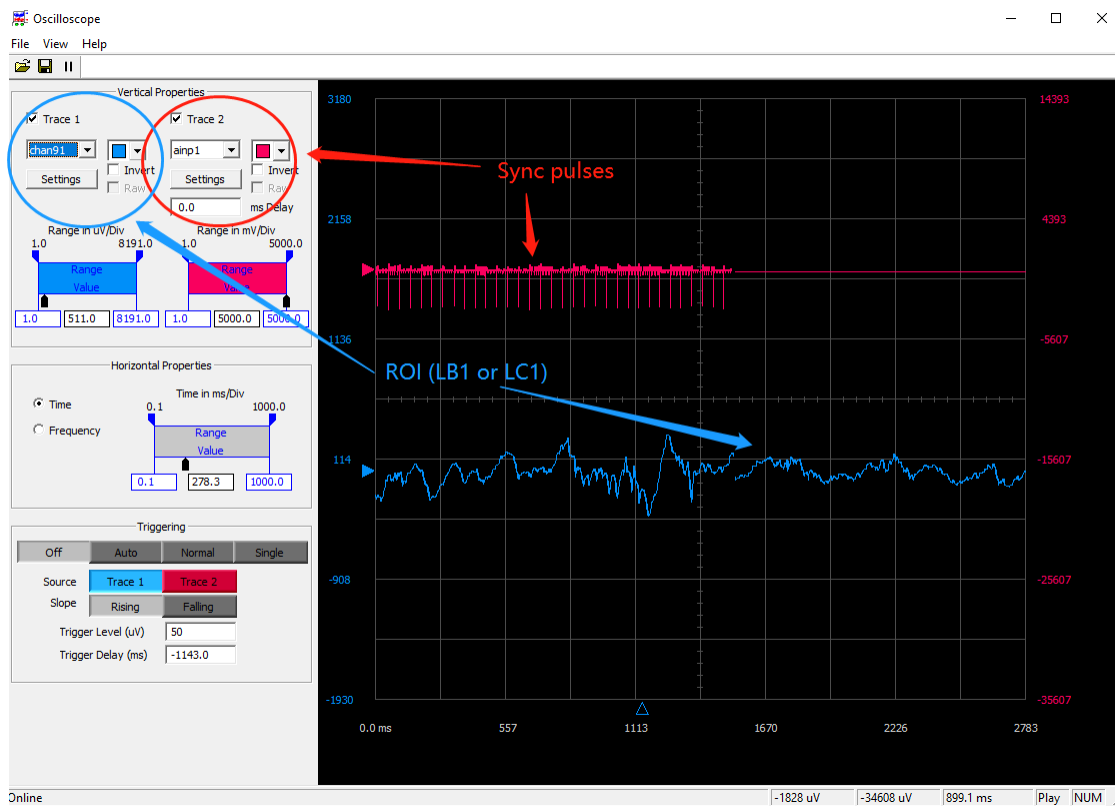


Figure 3.8: Monitoring BN stimulation and EEG recordings.

CHAPTER 4

A BRAIN-COMPUTER INTERFACE FOR MODULATING HIPPOCAMPAL GAMMA OSCILLATIONS VIA FREE-RECALL STIMULATION

4.1. Introduction

The past two decades have seen considerable interest in the development of deep brain stimulation (DBS) for restoring brain dysfunction. Nascent therapies for memory restoration draw on previous efforts in neuromodulation targeting Parkinson’s disease (Deuschl, Schade-Brittinger, et al., 2006; De Hemptinne et al., 2015), epilepsy (B. C. Lega, Halpern, et al., 2010), and depression (Mayberg et al., 2005; C. Zhou et al., 2018). However, as discussed earlier in Chapter 3, these DBS therapies are mostly open-loop with manually selected stimulation parameters via a trial-and-error procedure. The preferred stimulation was selected target via anatomical and empirical evidence (e.g. the subthalamic nucleus for neuromotor disorders and the medial temporal lobe for memory conditions)(Deuschl, Schade-Brittinger, et al., 2006). Open-loop DBS is inadequate for capturing the underlying neural dynamics during cognitive processes and has failed to restore memory function, and some have been shown to impair memory performance (Mankin and Fried, 2020; Natu et al., 2019; Jacobs, J. Miller, et al., 2016; Suthana et al., 2012; Laxton, Tang-Wai, et al., 2010). Recent studies have shown promising results of closed-loop stimulation paradigms, where stimulation parameters are guided by neural feedback (Ezzyat et al., 2018; Ngo et al., 2013). For instance, Miranda et al. used classifiers to predict episodic memory encoding success, they applied stimulation for approximately 700 *ms* if the classifier predicted an encoding failure. This strategy gave a 15 % increase in memory performance on average across 40 participants (Miranda et al., 2015). In contrast, Shanechi describes an alternative closed-loop,

control-theoretical method for treating depression (Shanechi, 2019). Their method incorporates an oscillatory signal acting as a ‘biomarker’ of mood, namely orbitofrontal theta or alpha power. This biomarker is used as a signal amenable to control using state space modeling and an LQR servo-controller. Then, Yang, Connolly, et al. developed a testbed system for implementing this method, using a Kalman filter to estimate the biomarker signal and an LQR controller to manipulate it precisely (Yang, Connolly, et al., 2018).

There are several concerns regarding the implementation of classifier-based closed loop BCI devices. First, the classifier performance is subject-specific based on numerous neural recordings and experimental sessions. Second, the regression model for predicting behavioral outcomes (encoding success) requires extensive data across more than 100 contacts, which may not be accessible in a clinically-applicable system. More importantly, the triggered DBS still needs a priori knowledge of stimulation parameters (i.e. stimulation amplitude, frequency, duration, etc.), which is not vastly available for treating memory conditions (Jacobs, J. Miller, et al., 2016), making it an on-demand open-loop stimulation scheme. Therefore, we seek to apply control-theoretical principles, which incorporate neural temporal dynamics, in neuromodulation for memory disorders. First, we use hippocampal gamma oscillatory power as an effective biomarker for memory since studies in both animals and humans have suggested that changes in gamma oscillatory power predict memory success and it is a critical component in local and cross-regional coupling via phase synchrony and cross frequency coupling (Sederberg, Schulze-Bonhage, et al., 2007; Solomon et al., 2017). Second, we believe posterior cingulate cortex (PCC) represents a rational choice for a stimulation target because not only does PCC exhibit dense connectivity to a variety of brain regions and has critical roles in the brain default mode network (i.e. a network of active interacting brain regions, Bai et al., 2009; Khalsa et al., 2014). Previous work has demonstrated that stimulation of the PCC reliably elicits hippocampal gamma oscillatory activity during episodic memory (Natu et al., 2019). These data were collected using the free-recall stimulation paradigm

(see Chapter 3), allowing us to model hippocampal gamma oscillatory power in the presence and absence of stimulation during encoding.

We demonstrate the feasibility of a control-theoretical BCI system for modulating hippocampal gamma oscillatory power predicated on PCC-applied stimulation using linear system identification methods similar to those reported previously (Yang, Connolly, et al., 2018). We show that we are able to model the relationship between PCC stimulation and responsive hippocampal gamma power using our ARX framework, accurately representing gamma power time-series in both stimulation and non-stimulation conditions. Next, we show that a system using PCC stimulation to modulate hippocampal gamma power is controllable in 100% of subjects as measured by computing the rank of the controllability matrix (Kailath, 1998). We then describe a simulation framework for the PCC–hippocampal system constructed using Simulink.

4.2. Materials and Methods

4.2.1. Participants and Experimental Stimulation

Eighteen participants (ages 20-60, 9 female) with medication-resistant epilepsy who underwent stereo-electroencephalography surgery with the goal of identifying their ictal onset region(s) participated in the study. Participants came from the UT Southwestern epilepsy surgery program across a span of 4 years. Only patients who had intracranial electrodes placed within the posterior cingulate were included in the study. The demographic information of participants is summarized in Table 5.1. The research protocol was approved by the UT Southwestern Medical Center Institutional Review Board, and each participant gave informed consent prior to data collection. Following implantation, electrode localization was achieved by co-registration of the post-operative computer tomography scans with pre-operative magnetic resonance images. The co-registered images were evaluated by a

member of the neuroradiology team to determine the final electrode locations (Details of implantation are found in Section 3.2). Each subject participated in a verbal free-recall

Table 4.1: Demographic information of participants in Free-recall stimulation paradigm. MTL: Medial temporal lobe, NTL: Neocortical temporal lobe, LH/RH: left/right hemisphere, B: bilateral.

Subject No.	Age	Type of epilepsy	Hemisphere	Duration of epilepsy
1	32	Right NTL	RH	25
2	29	Right NTL	RH	3
3	40	Left MTL	LH	9
4	24	Multifocal	B	6
5	43	Left MTL	LH	20
6	40	Bilateral B epilepsy	B	5
7	21	Right NTL	RH	9
8	40	Bilateral MTL	B	7
9	20	Multifocal	B	3
10	38	Multifocal	B	14
11	51	Right MTL	RH	43
12	22	Right NTL	RH	8
13	37	Bilateral NTL	B	15
14	43	Left NTL	LH	19
15	34	Left MTL	LH	24
16	33	Left NTL	LH	4
17	31	Left NTL	LH	6
18	60	Left NTL	LH	9

task. During the encoding phase, stimulation was applied to the PCC with an amplitude of 2 *mA* and a frequency of 100 *Hz* during every other encoding list, and was synchronized with the onset of the first word in the list. These stimulation parameters were determined using accepted safety thresholds for DBS drawn from initial work (Butson et al., 2007) and by incorporating typical parameters used for DBS techniques (Suthana et al., 2012; Jacobs, J. Miller, et al., 2016). This free-recall stimulation paradigm is illustrated in Figure 3.3 and detailed explanations of the paradigm and safety considerations are found in Section 3.3. All

of the 18 participants had their stimulation sites in the left PCC. For this study, we used the first word presented from each list. Since these words were preceded by the 50-second post-encoding delay and recall tasks, during which there was no stimulation, the stimulus amplitude took the form of a step function going from zero to 2 mA at the onset of the presentation of the first word (encoding event). Each subject exhibited a total of 10 such encoding events. We chose to focus on these events since it allowed us to compare gamma power level over a 2 second period prior to stimulation onset with gamma power during a 2 second interval after the onset of stimulation. This eliminated the effects of changes in baseline gamma over longer periods of time that can result from nonstationarity in the iEEG.

4.2.2. Data Acquisition and Processing

Intracranial electroencephalogram (iEEG) signals via depth electrodes, where contacts spaced 5-10 mm apart, were recorded using a Nihon-Kohden Nuerofax clinical EEG system under a bipolar montage with the most medial white matter contact on individual electrodes as the reference (for hippocampal recordings, this was white matter in the adjacent subcortical temporal lobe). The iEEG recordings are monitored continuously and we collected the signals during the free-recall stimulation paradigm. For each subject, iEEG signals were segmented according to the sync pulse train and the 4 transition interval from no-stimulation (2 seconds before stimulus onset) to stimulation (2 seconds after stimulus onset) was selected for each encoding list. There were 10 transition trials for each subject. Channels with highly noisy signals were excluded prior to re-referencing. A bipolar referencing scheme (within the contact probe, e.g. LB1-LB2, LB2-LB3, ..., LB10-LB1) was utilized to limit the stimulation artifact from affected electrodes. Then, iEEG trails were downsampled to 500 *Hz* and notch filtered at 60Hz for line noise removal via a projection-based filter (Davila, 2015). Further, stimulation artifact at 100 *Hz* was removed by utilizing a linear phase FIR bandstop filter

of $98 - 102$ Hz. Data from one subject was rejected due to its extensive noise, leaving a total of 17 subjects.

We sought to directly model hippocampal gamma power because modeling the full spectrum of iEEG would have necessitated arriving at a model that generates gamma power with the same statistical properties as our experimentally measured gamma power, and would have presented a more challenging modeling problem. Thus, instantaneous gamma power was extracted from the iEEG trials using an analytic wavelet filter bank consisting of Morse wavelets with symmetry parameter equal to 3 and time-bandwidth product equal to 60 (Lilly and Olhede, 2012). Ten Morse wavelets were used for covering gamma sub-bands of 30-50 Hz, 50-70Hz, and 70-90 Hz. Estimates of instantaneous RMS gamma power were obtained by taking the square root of the sum of the squared magnitudes of the wavelet filter outputs. Analytic wavelet filters were found to have greater sensitivity in detecting short-duration gamma oscillations compared to using a bandpass filter followed by conversion to analytic signal via the Hilbert transform.

4.2.3. Linear ARX Model

For modeling the hippocampal gamma power, we chose an autoregressive with exogenous input (ARX) model due to realistic representation of the neural activity during stimulation paradigm. Unlike an AR model, the ARX model incorporates an external input, which represents the stimulation applied to the PCC. Also, the exogenous term can integrate the DC level of intrinsic gamma power when stimulation is absent. Further, the ARX model output can have closely matched power spectral density (PSD) as observed experimental RMS gamma power, and it is simple and computationally efficient for the subsequent controller design. A linear ARX model can be written as

$$x(t) = -\sum_{k=1}^p a_k x(t-k) + b_{DC} u_{DC} + b_s u_s(t) + w(t) \quad (4.1)$$

where $x(t)$ represents the instantaneous RMS gamma power in μV at discrete-time t . The exogenous input u_{DC} is a constant that determines the mean value of the RMS gamma power when the stimulus current $u_s(t) = 0$. Both u_{DC} and $u_s(t)$ are currents having units of mA. This choice of units for the input is justified since the power in a periodic signal is proportional to its amplitude. For instance, the RMS power of a sinusoidal signal $A_c \cos(\omega_c t + \theta)$ is $A_c/\sqrt{2}$, which is independent of the frequency ω_c and phase θ . The result holds for any periodic signal (Oppenheim, Hamid, et al., 1997). Therefore, using the stimulus amplitude (current) as $u_s(t)$ proportionally affects the RMS gamma power $x(t)$. This is adjusted by the coefficient b_s . Further, $w(t)$, in this case, is a zero-mean Gaussian white noise process with variance σ_w^2 and units of μV , representing the system (neural) randomness in the hippocampal RMS gamma power. The ARX model parameters associated with the past output, $a_k, k = 1, \dots, p$ are dimensionless, where p denotes the model order. Parameters b_{DC} and b_s have units of resistance ($m\Omega$), representing how much of an impact stimulation amplitude and the DC level contribute to RMS gamma power. Here, the DC level, in absence of stimulation can be an arbitrary value since the coefficient u_{DC} scales the level accordingly, so we chose $u_{DC} = 1$ mA. All of these model coefficients can be identified using the experimental iEEG data during open-loop FR stimulation. Given the model parameters, the mean RMS gamma power across time can be computed theoretically via the Final Value Theorem (Oppenheim and Shafer, 1989). The result is,

$$\lim_{t \rightarrow \infty} x(t) = \frac{b_{DC}u_{DC} + b_s u_s}{1 + \sum_{k=1}^p a_k} \equiv \hat{\gamma} \quad (4.2)$$

Here, the random term $w(t)$ is ignored because it has zero mean. This can be used to predict the mean RMS power for any fixed amplitude stimulus current with amplitude u_s . In our

model, u_s was the step function

$$u_s(t) = \begin{cases} 0, & t = -2, \dots, -0.002 \\ 2, & t = 0, \dots, 2 \end{cases} \quad (4.3)$$

where t is the time in seconds of the encoding event. The stimulation started at $t = 0s$. Hence, using the step function 4.3 in Equation 4.2, the mean RMS gamma power for trials during no-stimulation and stimulation are

$$\hat{\gamma}_{ns} \equiv \frac{b_{DC}}{1 + \sum_{k=1}^p a_k} \quad (4.4)$$

and

$$\hat{\gamma}_s \equiv \frac{b_{DC} + 2b_s}{1 + \sum_{k=1}^p a_k} \quad (4.5)$$

respectively. Using the established relationships between the power spectral density (PSD) of the input and output of a linear time-invariant system, the PSD of such an ARX model can be written as (Kay, 1988):

$$P_{xx}(f) = \frac{\sigma_w^2 + 4b_s^2/(2\pi f/F_s)^2}{|1 + \sum_{k=1}^p a_k e^{-j2\pi f k/F_s}|^2} \quad (4.6)$$

where f is continuous-time frequency and F_s is the sampling frequency. We chose to use this expression to compare the theoretical PSD of the model with the estimated PSD of experimentally measured instantaneous gamma power.

As mentioned, the ARX model coefficients can be identified using our open-loop FR stimulation I/O data (experimental RMS gamma power $x(t)$ as the output and the step function 4.3 as the system input) via least squares linear prediction, which minimizes the squared error (Ljung, 1999)

$$\epsilon_{pred} = \sum_{t=p+1}^N e(t)^2 \quad (4.7)$$

over the ARX model parameters, $a_k, k = 1, \dots, p$, b_{DC} , and b_s , where the prediction errors are given by

$$e(t) = x(t) - \sum_{k=1}^p a_k x(t-k) - b_{DC} u_{DC} - b_s u_s(t) \quad (4.8)$$

with $t = p+1, \dots, N$ (discrete-time). In matrix notation, (4.8) represents an overdetermined system of equations,

$$Cv \approx d \quad (4.9)$$

with

$$C = \begin{bmatrix} x(p) & \cdots & x(1) & u_{DC} & u_s(1) \\ x(p+1) & \cdots & x(2) & u_{DC} & u_s(2) \\ \vdots & \ddots & \vdots & \vdots & \vdots \\ x(N-1) & \cdots & x(N-p) & u_{DC} & u_s(N-p) \end{bmatrix} \quad (4.10)$$

$d = [x(p+1), x(p+2), \dots, x(N)]^T$ and the ARX parameter vector $v = [a_1, a_2, \dots, a_p, b_{DC}, b_s]^T$.

It is well known that these least squares equations have a unique solution provided that the matrix C has full column rank (Golub and Van Loan, 1996). Hence, the two right-most columns of C must be linearly independent. Since u_{DC} is constant and $u_s(t)$ is a step function, this condition is true. For our model, we clarify that it is not necessary for the inputs to have a large bandwidth in order to identify the model parameters because the ARX model is driven by white noise $w(t)$, rather than the input pattern (Ljung, 1999). The least squares solution to equation (4.9) is $v^* = (C^T C)^{-1} C^T d$, whereas a QR decomposition of C is used more often in practice for its efficiency and accuracy (Golub and Van Loan, 1996). In order to evaluate our model accuracy, we utilized the commonly used minimum mean-squared prediction error as our quality metric, which can be estimated by (Ljung, 1999):

$$\epsilon_{pred}^* = \frac{1}{N} \|Cv^* - d\|^2 \quad (4.11)$$

where Cv^* is the optimal least squares prediction of the values in d . A normalized measure which takes into account the variance of $x(t)$ is the “fit percentage”, given by

$$\text{FitPerc} = 100 \left(1 - \frac{\sqrt{\epsilon_{pred}^*}}{\|d - \mu_d\|} \right) \quad (4.12)$$

where μ_d is the sample mean of the data vector d (Ljung, 2020). Note that a low mean squared prediction error leads to a fit percentage close to 100%. In Section 4.3.2 we demonstrate that the linear prediction approach to identifying the parameters of our ARX model gives good results.

4.2.4. LQI Servo-Controller

To achieve a robust and precise control of hippocampal gamma power, we were faced with two major objectives: the gamma power needs to reach the predetermined target power level rapidly while the control mechanism maintains a minimal amount of stimulus energy delivered to the patient. These conflicting aims lend themselves to employing a linear quadratic integral (LQI) controller, which is an optimal control strategy (Halevi, 1994). Hence, our design of the closed-loop simulation framework consists of the ARX plant model that generates gamma power and an LQI controller that attempts to drive measured gamma power towards a designated setpoint. The illustration of our framework is shown in Figure 4.1, where the I/O of our ARX model represents the physiological PCC-applied stimulation and hippocampal gamma oscillatory activity. The cost function for the LQI controller is given by:

$$J = \sum_{t=0}^{\infty} z_t^T Q z_t + R u_s(t)^2 \quad (4.13)$$

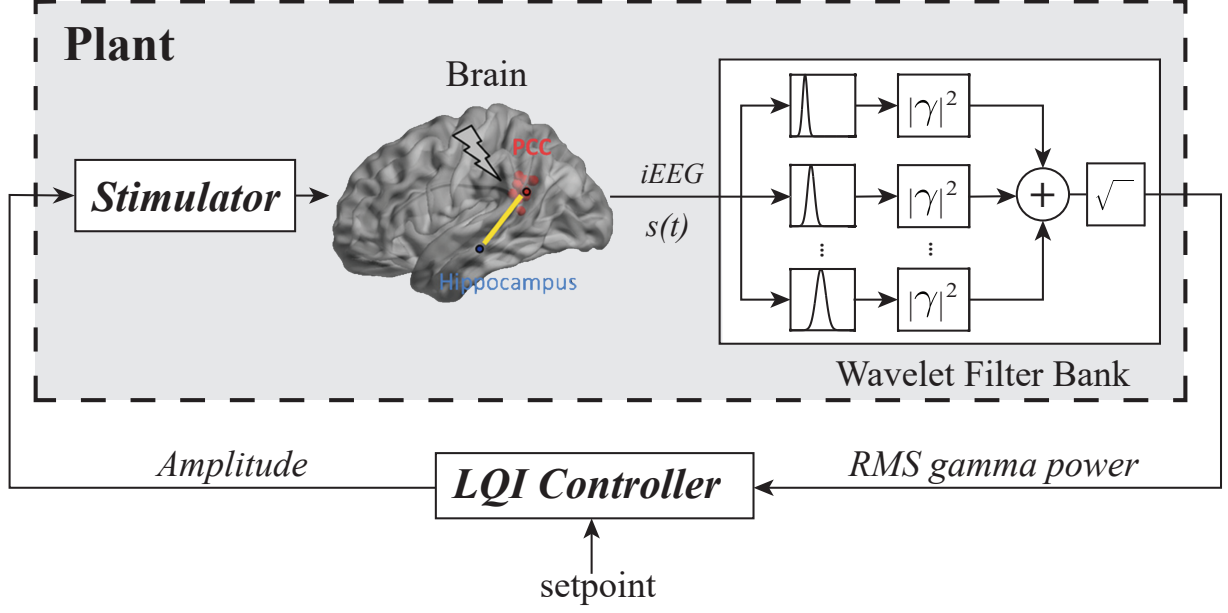


Figure 4.1: Simulation framework for control of RMS gamma power.

where $z_t = \begin{bmatrix} x_t^T & e_i(t) \end{bmatrix}^T$, and

$$e_i(t) = T_s \sum_{k=0}^t r - y(t) \quad (4.14)$$

is the discrete-time integration of the difference between the setpoint r and the observed gamma power $y(t)$. The parameter Q defines the weights on the states, adjusting the rate at which gamma power approaches the setpoint, while the parameter R weights the input and determines the amount of stimulus energy delivered to the patient via the stimulus amplitude $u_s(t)$. This optimal control problem has a well-known solution, the cost function in (4.13) is minimized using the control law $u_s(t) = -Kz_t$, where K is the solution to an algebraic Ricatti equation that depends on the state-space model A, B, C, D, G , details are found in (Rami and X. Y. Zhou, 2000). The controller takes the buffered plant output as the state vector x_t , which after augmenting with the integrated setpoint error $e_i(t)$, is multiplied by the gain vector $-K$ to determine the stimulation current amplitude. The resulting LQI

servo-controller is shown in Figure 4.2. In practice, the optimal set point can be modified based on subject-specific empirical observations. For safety concerns, we assigned an upper limit of 9 mA for the stimulation aptitude to maintain our DBS charge level below 30 μC per cm^2 (MacDonald, 2002; R. J. Coffey, 2009).

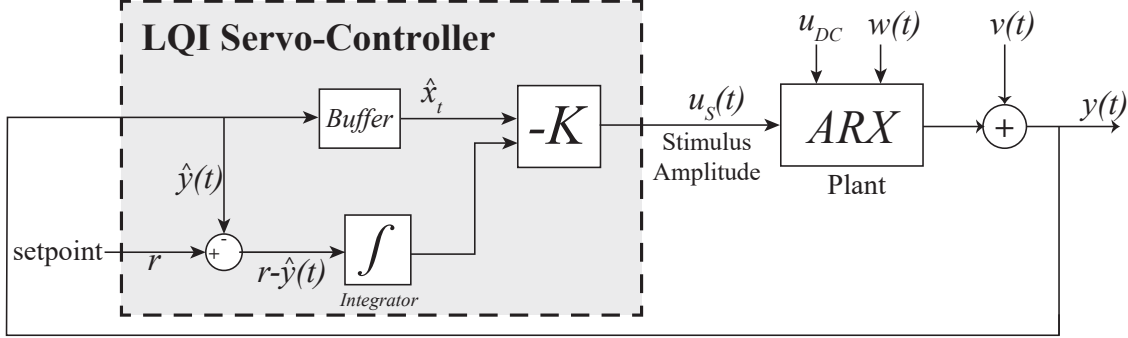


Figure 4.2: Linear quadratic integral servo-controller.

As the gain vector K is associated with the state-space vector, we then converted our ARX plant model into state-space form:

$$\begin{aligned} x_{t+1} &= Ax_t + Bu_t + Gw(t) \\ y_t &= Cx_t + Du_t + v(t) \end{aligned} \tag{4.15}$$

where x_t is the system state vector at discrete-time t , $u_t = \begin{bmatrix} u_{DC} & u_s \end{bmatrix}^T$ and y_t are scalar input and measurements, respectively, and $w(t)$, and $v(t)$ are the system disturbance and observed noise signals, respectively. The dimensions of these vectors, as well as that of matrices A, B, C, D , and G , depend on the state-space model. The ARX model can be readily implemented using a state-space model (Chang et al., 2012). In our case, the state vector consists of p consecutive samples of the RMS gamma power signal, $x_t =$

$\begin{bmatrix} x(t) & x(t-1) & \cdots & x(t-p+1) \end{bmatrix}^T$. Both the observation $y(t) = x(t)$ and the system disturbance $w(t)$ are scalar quantities. The observation noise $v(t)$ accounts for measurement noise and modeling uncertainties. Correspondingly, in order for (4.15) to agree with (4.1), we must have:

$$A = \begin{bmatrix} -a_1 & -a_2 & \cdots & -a_p \\ 1 & 0 & \cdots & 0 \\ 0 & 1 & \cdots & 0 \\ \vdots & \vdots & \ddots & \vdots \\ 0 & 0 & \cdots & 1 \end{bmatrix} \quad B = \begin{bmatrix} b_{DC} & b_s \\ 0 & 0 \\ \vdots & \vdots \\ 0 & 0 \end{bmatrix} \quad (4.16)$$

$G = \begin{bmatrix} 1 & 0 & \cdots & 0 \end{bmatrix}^T$, $C = \begin{bmatrix} 1 & 0 & \cdots & 0 \end{bmatrix}$, and $D = 0$. The choice of an ARX model has an important advantage compared to a general linear state-space model (LSSM). Since the state vector consists of consecutive samples of the RMS gamma power, there is no need to estimate the state vector using a Kalman filter. Moreover the use of scalars for b_{DC} and b_s rather than FIR filters, readily permits this simple transformation to state space form.

4.3. Results

4.3.1. Stimulation Effects on Hippocampal Gamma Power

For each of the 17 subjects, we investigated instantaneous RMS gamma power trails in a 4-second time window such that $x_k(t)$ where $t = -2, \dots, 0, \dots, 2$ s are time samples corresponding to a sampling rate of 500 *samples/s*, and $k = 1, \dots, 10$ represents the k-th trail. The stimulation was applied at $t = 0$ s. Example traces of the stimulation amplitude $u_s(t)$ and the instantaneous RMS gamma trials are shown in Figure 4.3, along with the ensemble average \bar{x} across all ten trials. We found robust hippocampal gamma power increases in response to the PCC-applied stimulation in all individual trials as well as in the ensemble average, especially within the first second after the stimulation. We then conducted a detailed examination of this power increase in the hippocampal gamma band by segmenting trails according to the stimulation conditions: a 2-second interval prior stimulation onset (i.e. gamma power during no stimulation, $t = -2, \dots, 0$ s) and another 2-second interval after stimulation onset (i.e. gamma power during stimulation, $t = 0, \dots, 2$ s). We chose the time interval of 2 second because it is well known that neural activity is non-stationary and EEG series (as well as the power) can be considered as a stationary process within a short duration (Blanco et al., 1995). Besides, the encoding event lasts a little over 2 seconds (because of the random jitter interval) and we wanted to eliminate additional behavioral (memory encoding from another event) effects on the gamma power. This also reduced the possibility that long-term baseline drift in mean RMS gamma power levels affected our results. In order to incorporate temporal-relevant power changes, we first compared the instantaneous power during stimulation versus no-stimulation and tested the amount of trials (in percentage) that the gamma power were significant greater during stimulation via one-tailed paired t-test for each of 10 trials ($p < 0.05$). On average, $57.61 \pm 20.47\%$ of the trials across 17 subjects exhibited significant power increases in the hippocampus gamma band due to the

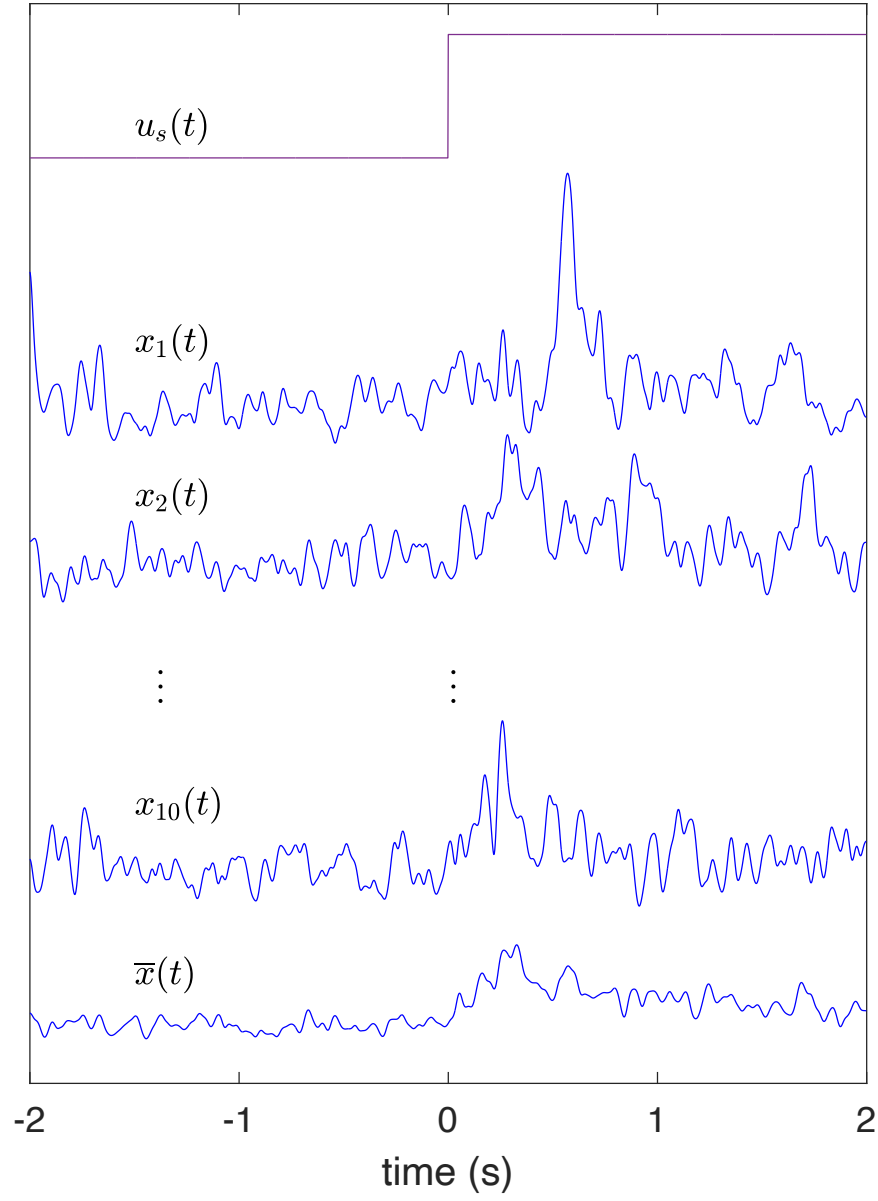
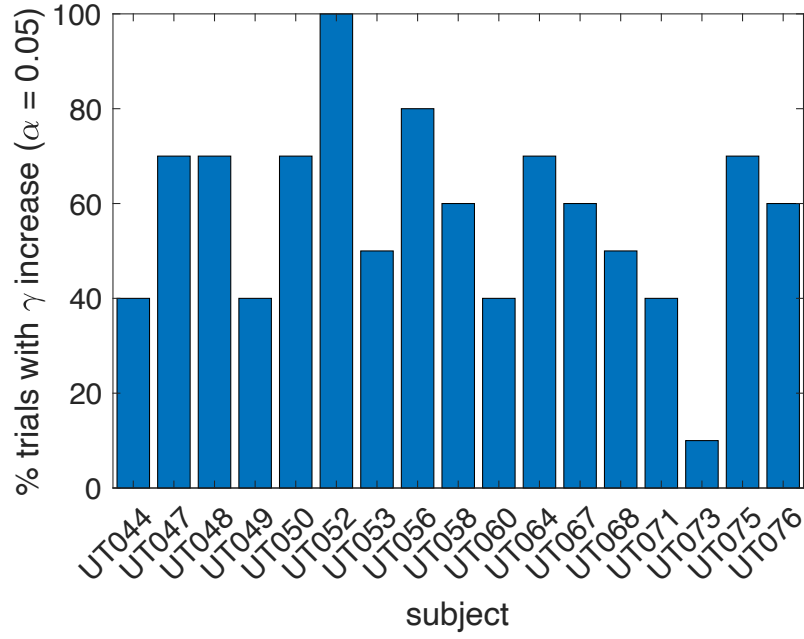
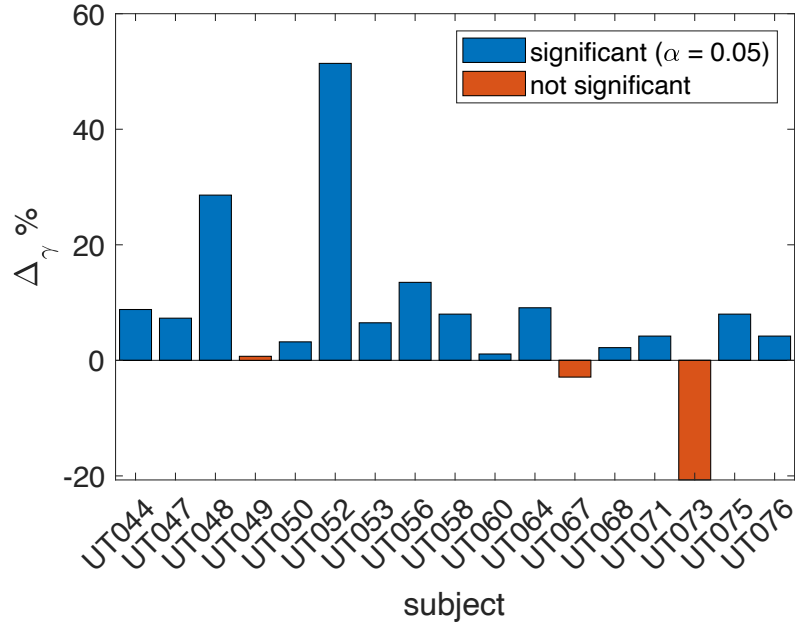


Figure 4.3: Instantaneous RMS gamma power trials, $x_1(t), \dots, x_{10}(t)$ and their ensemble average $\bar{x}(t)$. The stimulation signal amplitude $u_s(t)$ is a 2 mA step function.



(a) Percentage of trials with statistically significant increase in mean gamma power during stimulation.



(b) Increase in mean RMS gamma power Δ_γ % during stimulation, derived from ensemble average.

Figure 4.4: Impact of stimulation on mean gamma power.

stimulation. Results for each individual subjects are shown in Figure 4.4. We then computed mean RMS gamma power across time for trials during both stimulation (denoted as \bar{x}_s) and no-stimulation (denoted as \bar{x}_{ns}) to show an average power increase (across time). This was done by normalizing the difference in mean RMS gamma power between two conditions such that

$$\Delta_\gamma\% = \frac{\bar{x}_s - \bar{x}_{ns}}{\bar{x}_{ns}} \times 100\%$$

This normalized increase in mean RMS gamma power levels is found in Figure 4.4b. We found that 15 out of 17 subjects exhibited greater gamma power during stimulation than during no-stimulation, and 14 out of these 15 subjects showed their power increases were significant using a one-tailed pair t-test ($p < 0.05$).

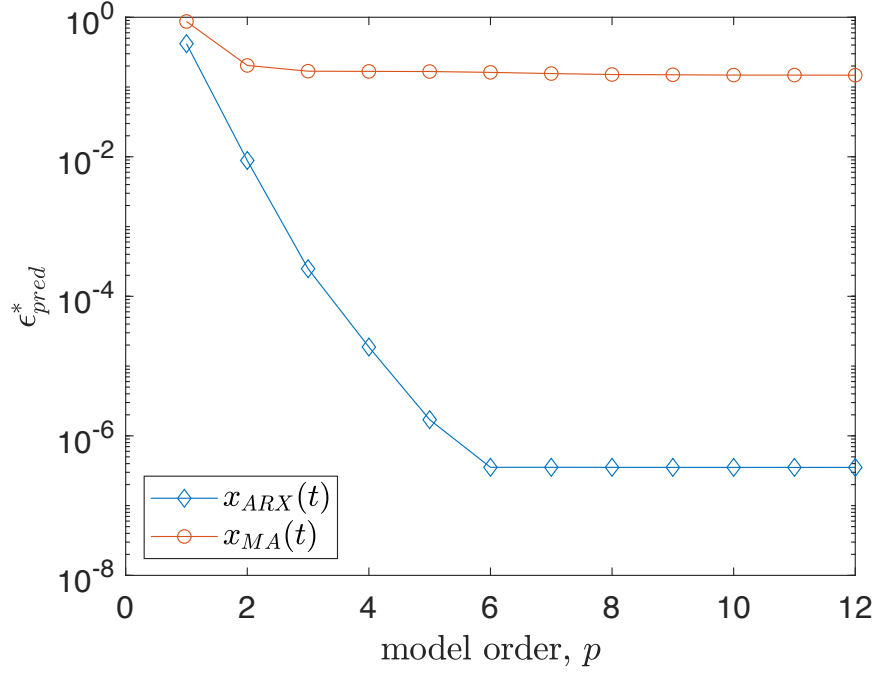
4.3.2. Model Validation and Performance

When estimating the ARX model parameters, we followed the linear least squares prediction solutions as described in Section 4.2.3 using the ‘arx’ function in the MATLAB System Identification Toolbox (<https://www.mathworks.com/products/sysid.html>). The function returns a number of model quality metrics, among them are the mean squared prediction error (ϵ_{pred}^*) and the goodness of fit (FitPerc) given by (4.11) and (4.12), respectively. Note that least square solutions for the system output $\hat{x}(t)$ were based on the past observed output $x(t-1), \dots, x(t-p)$ so that the function returned prediction MSE and the model FitPerc were equivalent to that of one-step-ahead prediction. In order to assess these quality metrics, we conducted a simulation where an ARX process and a moving average (MA) process were created. For the ARX random process, we used parameters identified from one of the subjects (via an ARX model) such that: $a_1 = 5.6758$, $a_2 = -13.6152$, $a_3 = 17.6747$, $a_4 = -13.0990$, $a_5 = 5.2554$, $a_6 = -0.8917$, $b_{DC} = 3.4689 \times 10^{-4}$, $b_s = 8.7828 \times 10^{-5}$. The process had a input of $u_s(t)$ and was driven by a zero-mean Gaussian white noise sequence $w(t)$ with a variance of 3.7197×10^{-7} . Then, we computed the ARX model of a high-order

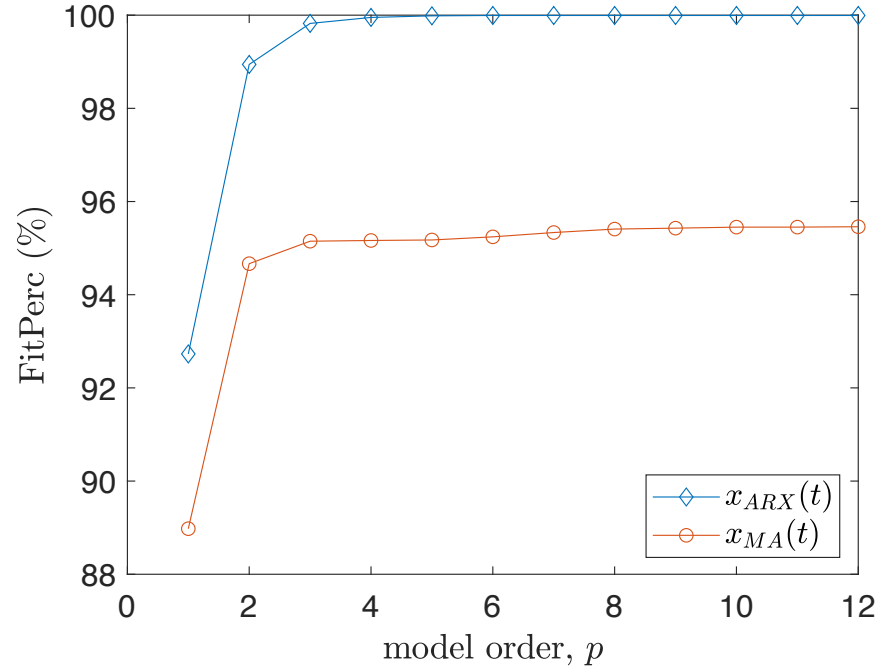
MA process given by

$$x_{MA}(t) = \sum_{k=0}^{29} b_k w(t - k\Delta_t) + b_{DC} u_{DC}(t) + b_s u_s(t) \quad (4.17)$$

where $w(t)$ is the same zero-mean Gaussian process used to produce $x_{ARX}(t)$. The b_k coefficients corresponded to a lowpass FIR filter so that the PSD of $x_{MA}(t)$ closely matched that of $x_{ARX}(t)$. The b_{DC} and b_s coefficients were chosen to yield the same DC values over the no-stim and stim intervals as $x_{ARX}(t)$. For both random processes, we ran through model orders ranging from $p = 1, \dots, 12$, and computed ϵ_{pred}^* and FitPerc, accordingly. We found that the mean squared prediction error drops rapidly with increasing model order for the ARX process, and then levels off at the correct model order. Similarly the fit percentage rises rapidly as the model order is increased and then levels off at nearly 100% after the correct model order of $p = 6$. For the MA process, the quality metrics deteriorated compared to those for the ARX process, with no improvement in either of the quality metrics beyond an ARX model order of $p = 3$. This suggests that our approach to estimating ARX model parameters is accurate when the model being identified corresponds to an ARX model. Attempting to identify ARX parameters of a signal that does not correspond to an ARX model (such as an MA model) will have a negative impact on model quality metrics (see Figure 4.5). More importantly, we demonstrated the high-valued quality metrics were not due to over-fitting via a 10-fold cross validation, by computing an ARX model based on 9 of 10 trials and testing the prediction $\hat{x}(t)$ of the 10th trial. We found there was virtually no change in the model quality metrics. Given these results of model validation, we believe that the ARX model is adequate for instantaneous RMS gamma power. We fitted the ARX model for each of the 15 subjects who experienced RMS gamma power increases on a trial-by-trial basis then averaged model parameters across trials to form a subject-specific composite ARX model.



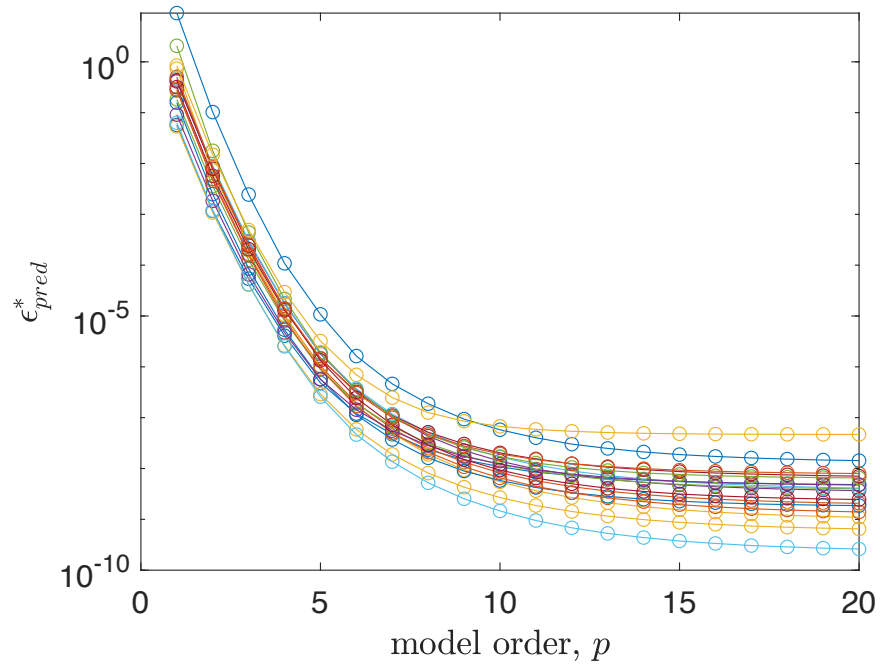
(a) Mean squared prediction error.



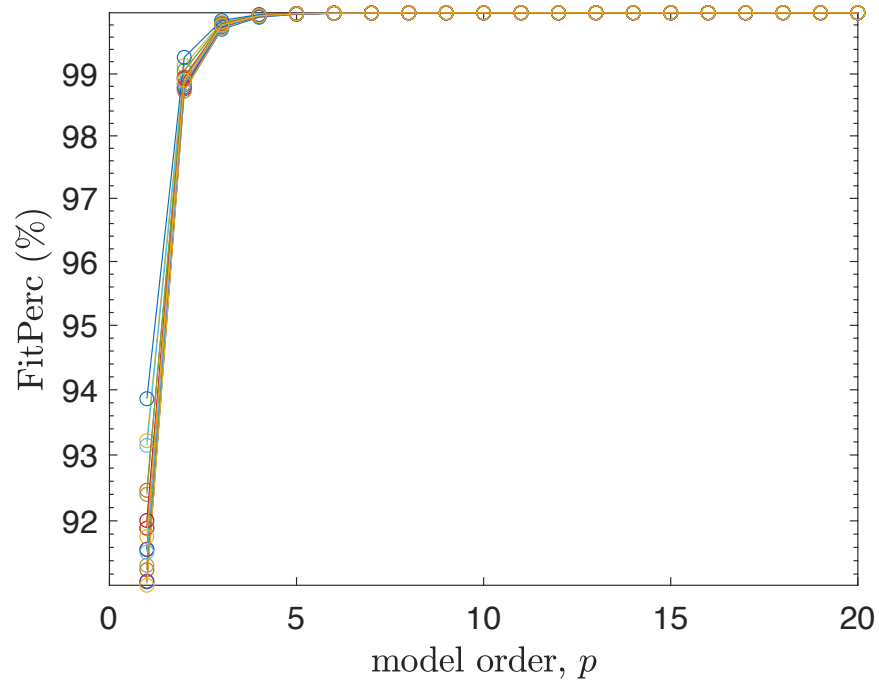
(b) Fit Percentage.

Figure 4.5: Model quality metrics for identifying the ARX parameters for two different signals: an ARX process of order 6, $x_{ARX}(t)$, and a moving average (MA) process of order 29, $x_{MA}(t)$ having similar spectral features.

We investigated the model performance ϵ_{pred}^* and FitPerc for model order $p = 1, \dots, 20$, independently, and concluded that $p = 6$ offered a reasonable trade-off between mean-squared prediction error, fit percentage, and computational complexity. We implemented a model order of $p = 6$ and found all but one subject exhibited mean-squared prediction error values lower than 10^{-6} , while fit percentage approached 99% (as shown in Figure 4.6). We then compared the predicted RMS gamma power versus the experimental data. Here, RMS gamma power trials were predicted and segmented according to the stimulation conditions (as discussed in Section 4.3.1) for which mean RMS gamma power was computed. We found that the predicted mean RMS gamma power during both stimulation and no-stimulation closely matched the experimental (open-loop) results. We present this comparison in a regression shown in Figure 4.7. As another objective, we sought to demonstrate that our model maintains the spectral characteristic of the hippocampal gamma power. Thus, we computed power spectral density (PSD) for each of the 10 trials via using periodogram with a 2000-sample Hanning window then compared this averaged PSD (across trials) with the theoretical PSD for the identified ARX model (see Equation 4.6). Example traces of PSD comparison from two subjects are shown in Figure 4.8. We confirm there is a fairly close match between the periodogram estimate of instantaneous RMS gamma power PSD and the theoretical PSD for the ARX model, especially for the 0-100 Hz frequencies. Also, we note that the frequencies represented in the PSD correspond to random variability in instantaneous RMS gamma power, rather than gamma oscillations in iEEG. This result suggest that an ARX model with model order $p = 6$ is capable of not only predicting hippocampal gamma power but also maintaining critical spectral features in predicted signals.



(a) Mean squared prediction error.



(b) Fit percentage

Figure 4.6: Model quality metrics for all subjects.

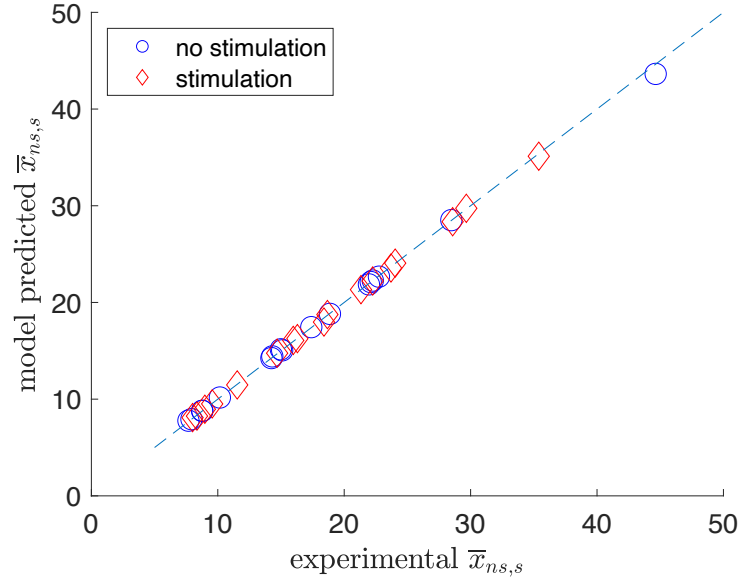


Figure 4.7: Mean RMS gamma power level predictions by ARX model.

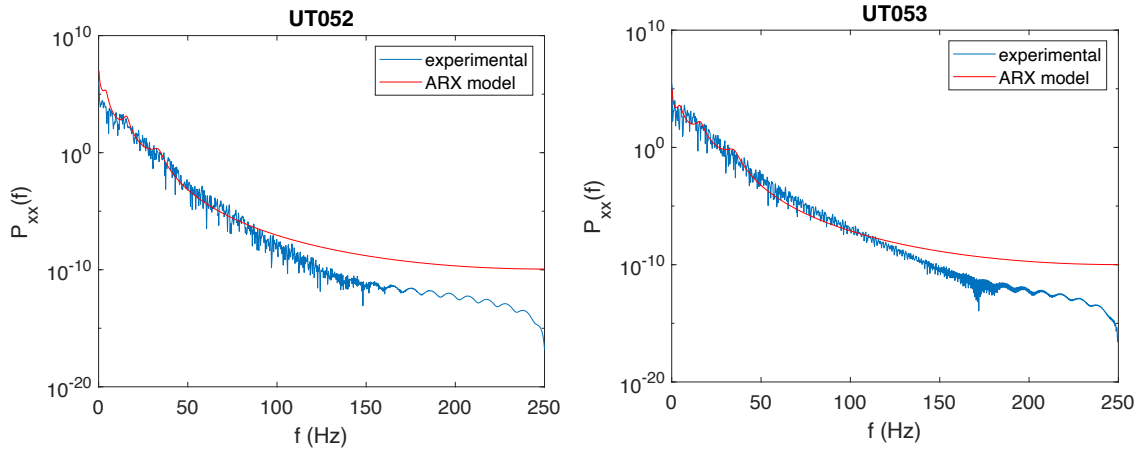


Figure 4.8: Comparison of averaged periodogram of instantaneous RMS gamma power (experimental) with theoretical power spectral density of identified ARX models, as given by (4.6) with $p = 6$.

4.3.3. Simulated Closed-Loop Control

To test our strategy of modulating hippocampal gamma power, we implemented a closed-loop LQI servo-controller in Simulink using a sampling interval of 2 ms and a simulation duration of 4 seconds ranging from $t = -2 \text{ s}, \dots, 0, \dots, 2 \text{ s}$ (where stimulation was applied at $t = 0 \text{ s}$), for each of the subjects who experienced gamma increase due to open-loop stimulation. For tuning the controller weights in the cost function (4.13), We utilized typical parameters such that:

$$Q = \begin{bmatrix} 0.005I_6 & \bar{0}_6 \\ \bar{0}_6^T & 100 \end{bmatrix}, \quad R = 1 \quad (4.18)$$

where I_6 is the 6×6 identity matrix and $\bar{0}_6$ is a 6×1 zero vector. The closed-loop control was applied at $t = 0 \text{ s}$. For each subject, the parameters (state-space vectors) for the LQI controller were derived from the identified composite ARX model (averaged across all ten trials). The setpoint (desired target level) of closed-loop control was determined by using the maximum achievable RMS gamma power via the LQI controller while stimulation amplitudes were maintained under 9 mA, which is the upper safety limit of stimulation current for intracranial sEEG electrodes. We were able to control the RMS gamma power and achieve the setpoint within 300 ms in all 15 subjects, although the setpoint level varied from subject to subject. Figure 4.9 shows the mean and standard deviation of RMS gamma power over 100 independent trials for two subjects. We then computed the normalized RMS power increases (as in Equation 4.3.1) for both closed-loop (during closed-loop stimulation versus during no stimulation) and open-loop configurations (experimental stimulation versus during no stimulation) for the 15 subject, and we found all of these subjects exhibited greater power increases via our closed-loop LQI controller (see Figure 4.10). Across subjects, the averaged open-loop RMS gamma power increase was 11.8%, as determined directly from the experimental data, whereas in the closed-loop stimulation, the mean RMS gamma power increase was 22.8% using the LQI controller. Figure 4.11 shows the simulated closed-loop

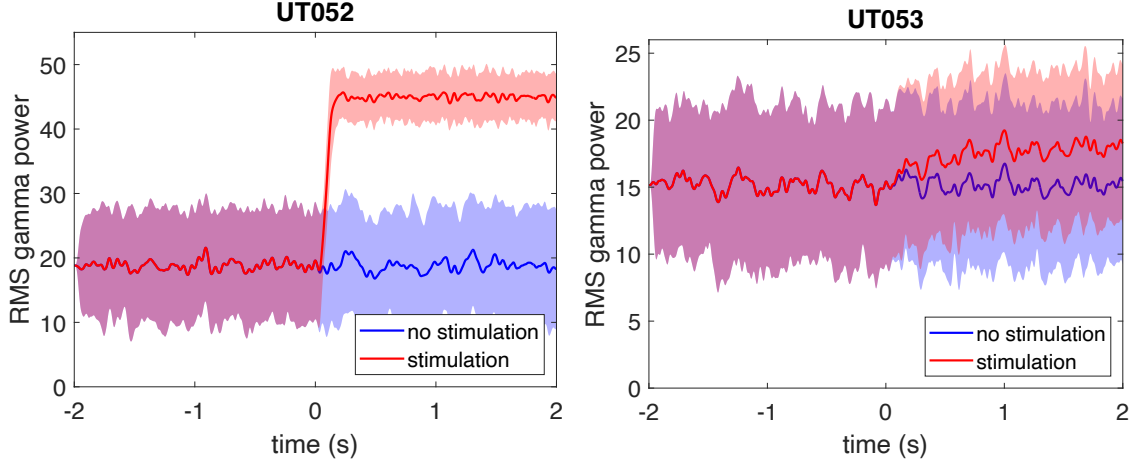


Figure 4.9: LQI controller simulations with control signal starting at $t = 0$ s for several subjects, showing mean and standard deviations over 100 independent trials.

RMS gamma power for each subject versus the desired setpoint. The normalized error was around -3% averaged over all subjects. We discovered that the slight negative error was likely due to stimulation amplitude being limited (partially saturated) to 9 mA while the controller was needing additional current to reach the setpoint.

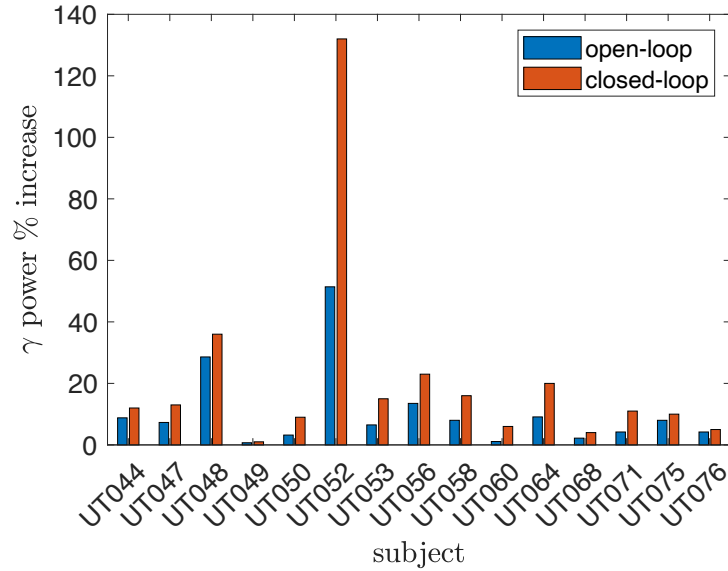


Figure 4.10: Percent increase in RMS gamma power ($\Delta\gamma\%$, see (4.3.1)) for open-loop (based on iEEG data) and closed loop conditions. The closed-loop results are based on simulated LQI control and had a mean of 22.8% across all subjects compared to 11.8% for the open loop condition.

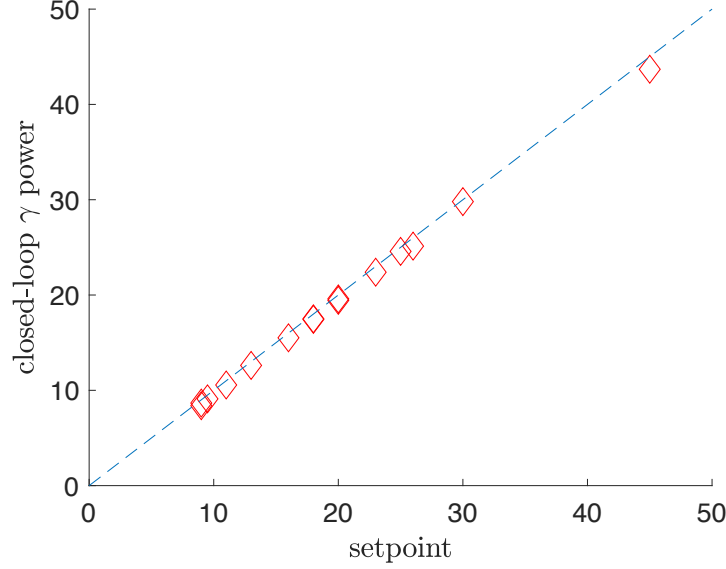


Figure 4.11: Simulated closed-loop RMS gamma power versus desired RMS gamma power setpoint.

4.4. Discussion

We designed a closed-loop brain computer interface system for modulating hippocampal gamma oscillatory power using an LQI controller derived from a linear ARX model, which was identified using our PCC-applied FR stimulation data with measured responses in the hippocampus (Natu et al., 2019). We sought to demonstrate the feasibility of a precise control of the hippocampal oscillation while stimulating the PCC, and eventually to improve memory performance in humans. We believe such a BCI can also be applied to test specific hypotheses regarding gamma band contributions to memory processing. As discussed in Section 4.3.1, the use of the PCC as a DBS target region for neuromodulation rests in part on the ability to see predictable effects on gamma power in the presence of stimulation, as well as established anatomical connectivity in humans (B. Lega, Germei, et al., 2017). The choice of hippocampal gamma power as a target biomarker for control in our BCI system was based on established empirical and theoretical data that connect hippocampal gamma band oscillatory activity and episodic memory, spatial navigation, and associative encoding (Griffiths et al., 2019; Zion-Golumbic et al., 2010; Negrón-Oyarzo et al., 2018). Surely, our BCI system needs

to be tested in memory-relevant tasks to demonstrate the capacity of improving memory performance across a large number of subjects, and we intend to investigate this in subsequent experimentation. Additionally, it would be beneficial to identify narrow gamma frequency ranges that most strongly predict encoding success for an individual recording location, and then to model the impact of different stimulation frequencies on this signal. Such an approach would require varying the stimulation parameters used in system identification, as discussed below, but may represent a more efficient method for parameter identification as compared to the grid search approach used in existing closed loop systems for memory modulation (Ezzyat et al., 2018). We focused on modulation of gamma rather than theta oscillatory activity. In rodents, restoration of pharmacologically or anatomically reduced theta activity is capable of restoring memory function (McNaughton et al., 2006). However, human theta oscillations exhibit a greater diversity across a broad 2–10 Hz frequency range, and not all subjects exhibit persistent theta frequency power increases that predict successful encoding (Jacobs, J. Miller, et al., 2016; Zhang and Jacobs, 2015; Lin, Rugg, et al., 2017). Targeting memory-relevant theta activity remains an active area of investigation; adjustment of PCC-applied stimulation parameters may be an effective approach given strong functional connectivity between the PCC and hippocampus during episodic memory processing (B. Lega, Germei, et al., 2017; Choi et al., 2020).

We utilized an ARX model to characterize the effect of PCC-applied stimulation on hippocampal neural activity. For this, we first validated the model quality metrics using two random processes to demonstrate that the choice of ARX model for hippocampal RMS gamma power was reasonable. Then, we showed that our ARX model exhibits good performance in predicting hippocampal gamma power, as well as representing critical spectral characteristics in the predictions. Our results revealed that the ARX model predicted random fluctuations in instantaneous gamma power during both stimulation and no-stimulation conditions and that the modeled output closely matched experimental data. In simulated closed-loop control, our LQI controller showed capability of reaching the setpoint in a clinically-relevant time

scale and staying within stimulation safety guidelines in all tested subjects. Our BCI design suggests we can achieve robust control of RMS gamma power at physiologically safe using this linear modeling approach, although some subjects only experienced modest increases. Because, the increase in gamma oscillatory power under closed-loop control ultimately depends on the power increase achievable during open-loop stimulation. This can be seen in Figure 4.12. We believe linear models offer several advantages for design of a controlled system.

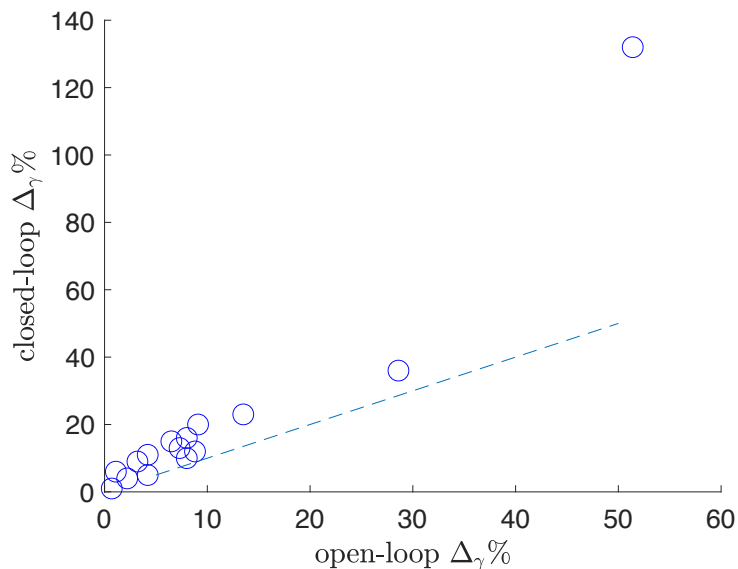


Figure 4.12: Percent RMS gamma power increases for open-loop vs closed-loop stimulation. The dashed line has a slope of one.

For instance, we are able to implement a robust and computationally efficient state-space based controller (LQI controller) while eliminating the need for a state estimator. These state-space based linear models have been successfully applied to complex dynamical brain systems for underlying surface EEG (Izhikevich, 2007), magnetoencephalography (Lamus et al., 2012; Daunizeau and K. J. Friston, 2007), and local field potential data (Agarwal et al., 2014).

Importantly, we would like to address the safety concerns regarding our BCI control mechanism. In previous work, we demonstrated the safety of PCC-applied DBS for a relatively long period of time (over 20 seconds) as a distinct feature of our underlying data (see

Chapter 3 and Natu et al., 2019). We followed the same clinical safety guideline when designing our LQI controller and testing the closed-loop control in simulated environment. As an optimal controller, we believe the choice of LQI gives us more leverage to achieve higher target power level meanwhile maintain a relatively low stimulation amplitude, as well as rapid closed-loop control response. Unlike some of reported BCI systems that focus on modulating and stimulating the same brain target/network (Ezzyat et al., 2018; Jacobs, J. Miller, et al., 2016), our focus on hippocampal response permits relatively artifact-free recordings for modeling. More so, these were collected while individuals were engaged in memory behavior, which is a distinct advantage compared to approaches in which stimulation parameters are selected when the patients are at rest, or when stimulation is applied for a limited number of memory items (M. T. Kucewicz et al., 2018). We intend to improve the generalizability of our BCI system across more participants and extend its capabilities across a range of brain signals (as biomarkers). This will require our knowledge of how neuromodulation of gamma power impacts other critical hippocampal oscillatory power (e.g. theta power), which can be examined by additional empirical data using our closed-loop stimulation system. More generally, regarding the goal of improving memory, the relative merits of a control system built on complex, multivariate brain signals versus a single well-established biomarker such as hippocampal gamma power remain a clear target of subsequent empirical investigation.

4.5. Conclusion

Our development of a close-loop brain-computer interface targeting a precise control of hippocampal gamma power would impact the field of neuromodulation for memory restoration. Our analysis of changes in the hippocampal gamma oscillation in response to PCC-applied stimulation suggests that using the PCC as a DBS target may be a propitious strategy. Our modeling strategy incorporates the previous open-loop FR stimulation data and seeks to describes the system input-output relationship between physiological stimulation applied to the PCC and the corresponding hippocampal neural activity. We finally

demonstrate the capability of modulating and controlling hippocampal RMS gamma power, as the biomarker, in all tested human subjects safely and in realistic time scales using an LQI servo-controller, based on our linear ARX modeling. We believe our proposed BCI system offers a promising approach for the neuromodulation of memory.

CHAPTER 5

CLOSED-LOOP BRAIN-COMPUTER INTERFACES FOR MODULATING HIPPOCAMPAL OSCILLATORY ACTIVITY VIA BINARY-NOISE STIMULATION

5.1. Introduction

Therapeutic brain-computer interfaces (BCIs) for modulating brain activity have drawn considerable attention for treating neurological disorders in the past ten years. Deep brain stimulation (DBS) techniques have emerged for treating a variety of brain dysfunctions (Hoang et al., 2017; Shanechi, 2019). Such DBS systems are effective for treating neurodegenerative disorders such as epilepsy (B. C. Lega, Halpern, et al., 2010; Fisher et al., 2010), Parkinson’s Disease (Deuschl, Schade-Brittinger, et al., 2006; Deuschl and Agid, 2013), and Alzheimer’s Disease (Laxton and Lozano, 2013; Lozano et al., 2016), as well as for neuropsychotic disorders such as depression (Mayberg et al., 2005; C. Zhou et al., 2018) and schizophrenia (Corripio et al., 2020). Often, BCI systems for targeting movement disorders are open-loop, which relies solely on preset empirically derived stimulation parameters from clinical trials. However, unlike movement disorders, the underlying brain circuitry for memory disorders is more sophisticated and likely requires investigation of brain activity patterns or biomarkers as neuro-feedback to govern subsequent stimulation parameters in a closed-loop format. Results have shown that open-loop schemes often fail to capture the drastically changing dynamics of the neurological activities associated with cognitive processes, and some even impaired memory performance. In contrast, closed-loop stimulation for this task has shown greater potential for memory restoration and achieved empirical success in improving memory performance. For instance, the DARPA founded Restoring Active Memory (RAM) program proposed a classifier-based closed-loop stimulation system

and demonstrated a 15% average increase in memory performance across 40 participants (Ezzyat et al., 2018), and the CLoSES platform described a closed-loop DBS system targeting brain states based on the predetermined threshold (Zelmann et al., 2020). Yet, these types of systems are inadequate for temporal resolution needed for desired biomarkers (or model features). For instance, the classifier in the RAM program utilizes a feature extracted from a 700 *ms* neural recordings to predict memory success and the standby stimulator with fixed parameters (amplitude and frequency) is triggered whenever the classifier predicts a failure of memory encoding. Similarly, the CLoSES-REM system estimates the brain states via features averaged across a 2 *sec* recording then triggers the stimulation with preferred parameters. Although this type of closed-loop BCI system is found to be empirically successful, one critical point is that it sacrifices important temporal dynamics since neural activities change rapidly, especially in memory processes. Moreover, such scheme of on-demand stimulation with preset parameters presents another critical question regard what stimulation parameters to apply.

To answer this question, recent studies reported fruitful approaches via computational dynamic modeling, which reveals the neural circuitry underlying the input-output (I/O) time-series. For instance, neural mass models describe the oscillatory activity within a group of neurons (I. Basu et al., 2018), and dynamic causal modeling uses state-space parameterization of region-region interactions in the brain (Stephan et al., 2010). However, these neurophysiological models often focus on a group of neurons or are disease-specific, making them challenging to implement across the board of neural activities due to the lack of generalizability. Data-driven models are more versatile and capable of modeling the neural I/O dynamics during behavioral tasks or stimulation. For instance, the linear state space model (LSSM) paired with a linear quadratic integral (LQI) controller shows great potential in modulating brain mood (Shanechi, 2019; Yang, Connolly, et al., 2018) and this strategy has recently been extended to modulate a large-scale brain network (Yang, Qiao, et al., 2021). Moreover, in our previous work (discussed in Chapter 4), we tested and demonstrated the

feasibility of a control-theoretical system using linear autoregressive with exogenous input (ARX) model paired with a linear quadratic regulator (LQR) controller in modulating the desired memory-relevant biomarker (gamma oscillatory power). Here, we apply a similar principle to develop a BCI system for modulating stimuli-evoked memory biomarkers with a novel stimulation dataset for better neuromodulating and predicting I/O dynamics. We now select both hippocampal theta and gamma oscillatory power as our biomarkers for memory because of the well-established fact that power changes in these bands predict memory success from numerous studies in rodents and humans (Sederberg, M. J. Kahana, et al., 2003a; Fries, 2009; Steinvorth et al., 2010; Sederberg, Schulze-Bonhage, et al., 2007; Kota et al., 2020; Jacobs, B. Lega, et al., 2017; Sederberg, M. J. Kahana, et al., 2003b; Jacobs, 2014; Lin, Rugg, et al., 2017). We compared stimuli-evoked changes in these two bands as they show drastically varied temporal dynamics in memory encoding (Natu et al., 2019; Jacobs, J. Miller, et al., 2016). We chose posterior cingulate cortex (PCC) as our stimulation target due to its dense connectivity to a variety of brain regions including the hippocampus (Bai et al., 2009; Khalsa et al., 2014; Wang, Schmitt, et al., 2021). More importantly, our previous work has not only demonstrated stimulating the posterior cingulate cortex (PCC) consistently elicits increases in hippocampal gamma power and conveys dynamical changes in the theta band (Natu et al., 2019), but also established that these changes in hippocampal oscillatory power can be modulated via precise control of PCC-applied stimulation. In addition, we adapted and developed a PCC-applied binary-noise (BN) stimulation paradigm in which the stimulation pattern was generated randomly (binary, uniformly distributed). We incorporated this paradigm with the Cerestim stimulator and NSP intracranial EEG (iEEG) recording module manufactured by Blackrock Neurotech (Details are found in Chapter 3).

We developed a closed-loop BCI system for memory neuromodulation based on binary-noise deep brain stimulation applied to the PCC using a novel nonlinear autoregressive with exogenous input neural network (NARXNN) as the plant model, paired with a robust proportional-integral-derivative (PID) controller. We also implemented a linear state-space

model (LSSM) with PID controller as the benchmark to demonstrate the superior performance of our NARXNN-PID control strategy. We show that our NARXNN architecture provides better accuracy in modeling the dynamics between PCC-applied stimulation and stimuli-evoked hippocampal theta and gamma power, as well as its effectiveness in controlling and modulating theta and gamma power to a desired target level in all 12 subjects using our NARXNN-PID BCI framework.

5.2. Materials and Methods

5.2.1. Participants

A total of 12 participants (ages 22-63, 5 female and 7 male) with medication-resistant epilepsy were recruited at the epilepsy monitoring unit (EMU) in the Clements University Hospital at the UT Southwestern Medical Center. All participants underwent stereo-electroencephalography (sEEG) for localizing their seizure region(s) and had intracranial electrodes implanted within the ipsilateral posterior cingulate cortex and hippocampus (anterior and/or posterior hippocampus). Contacts localization was achieved by co-registration of the post-operative computer tomography scans with pre-operative magnetic resonance images and evaluated by a member of the neuroradiology team to determine the final electrode locations. The research protocol was approved by the UT Southwestern Medical Center Institutional Review Board, and each patient granted informed consent prior to stimulation paradigm and data collection.

5.2.2. Binary-Noise Stimulation Paradigm and Data Acquisition

Each subject participated in the stimulation paradigm was asked to remain calm and minimize physical movement for collecting resting-state iEEG recordings while binary-noise stimulation sessions were performed. The stimulation task was operated at the patient's

Table 5.1: Demographic information of participants in BN stimulation paradigm. MTL: Medial temporal lobe, NTL: Neocortical temporal lobe, LH/RH: left/right hemisphere, B: bilateral.

Subject No.	Age	Type of epilepsy	Hemisphere	Duration of epilepsy
1	22	Multifocal	LH	3
2	30	Right NTL	RH	13
3	34	Left MTL	LH	11
4	54	Right MTL	RH	14
5	52	Multifocal	LH	50
6	41	Left MTL	LH	38
7	29	Right NTL	RH	10
8	47	Bilateral MTL	B	46
9	35	Multifocal	B	19
10	63	Multifocal	R	62
11	40	Bilateral MTL	B	24
12	48	Right MTL	RH	5

bedside on the caster of NSP system (PC) and Cerestim stimulator manufactured by Blackrock Neurotech that runs in parallel to the Nihon Kohden NeuroFax clinical EEG system monitored by EMU technicians. For safety concerns, this stimulation paradigm provides an additional intracranial (LX2 or RX2, the adjacent channel to the stimulation target) and a surface grounding placed on the patient’s, with a power kill-switch within the operator’s reach. For all 12 participants, no bleeding, sickness or seizure attack were reported. Each stimulation session consisted of ninety 2-second non-stimulation and ninety 2-second stimulation events, where the amplitude of stimuli randomly switches from 1 *mA* to 2 *mA* and the frequency switched from 100 Hz to 150 Hz. The 128-channel iEEG was recorded at 1 *kS/s* via the digital ports of the NSP system and the recordings were then parsed and aligned into event trials by event sync pulses using the Blackrock NSP API in MATLAB software (details are found in Chapter 3). We propose a closed-loop BCI framework for control of hippocampal oscillatory power via BN stimulation using the Blackrock Neurotech system as shown in Figure 5.1 (Brain mapping of the PCC and hippocampus was generated by the

open-source BrainPainter by Marinescu et al.). The signal processing and the PID controller are discussed in Section 5.2.3 and Section 5.2.6, respectively.

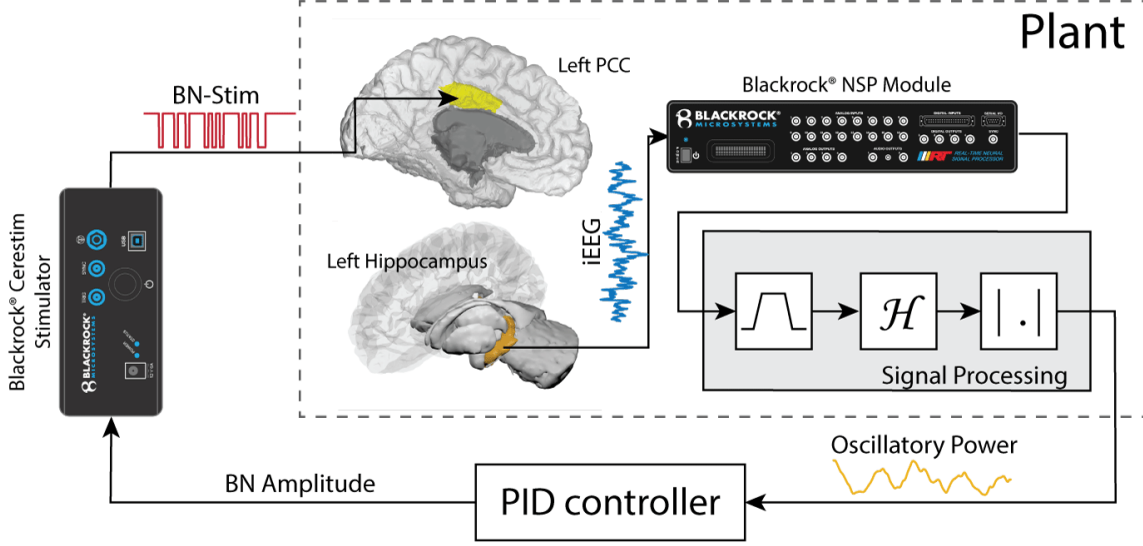


Figure 5.1: Brain-computer interface framework for control of hippocampal RMS gamma/theta power with Blackrock Cerestim stimulator and NSP module in the loop.

5.2.3. Data Processing

5.2.3.1. *iEEG Denoising*

Although our configuration of the stimulation paradigm and EEG acquisition rejects the majority of stimulation artifacts and line-noise (see Chapter 3), parsed EEG trials were further examined for outliers and remaining noise/artifacts. For outliers, mean Euclidean distance (MED) was computed for each trial with respect to an arbitrary reference trial. The MED can be written as:

$$MED(i) = \sqrt{\frac{1}{N} \sum_{j=1}^n (x_i(j) - x_r(j))^2} \quad (5.1)$$

where $i = 1, 2, 3, \dots, M$ is the trials number, $j = 1, 2, 3, \dots, N$ is the sample number of the trial, and x_r is the reference trial for which an arbitrary trial can be selected. The majority of MEDs fluctuate within a stable range whereas outliers exceed the range dramatically. In our case, we used the first trial as a reference and trials exhibited 75% greater than averaged MED were rejected. Then, EEG trials were downsampled to 500Hz followed by an anti-aliasing lowpass filtering at 200 Hz, and were further denoised via a subspace approach such that (Wang and Davila, 2019):

$$B = A Q_s Q_s^T = [s_1(t)^T, s_2(t)^T, s_3(t)^T, \dots, s_m(t)^T]^T \quad (5.2)$$

where $A = [x_1(t)^T, x_2(t)^T, x_3(t)^T, \dots, x_m(t)^T]^T$ is the matrix of EEG trials, Q_s is matrix of the principle eigenvectors decomposed from the sample correlation matrix $\hat{R} = A^T A$, and $s_i, i = 1, 2, 3, \dots, M$ are the projections of individual trials onto the signal subspace. Here, we selected the first r -th eigenvectors that explained at least 80% variance of the correlation matrix and this was evaluated by the sorted corresponding eigenvalues.

5.2.3.2. Hippocampal Oscillatory Power

In this study, we focus on modulating hippocampal oscillatory power in the theta and gamma bands instead of the actual oscillations in these frequency bands because 1) it is well-established that the changes of oscillatory power in these bands are highly associated with neuropsychological activity, especially in the formation of new memories (Klimesch, 1999; Kota et al., 2020; Jacobs, B. Lega, et al., 2017), and 2) it is not necessary and technically challenging to model the full-spectrum of iEEG with high temporal resolution. Thus, we selected the oscillatory power in the 5-9 Hz theta band and the 30-50 Hz low gamma band as our ‘biomarkers’. The instantaneous root mean square (RMS) power in each frequency band was obtained via the Hilbert transform:

$$a_{x\gamma}(t) = \sqrt{\mathcal{H}(x_\gamma(t))^2} \text{ and } a_{x\theta}(t) = \sqrt{\mathcal{H}(x_\theta(t))^2} \quad (5.3)$$

where $x_\gamma(t)$ and $x_\theta(t)$ denote the bandpass filtered EEG trials for the gamma and theta ranges, respectively.

5.2.4. Linear State-Space Modeling

We selected the linear state-space model (LSSM) as a benchmark to evaluate both linear and nonlinear approaches for capturing the oscillatory dynamics in theta and gamma bands. For a discrete system, an LSSM uses state variables to describe a system by a set of first-order difference equations. Such a model is a good choice for estimating the system since it only requires input-output data and the model order to which the state variables are associated. Further, several recent studies have demonstrated the effectiveness and efficiency of such LSSM structure in modeling dynamic biomarkers (Yang, Qiao, et al., 2021; Yang, Connolly, et al., 2018). A discrete LSSM can be written as:

$$\begin{aligned} x_{t+1} &= Ax_t + Bu_t + w_t \\ y_t &= Cx_t + Du_t + v_t \end{aligned} \quad (5.4)$$

where x_t is the system state variable, u_t is the BN stimulation pattern, y_t is the experimental measurement of the oscillatory power, and w_t , and v_t are the (scalar) system disturbance and observation noise signals, respectively.

The parameters of the LSSM are estimated via the least squares approach. Assume the state variable x_t is also measured, and let:

$$Y_t = \begin{bmatrix} x_{t+1} \\ y_t \end{bmatrix}, \quad \Theta = \begin{bmatrix} A & B \\ C & D \end{bmatrix}, \quad \Phi_t = \begin{bmatrix} x_t \\ u_t \end{bmatrix}, \quad E_t = \begin{bmatrix} w_t \\ v_t \end{bmatrix} \quad (5.5)$$

then, equation 4.15 can be re-written as:

$$Y_t = \Theta \Phi_t + E_t \quad (5.6)$$

and the k-step ahead predictor is given by:

$$\hat{Y}_{kt} = \hat{\Theta}_N \phi_{st} \quad (5.7)$$

where $\phi_{st} = [y_{t-1}^T, \dots, y_{t-s1}^T, u_{t-1}^T, \dots, u_{t-s2}^T]^T$, $s1$ is the past output and $s2$ is the past input, and $\hat{\Theta}_N$ is estimated using least square method to solve $Y_{kt} = \Theta \phi_{st} + \Gamma_t U_{lt} + E_t$ given that:

$$U_{lt} = [u_{t-1}^T, \dots, u_{t+l-1}^T]^T \quad (5.8)$$

$$E_t = [\epsilon_t^T, \dots, \epsilon_{t+k-1}^T]$$

Detailed explanations are found in (Ljung, 1999). We utilized the System Identification Toolbox in MATLAB for estimating 8–th order LSSM parameters using the multi-experimental I/O data (MathWorks, 2020), and we built separate models for both theta and gamma RMS power for each subject.

5.2.5. Nonlinear Autoregressive-Exogenous Neural Network

It is well-known that cognitive neural activity is difficult to predict and classified due to the nonlinear relationship between external stimuli and stimuli-evoked electrophysiological responses (Pradhan et al., 2012; Kannathal et al., 2005; C. Stam et al., 1996). A

variety of nonlinear dynamical analyses of EEG have been published for decoding different brain states such as during no-task resting-states, perceptual processing, and various behavioral tasks (Elger et al., 2000; C. J. Stam, 2005; Jeong, 2004). In addition, numerous neurophysiologically inspired models have been developed for reconstructing the nonlinear dynamics within a small group of neurons. For instance, the famous Hodgkin–Huxley model, a conductance-based model, describes how membrane potentials in neurons are excited and inhibited via a set of nonlinear differential equations (Hodgkin and Huxley, 1952), and the neural mass model (NMM) resembles the dynamics of the firing rate in response to the external stimulus applied to the excitatory and inhibitory neurons (Jansen and Rit, 1995). We investigated the NMM in our initial attempt and found estimating a NMM in the format of a grey-box model required enormous computational resources for the ordinary differential equation solver given our dataset, and changing the model structure (manipulating numbers of neuron groups) increased computational time exponentially, despite the mathematical simplicity and versatility of the NMM in analyzing event-related potentials and neuronal spiking activities (Coombes and Byrne, 2019). It is preferable to implement a nonlinear model that is easy to manipulate and optimize in a realistic time scale. For this reason, we selected a nonlinear autoregressive with exogenous input neural network (NARXNN) as our nonlinear model for the plant due to its ease of use, computational efficiency, and most importantly, its superior performance in predicting a complex system (Xie et al., 2009; Diaconescu, 2008; Ardalani-Farsa and Zolfaghari, 2010; Menezes Jr and Barreto, 2008).

The architecture of such a NARXNN consists of a nonlinear ARX model (linear ARX model with nonlinear activation function) optimized by a multilayer perceptron (MLP) neural network arranged typically in a shallow structure (less than three layers). Given the model input $u(t)$ and model output $y(t)$ at discrete time t , the I/O dynamics can be written as:

$$y(t+1) = f[y(t), \dots, y(t-d_y); u(t), \dots, u(t-d_u)] \quad (5.9)$$

where $d_u \geq 1$ is the input delay, $d_y \geq 1$ ($d_y \geq d_u$) is the output delay, and $f(\cdot)$ is the nonlinear transfer function to be estimated by the MLP architecture. In general, unlike the vast majority of artificial neural networks, NARXNN does not achieve prediction of a chaotic time-series by extending the number of hidden layers, rather, it is a dynamic neural network and relies on recurrent feedback (Leontaritis and Billings, 1985; Ljung, 1999; Norgaard et al., 2000). Therefore, we implemented a two-layer NARXNN (one hidden layer and one output layer) for modeling both RMS theta and gamma power. The architecture of our NARXNN model is shown in Figure 5.2, and it can be written as

$$y(t+1) = f_0 \left[b_0 + \sum_{h=1}^{Nh} w_{h0} \cdot f_h \left(b_h + \sum_{i=0}^{d_u} w_{ih} u(t-i) + \sum_{j=0}^{d_y} w_{jh} y(t-j) \right) \right] \quad (5.10)$$

where w_{ih} and w_{jh} are the weights in hidden layer for delayed input and output, respectively, b_h is the bias in the hidden layer, w_{h0} and b_0 are the weights and bias in the output layer, and f_0 (linear) and f_h (sigmoid) are the activation functions of the output and hidden layer, respectively.

In fitting NARXNN to the I/O data, we took advantage of multi-sequence training and temporal-wise attention (TA) techniques (Han et al., 2021). The multi-sequence training is a network training procedure used when the time-series data is not available in one long sequence. For instance, our I/O data consisting of the BN stimulation sequence and the hippocampal gamma/theta power have the same temporal values across trials. Thus, a concurrent dataset like ours needs to be trained with multi-sequence training for the network, where each epoch back-propagates and optimizes the network parameters on a trial-to-trial basis by concatenating all the I/O trials, and the delay is reset for each trial to maintain the same temporal scheme (i.e. $y_i(t), \dots, y_i(t-d_y)$ and $u_i(t), \dots, u_i(t-d_u)$, $i = 1, 2, \dots, m$). See

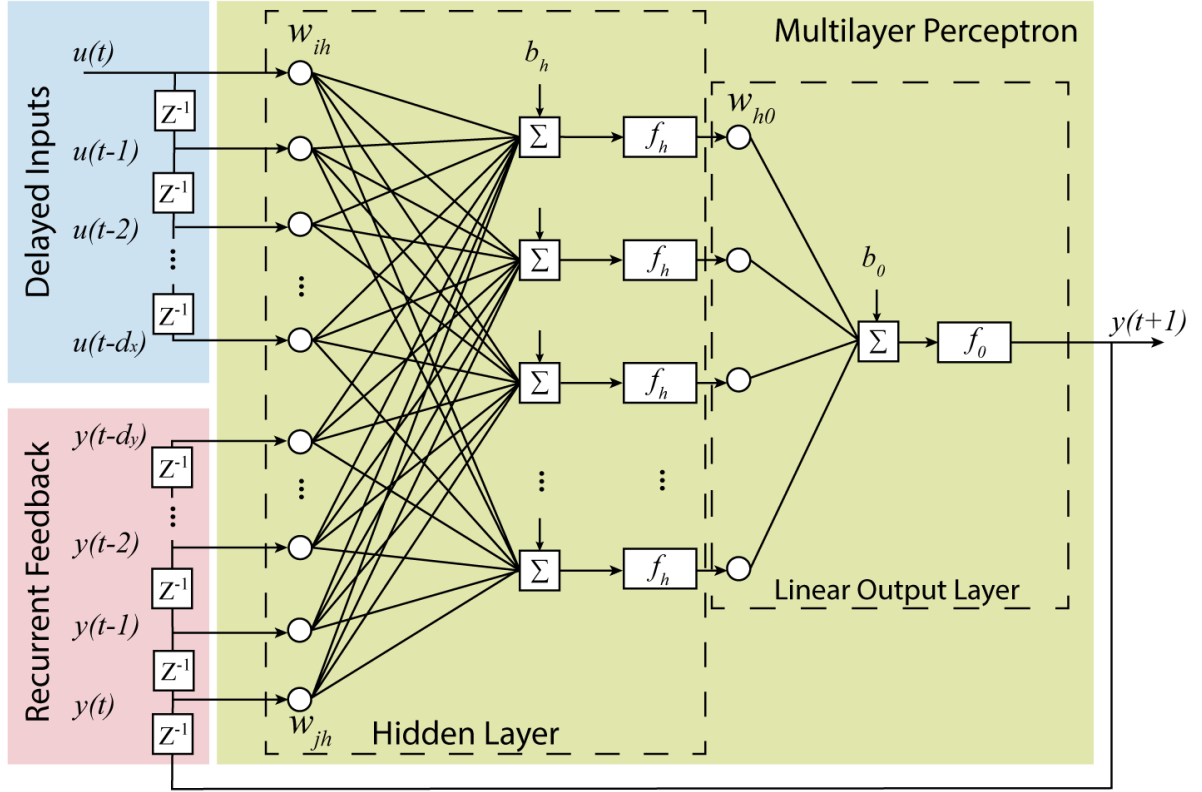


Figure 5.2: The architecture of NARXNN with one hidden layer and one output layer. d_x is the order delayed inputs and d_u is the order of delayed outputs. f_h is the sigmoid activation function and f_0 is a linear function.

Figure 5.3). On the other hand, the TA technique is essentially a multi-rate data batching technique that has been commonly used in modern complex tasks such as computer vision and natural language processing (Leontaritis and Billings, 1985; Galassi et al., 2020; Yao et al., 2021; Gatt and Krahmer, 2018; Young et al., 2018). This “attention” mechanism parses a multi-sample sequence into smaller temporal windows that dynamically highlights relevant sequential features of the I/O data, and it can be applied directly to the raw input or to its higher level representation (Galassi et al., 2020). Therefore, we implemented this TA technique to further extract temporal-relevant features to train the NARXNN plant and we selected a temporal window of 40 *ms* by trading-off the computational efficiency and the model accuracy, empirically.

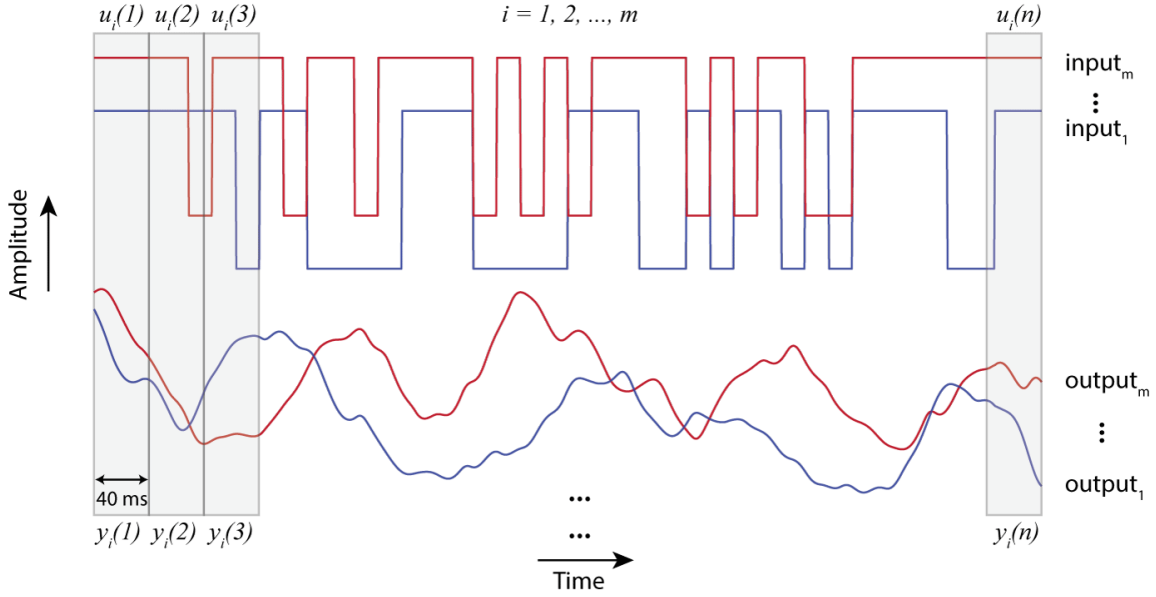


Figure 5.3: Illustration of batching I/O data into TA segments, where each batch is 40 ms long (20 samples), $u_i(1), u_i(2), \dots, u_i(n)$ and $y_i(1), y_i(2), \dots, y_i(n)$, $i = 1, 2, 3, \dots, m$ are the input and output to the NARXNN model, respectively.

As illustrated in Figure 5.3, the I/O trials are batched input TA segments. On discrete sample basis, the input is now $u_i = [u_i(1), u_i(2), \dots, u_i(n)]$ where $i = 1, 2, 3, \dots, m$ is the number of trials for the subject, and the output is $y_i = [y_i(1), y_i(2), \dots, y_i(n)]$, accordingly. Each batched sample consists of a 20-sample long feature (40 *ms*) such that $u_i(j) = [I_i((j -$

$1) \times 20 + 1), I_i((j - 1) \times 20 + 2), \dots, I_i(j \times 20)]$ and $y_i(j) = [O_i((j - 1) \times 20 + 1), O_i((j - 1) \times 20 + 2), \dots, O_i(j \times 20)]$, where I_i and O_i are the original I/O trials. In addition, we used a Bayesian regularization algorithm to minimize the squared error. This algorithm uses the Levenberg-Marquardt backpropagation, which computes the Jacobian matrix $j\mathbf{w}$ of the mean squared error (MSE) with respect to the weight and bias variables \mathbf{w} . Each variable is adjusted according to Levenberg-Marquardt (Foresee and Hagan, 1997):

$$\begin{aligned} jj &= j\mathbf{w}^T j\mathbf{w} \\ je &= j\mathbf{w}^T E \\ d\mathbf{w} &= -(jj + I\mu) je \end{aligned} \tag{5.11}$$

where E is the matrix of errors, I is the identity matrix, and the step size μ is adaptively increased until the epoch reduces the performance in minimizing the MSE. The Bayesian regularization is a powerful approach to prevent overfitting and to smooth the network response. According to Bayes' rule, parameters of a network are considered as random variables and can be written as:

$$P(\mathbf{w} \mid D, \alpha, \beta, M) = \frac{P(D \mid \mathbf{w}, \beta, M)P(\mathbf{w} \mid \alpha, M)}{P(D \mid \alpha, \beta, M)} \tag{5.12}$$

where α and β are parameters for the objective function such that $E = \beta E_D + \alpha E_W$, where E_W is the sum of squares of the network weights and E_D is sum of squared errors $E_D = \sum_{j=1}^n (y(j) - \hat{y}(j))^2$. D is the data set, M is the network model used, and \mathbf{w} is the vector of network parameters. $P(\mathbf{w} \mid \alpha, M)$ is the prior density representing the knowledge of the network parameter prior to any data collection. $P(D \mid \mathbf{w}, \beta, M)$ is the likelihood of the data occurring, given the parameter \mathbf{w} . $P(D \mid \alpha, \beta, M)$ is a normalization factor with

total probability of 1. And, this normalization factor can be solved by:

$$\begin{aligned}
P(D \mid \alpha, \beta, M) &= \frac{P(D \mid \mathbf{w}, \beta, M)P(\mathbf{w} \mid \alpha, M)}{P(\mathbf{w} \mid D, \alpha, \beta, M)} \\
&= \frac{\left[\frac{1}{Z_D(\beta)} \exp(-\beta E_D) \right] \left[\frac{1}{Z_W(\alpha)} \exp(-\alpha E_W) \right]}{\frac{1}{Z_F(\alpha, \beta)} \exp(-F(\mathbf{w}))} \\
&= \frac{Z_F(\alpha, \beta)}{Z_D(\beta)Z_W(\alpha)} \cdot \frac{\exp(-\beta E_D - \alpha E_W)}{\exp(-F(\mathbf{w}))} \\
&= \frac{Z_F(\alpha, \beta)}{Z_D(\beta)Z_W(\alpha)}
\end{aligned} \tag{5.13}$$

and

$$\begin{aligned}
Z_F(\alpha, \beta) &\approx (2\pi)^{N/2} \left(\det \left((\mathbf{H}^{\text{MP}})^{-1} \right) \right)^{1/2} \exp(-F(\mathbf{w}^{\text{MP}})) \\
Z_D(\beta) &= \frac{1}{P(D \mid \mathbf{W}, \beta, M)} \exp(-\beta E_D) \\
Z_W(\alpha) &= \frac{1}{P(\mathbf{w} \mid \alpha, M)} \exp(-\alpha E_W)
\end{aligned} \tag{5.14}$$

where $\mathbf{H} = \beta \nabla^2 E_D + \alpha \nabla^2 E_W$ is the Hessian matrix of the objective function. In short, Bayesian regularization minimizes the linear combination of squared errors and weights so that the resulting network has good generalization qualities at the end of training. The detailed proof and explanations are found in Foresee and Hagan, 1997, and MacKay, 1992.

5.2.6. Proportional–Integral–Derivative Controller

The proportional–integral–derivative (PID) controller is a non-model-based control mechanism that constantly adjusts the control signal by referencing the error $e(t)$ between setpoint and feedback. We implemented the PID controller for two major reasons:

1. The PID controller is not a model-based and can work for both of the LSSM and NARXNN plants without linearization.
2. The PID controller is relatively easy to tune for its response as it only has three terms.

First, our NARXNN plant is a nonlinear model so that a linear controller such as LQI or LQR is not compatible. For solving this problem, a common approach is to linearize the nonlinear plant model. In our initial attempt, we found that linearizing a NARXNN plant sacrificed the model performance dramatically due to the highly nonlinear I/O relationship. In an industrial control configuration, plants are often implemented with well-described physical models (e.g. thermal problems) or for control of system operational devices (e.g. robotic operations). Neither of these work with our objectives because it is challenging to describe the model using a set of differential equations or inapplicable to use the biological plant (i.e. the human subject) directly for testing a predictive controller without preliminary testing. Second, a PID controller is easy to tune because it only consists of three parameters, namely, proportional gain, integral gain and derivative gain for the error $e(t)$. The control function is given by:

$$u(t) = K_p e(t) + K_i \int_0^t e(\tau) d\tau + K_d \frac{de(t)}{dt} \quad (5.15)$$

where K_p , K_i , and K_d denote the gains for proportional, integral, and derivative terms, respectively. The PID control structure along with the NARXNN and LSSM plant models for our BCI framework is shown in Figure 5.4.

In the tuning of PID controller, we followed Ziegler–Nichols tuning method with three fundamental objectives (Ziegler, Nichols, et al., 1942; Åström et al., 2006):

1. Stability — The closed-loop system output remains bounded for bounded input.
2. Performance — The closed-loop system tracks and reaches desired setpoint as rapidly as possible.

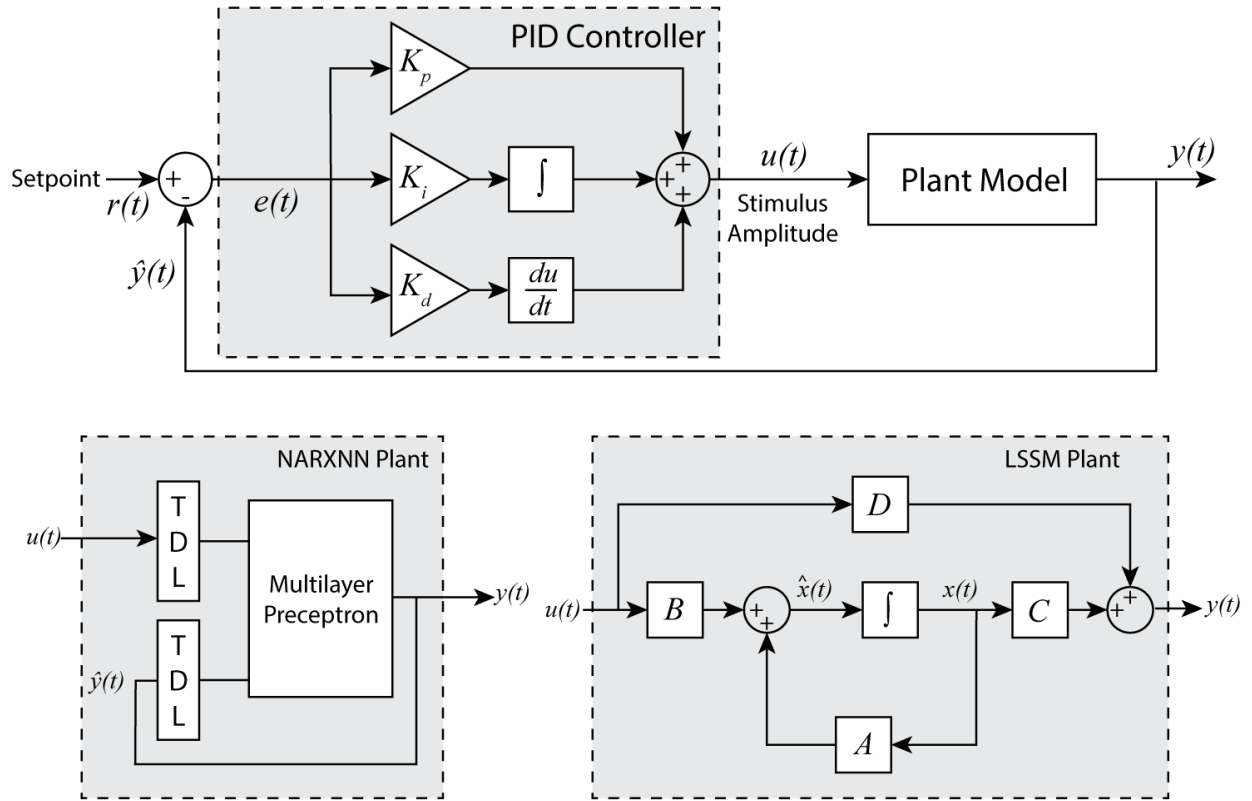


Figure 5.4: PID control structure with NARXNN and LSSM plants. TDL: tapered delay line

3. Robustness — The loop design has enough gain margin to allow modeling errors or variations in system dynamics.

and Ziegler-Nichols' method is a simple and powerful approach to achieve these objectives. Let $K_i = K_p/T_i$ and $K_d = K_p T_d$, where T_i and T_d are the integral and derivative time intervals, respectively, Equation 5.15 can then be rewritten as:

$$u(t) = K_p \left(e(t) + \frac{1}{T_i} \int_0^t e(\tau) d\tau + T_d \frac{de(t)}{dt} \right) \quad (5.16)$$

and can show it has a transfer function of:

$$\begin{aligned} u(s) &= K_p \left(1 + \frac{1}{T_i s} + T_d s \right) e(s) \\ &= K_p \left(\frac{T_d T_i s^2 + T_i s + 1}{T_i s} \right) e(s) \end{aligned} \quad (5.17)$$

Table 5.2: Ziegler-Nichols' PID tuning rules for K_p , K_i and K_d using the ultimate gain K_u and its oscillation period T_u .

Control Type	K_p	T_i	T_d	K_i	K_d
P	$0.5K_u$	-	-	-	-
PI	$0.45K_u$	$0.80T_u$	-	$0.54K_u/T_u$	-
PD	$0.8K_u$	-	$0.125T_u$	-	$0.10K_u T_u$
PID	$0.6K_u$	$0.5T_u$	$0.125T_u$	$1.2K_u/T_u$	$0.075K_u T_u$

The Ziegler-Nichols' first sets K_i and K_d to zero and increases K_p from zero until it reaches the ultimate gain K_u at which the system outputs a stable and consistent oscillation, which has a period of T_u . Then, it adjusts the T_i and T_d based on the oscillation period T_u . Ziegler and Nichols gave a typical rule for solving the PID parameter once ultimate gain is achieved (see Table 5.2, Ziegler, Nichols, et al., 1942). In practice, we followed this rule to tune the PID controller for the NARXNN plant manually, and used the PID

Tuner software, which uses the same method, via the MATLAB Control System Toolbox (<https://www.mathworks.com/products/control.html>).

5.3. Results

5.3.1. Stimulating the PCC Elicits Hippocampal Oscillatory Activity

A preliminary study on stimulating PCC in our research group suggests that PCC serves as a favorable DBS target for neuromodulation strategies using a priori connectivity measures to predict stimulation effects (Natu et al., 2019). Based on this, we developed control-theoretical systems to modulate the stimuli-evoked hippocampal oscillatory response with PCC-applied binary-noise DBS. We first compared the hippocampal mean RMS power across a 2-second time window in both theta and gamma bands for trials during open-loop stimulation and no-stimulation. We found that 9 out 12 subject experienced a power increase in the gamma band and 8 subjects exhibited power increase in the theta band. Using a one-tail paired t-test, we confirmed the gamma power increases in 6 out of the 9 subjects were significant, and 7 out of the 8 subjects were significant for the theta power ($p < 0.05, T > 1.96$). These results are found in Table 5.3 and 5.4.

Table 5.3: Averaged mean RMS gamma power across 2 s time window and across trials during stimulation (S) and no stimulation (NS). $\Delta\bar{Power}$ denotes the mean RMS power difference, and T-stats is by one-tailed t-test. LB/RB and LC/RC are left/right anterior and posterior hippocampus, respectively.

Subject No.	Contacts	\bar{Power}_S	\bar{Power}_{NS}	$\Delta\bar{Power}$	T-stats	Events
1	LB1	7.06	5.32	1.74	3.87	54
2	LB1	2.02	1.34	0.68	2.48	83
3	LB2	1.41	1.53	-0.12	-1.62	89
4	RB1	4.00	4.55	-0.54	-2.06	82
5	LB1	1.70	1.70	0.00	0.05	89
6	LC1	3.63	3.53	0.10	0.61	85
7	RB1	2.07	1.86	0.20	0.81	75
8	LB2	1.54	1.25	0.29	1.99	88
9	RC1	5.40	4.30	1.09	4.24	86
10	RB2	1.13	1.24	-0.10	-0.54	88
11	LB3	4.06	1.91	2.15	6.85	67
12	RC1	27.82	4.13	23.6	29.84	82

Table 5.4: Averaged mean RMS gamma power across 2 s time window and across trials during stimulation (S) and no stimulation (NS).

Subject No.	Contacts	\bar{Power}_S	\bar{Power}_{NS}	$\Delta\bar{Power}$	T-stats	Events
1	LB1	31.02	21.35	9.66	4.18	54
2	LB1	16.12	10.72	5.40	2.01	83
3	LB2	9.56	9.82	-0.25	-0.46	89
4	RB1	20.24	22.70	-2.45	-1.76	82
5	LB1	10.46	11.03	-0.57	-0.75	89
6	LC1	26.187	21.71	4.47	3.78	85
7	RB1	12.75	10.30	2.44	1.43	75
8	LB2	12.30	9.70	2.59	3.99	88
9	RC1	24.12	20.69	3.42	3.41	86
10	RB2	8.38	7.048	1.33	1.03	88
11	LB3	21.35	16.19	5.16	2.68	67
12	RC1	15.37	9.788	5.5	8.47	82

Next, we investigated dynamical changes of the stimuli-evoked hippocampal oscillatory power in the theta and gamma bands. In Figure 5.5 and 5.6, we show the theta and gamma RMS power trials in a time window of 400 *ms* before the stimulation (i.e. -400 *ms*) to 1600 *ms* after the stimulation (i.e. +1600 *ms*), where stimuli were onset at 0 *ms*. Because of the various power levels across different subjects, these power trials were normalized in z-scores (subtract mean then divide by S.D.). We observed increases in the gamma power within a short period after stimulation in 11 out of 12 subjects, and this happened 86.5 ± 72.36 *ms* after stimuli onset. Similar for the theta power, we observed power increases in all of 12 subjects and this power increase occurred at 133.2 ± 107.5 *ms* on average. To better understand the stimuli-evoked changes during stimulation versus absence of stimulation, we divided the power trials (0 *ms* - 1600 *ms*) into four segments and each of which had a time window of 400 *ms*, and we then computed the subsequent stimulation effects (SSE) of normalized power in each stimulation segments versus the power during no stimulation (i.e. power during -400 *ms* to 0 *ms* as baseline), independently. SSE computes the one-directional normalized changes in power such that $SSE = (\mu_S - \mu_{NS}) / \sqrt{(\sigma_S^2 + \sigma_{NS}^2) / 2}$. We found that both gamma and theta power experienced increases within the first 400 *ms* in respond to stimulation but the increases in theta band were overall less. Moreover, the increases of gamma power gradually decayed back to the baseline power level (during no-stimulation) from 800 *ms* to 1600 *ms*, and the theta power exhibited overall decreases within 800 *ms* to 1200 *ms*, after an initial increase within 0 *ms* - 400 *ms* followed much more diverse changes within 400 *ms* - 800 *ms* (median SSE showed increase). These results are found in Figure 5.7.

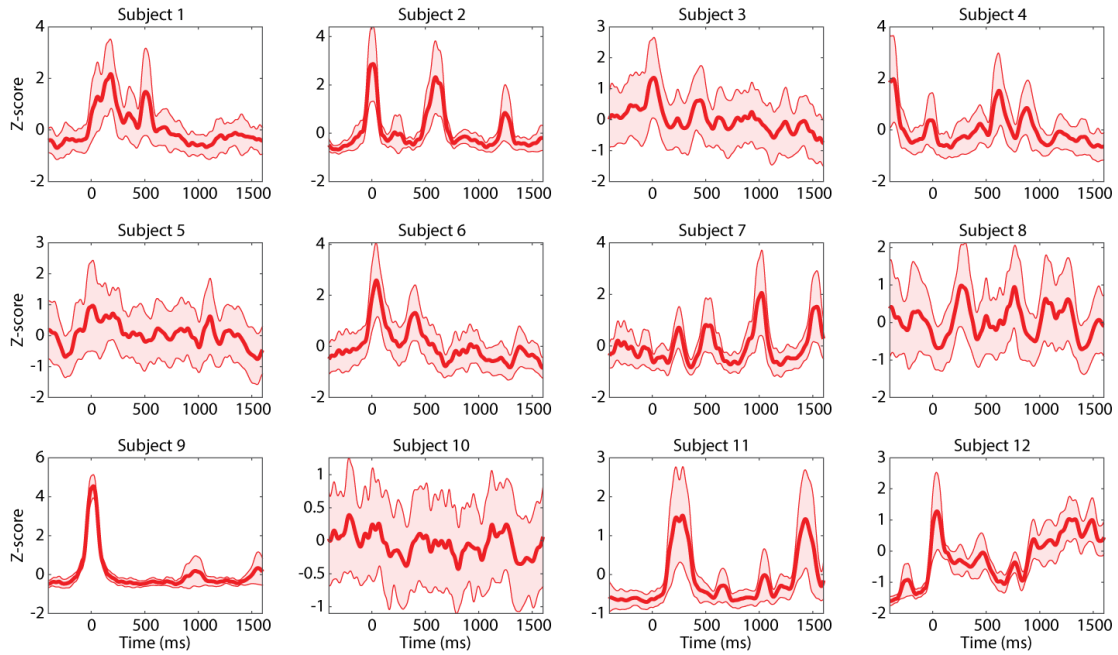


Figure 5.5: RMS gamma power trials in a time window of -400 ms to 1600 ms , where stimuli were applied at 0 ms .

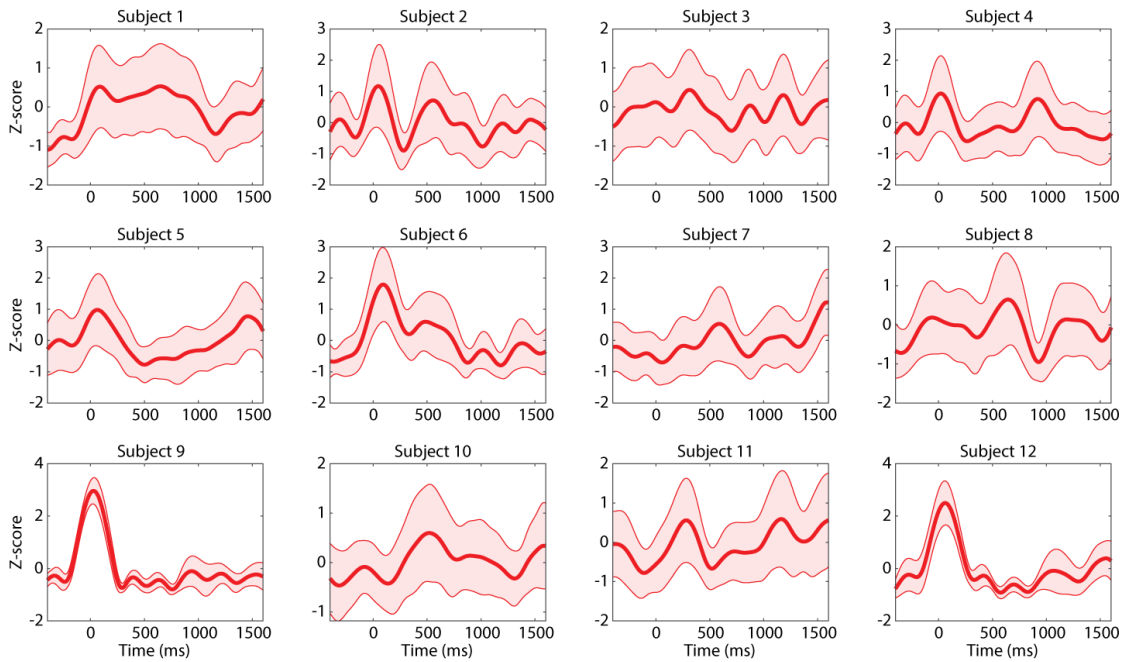


Figure 5.6: RMS theta power in a time window of -400 ms to 1600 ms , where stimuli were applied at 0 ms

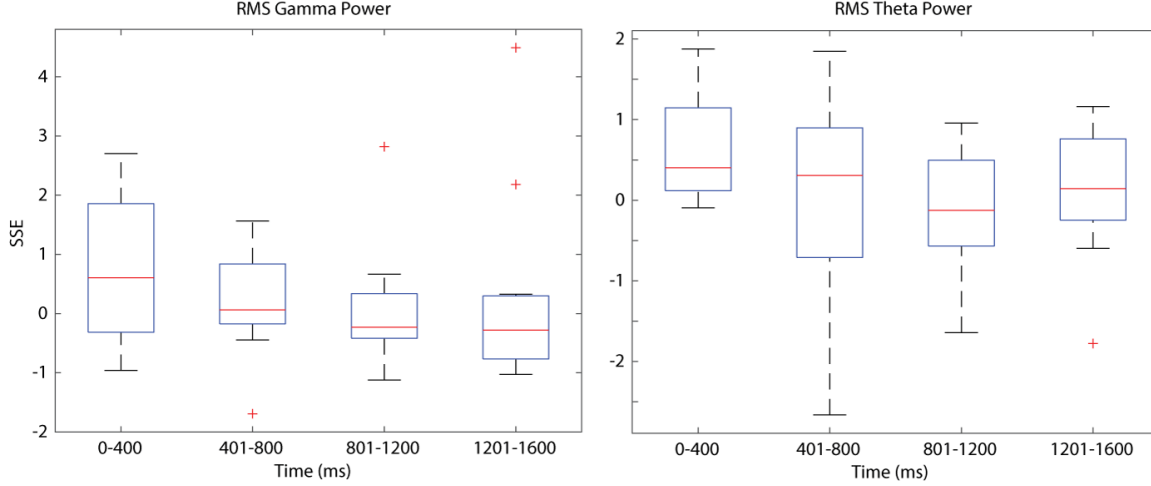


Figure 5.7: Subsequent simulation effects (SSE) across subjects in four time windows for the theta and gamma bands.

5.3.2. NARXNN Plant Outperformed LSSM Plant

Across 12 subjects, we found that both NARXNN and LSSM models accurately predicted the input-driven dynamics of the hippocampal theta and gamma oscillatory activities in response to stimulation. In our initial work, we tested model orders from $p = 1$ to $p = 50$ for both LSSM and NARXNN (for both input and output delays) then selected $p = 8$ for both LSSM and NARXNN (with 10 artificial neurons in the hidden layer) by trading-off the prediction error and computational complexity, empirically. With this model architecture, both LSSM and NARXNN were trained and optimized over 1000 epochs. Because of the subject-specific power levels in different frequencies, we used normalized mean squared error (NMSE) as our quality metric for evaluating model performance. NMSE is given by $NMSE = \sqrt{\epsilon_{pred}^* / \|d - \mu_d\|}$ as discussed in Equation 4.11 and 4.12. In the process of system identification, the one-step-ahead prediction is a commonly-used approach to validate an identified model of a stochastic dynamic system (Gershenfeld and Weigend, 1993), where the next output $\hat{y}(t+1)$ is predicted by the estimator. We the first employed one-step-ahead prediction, where the predictor estimates the next output given the knowledge of current

and previous **input and output** (i.e. $\hat{y}(t+1)$ is predicted by $u(t), u(t-1), \dots, u(t-d_u)$ and $y(t), y(t-1), \dots, y(t-d_u)$). The NMSE of such a prediction approximately resembles the normalized residual in the optimization process (least-squared solution for LSSM and Levenberg-Marquardt solution for NARXNN in fitting the model). For both LSSM and NARXNN models, predicted instantaneous theta and gamma RMS power closely matched the experimental trials, as expected. Figure 5.8 shows an example trace of predicted instantaneous theta and gamma RMS power via LSSM and NARXNN, where we also compared prediction error $y(t) - \hat{y}(t)$ and the power spectral density (PSD) of the predictions versus the experimental data. The overall performance for subject-specific NARXNN versus LSSM in one-step ahead prediction is shown in Figure 5.9. Across all subjects, the averaged NMSE of NARXNN predictions was 0.0348 ± 0.004 for the gamma power and 0.0379 ± 0.007 for the theta power, and the averaged NMSE of LSSM predictions was 0.0384 ± 0.004 for the gamma power and 0.0417 ± 0.006 for theta power.

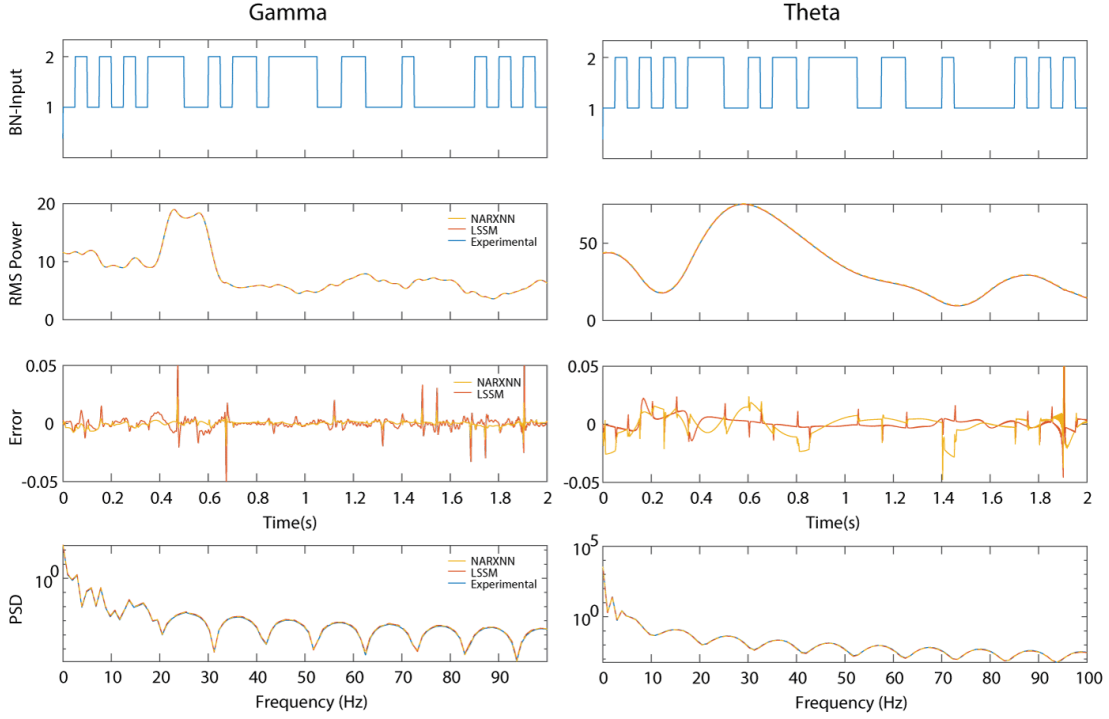


Figure 5.8: Example trace of one-step-ahead predicted instantaneous theta and gamma RMS power via LSSM and NARXNN. $Error = y(t) - \hat{y}(t)$.

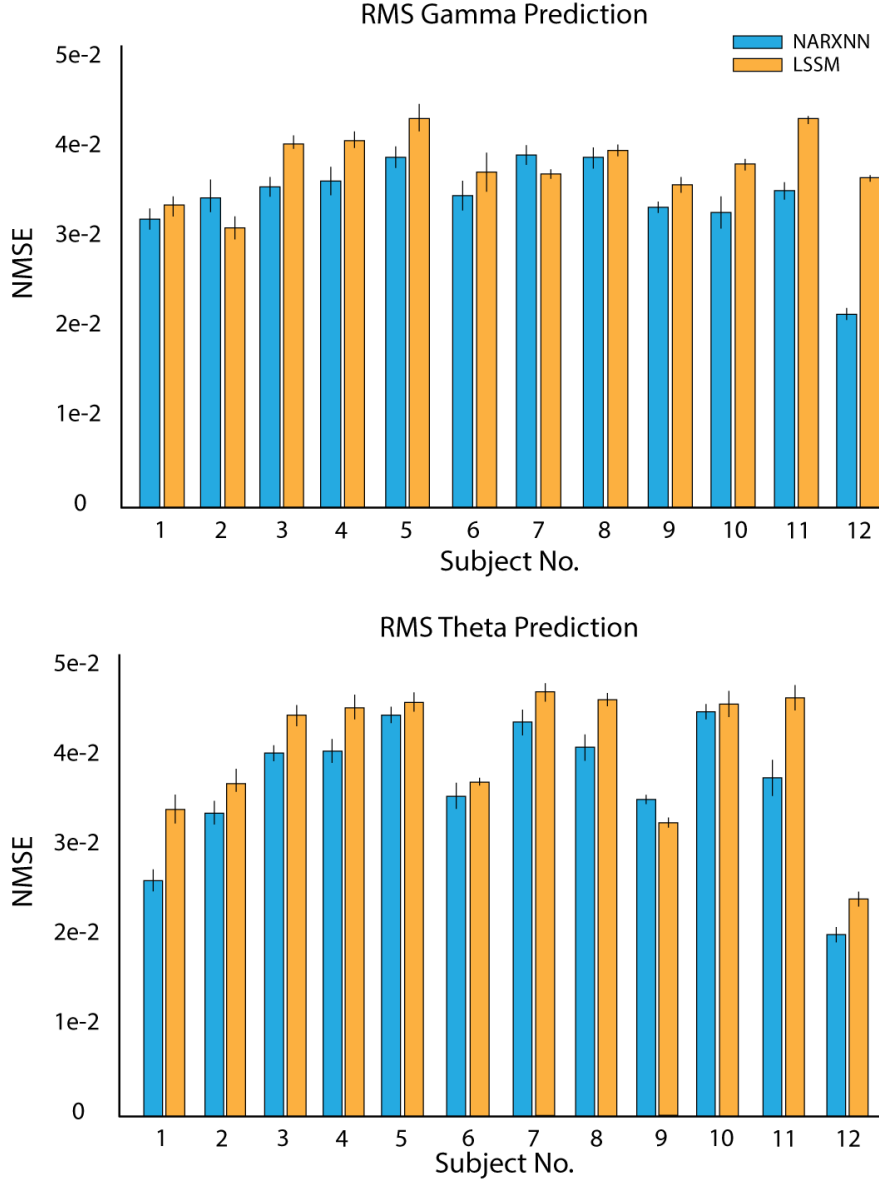


Figure 5.9: Averaged Normalized mean squared error in one-step-ahead prediction of RMS gamma (left) and theta (right) power via NARXNN and LSSM.

Next, we implemented full input-driven prediction in both models. Note that the plant models are now "simulators" (simulation focused) instead of "predictors" (prediction focused). A simulator is the structure in which the model only uses input $u(t), \dots, u(t - d_u)$ and estimated output $\hat{y}(t), \dots, \hat{y}(t - d_y)$ to predict the system output without the knowledge of the experimental output measurements $y(t)$, whereas a predictor is the structure in which

the model utilizes the experimental output measurements. These are also termed "Parallel architecture" and 'Series-Parallel architecture', respectively, in dynamic neural networks (Leontaritis and Billings, 1985; Ljung, 1999; Norgaard et al., 2000). To avoid ambiguity, we used the term 'full input-driven prediction' to distinguish this from results discussed above, despite the prediction can be achieved by a k-step-ahead predictor (see 'compare' versus 'predict' functions for LSSM and 'opennet' verses 'closednet' for NARXNN in MATLAB for detail). This input-driven prediction represents how a plant responds to a system input and yields input-driven dynamics of the system (Ljung, 1999; Yang, Qiao, et al., 2021). In this full prediction, we found that both models altered their performance.

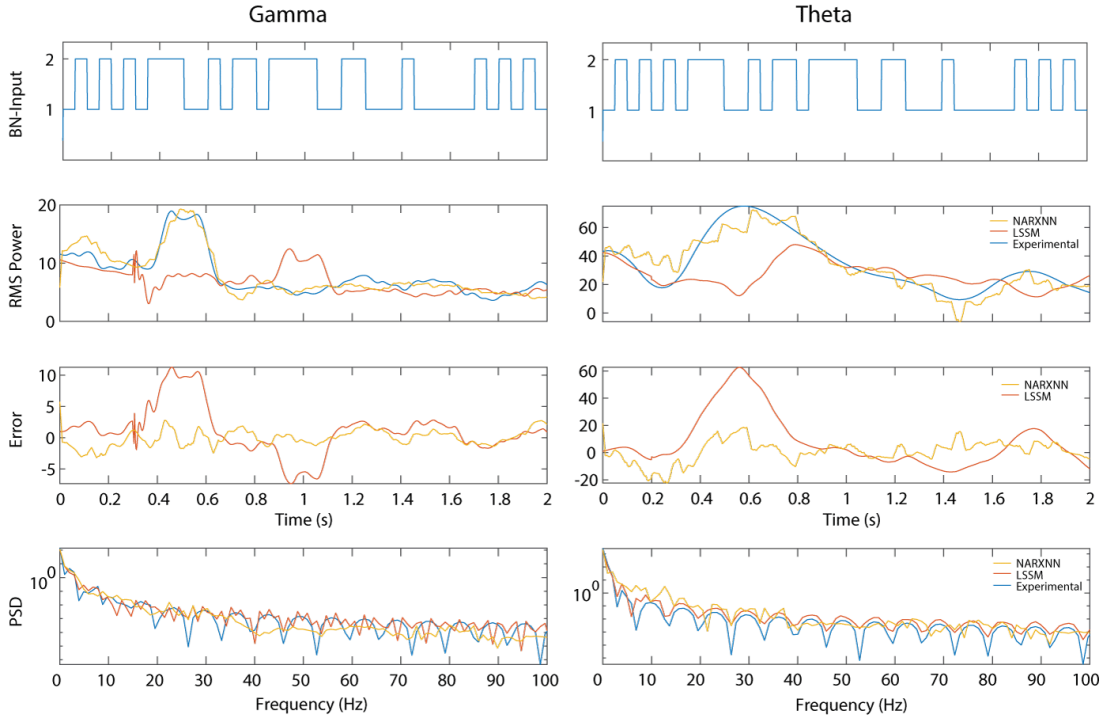


Figure 5.10: Example trace of full input-driven predicted instantaneous theta and gamma RMS power via LSSM and NARXNN. $Error = y(t) - \hat{y}(t)$.

As shown in Figure 5.10, the example trace shows that NARXNN introduced some random fluctuation in predicting gamma and theta power but maintained a fair match to the experimental trial, whereas LSSM lost critical temporal resolutions especially within the 0.3 – 0.8 time window where theta and gamma exhibited great dynamical changes that

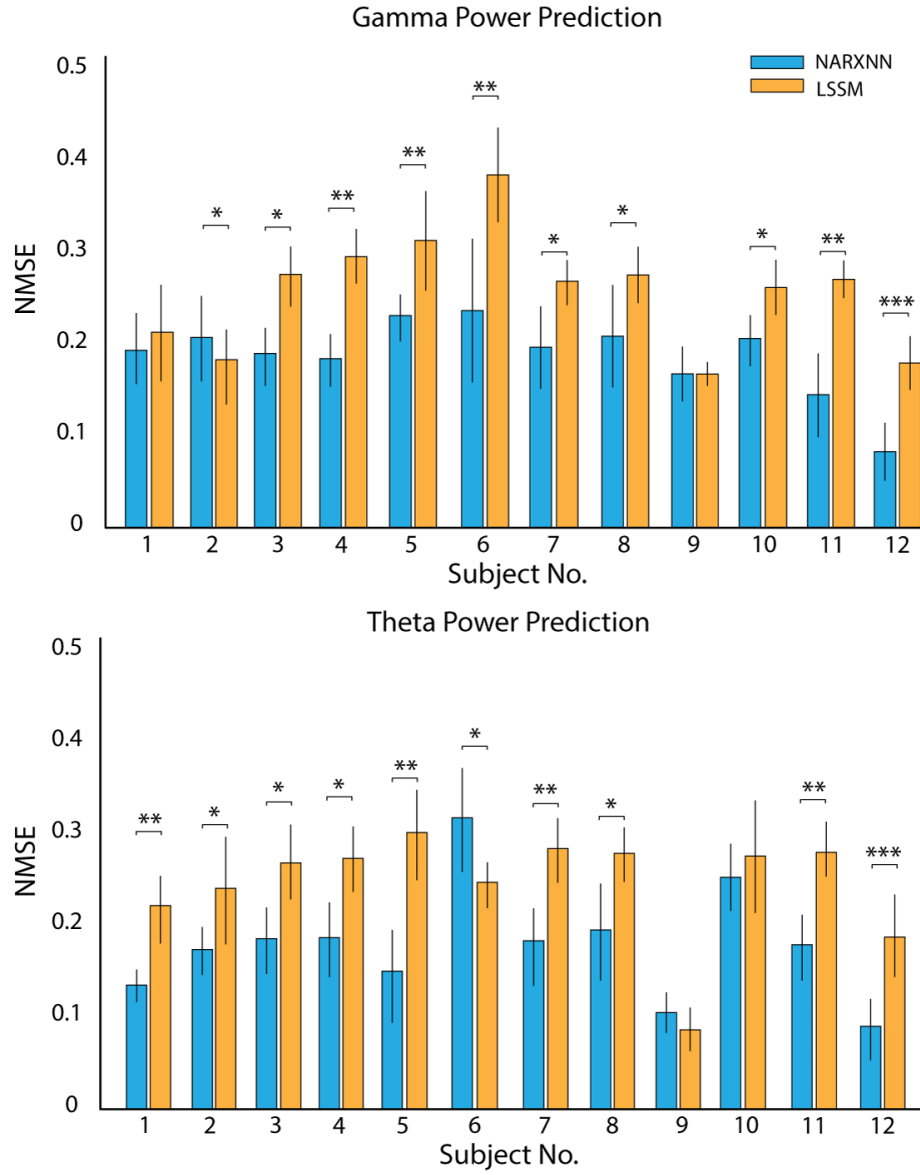


Figure 5.11: Averaged Normalized mean squared error in full input-driven prediction of RMS gamma (left) and theta (right) power via NARXNN and LSSM. *, $p < 0.05$; **, $p < 0.01$; and ***, $p < 0.001$.

LSSM failed to predict accurately. The NMSE of this prediction was 0.190 via NARXNN versus 0.303 via LSSM for the gamma power, and 0.161 via NARXNN versus 0.267 via LSSM for the theta. Across all subjects, the averaged NMSE of predictions via NARXNN was 0.195 ± 0.041 for the gamma power and 0.188 ± 0.062 for the theta, and the averaged NMSE of predictions via LSSM was 0.276 ± 0.079 for the gamma band and 0.251 ± 0.059 for the theta. In 10 out of 12 subjects, gamma band power predicted by NARXNN model exhibited less NMSE comparing to the predictions by LSSM model, and 9 subjects of them had significant less NMSE via paired t-tests ($p < 0.05$). For theta power prediction, 10 subjects had less NMSE using NARXNN than using LSSM and 9 of them were statistically significant (see Figure 5.11).

5.3.3. NARXNN-PID Architecture Is Superior In Modulating Oscillatory Power

We created a simulated testbed for the proposed BCI sytem in Simulink environment then conducted closed-loop control using our NARXNN plant, paired with tuned PID controllers (NARXNN-PID) for testing the effectiveness and efficiency in modulating hippocampal theta and gamma power. The PID controller for each subject-specific NARXNN plant was manually tuned by following the Ziegler-Nichols' method, independently. Then, a subject-specific setpoint (i.e. desired target power level) for each theta and gamma oscillations was determined by the highest power level the NARXNN-PID was able to achieve while maintaining the control signal (i.e stimulation amplitude) in a psychological safe range of $0 - 9 \text{ mA}$ (see Chapter 3, MacDonald, 2002, and R. J. Coffey, 2009). Then, the closed-loop control took place over a course of 2 s , where closed-loop stimulation was onset at $t = 0$, for 76.6 ± 18.8 independent simulations (the same number as experimental trials) across 12 subjects. In comparison, open-loop stimulation was also simulated using the experimental BN input. Example trials of closed-loop control versus open-loop control are found in Figure 5.12, where closed-loop control of gamma power was $87.3\% \pm 12.6\%$ greater than open-loop

power, and closed-loop control of theta power was $56.7\% \pm 13.3\%$ greater, using our NARXX-PID framework. This was calculated on averaged theta/gamma power across the entire 2 s of simulation. Beside, the averaged time to achieve setpoint using closed-loop NARXNN-PID was $413.63 \text{ ms} \pm 211.32 \text{ ms}$ for the gamma power and $186.36 \text{ ms} \pm 59.23 \text{ ms}$ for the theta.

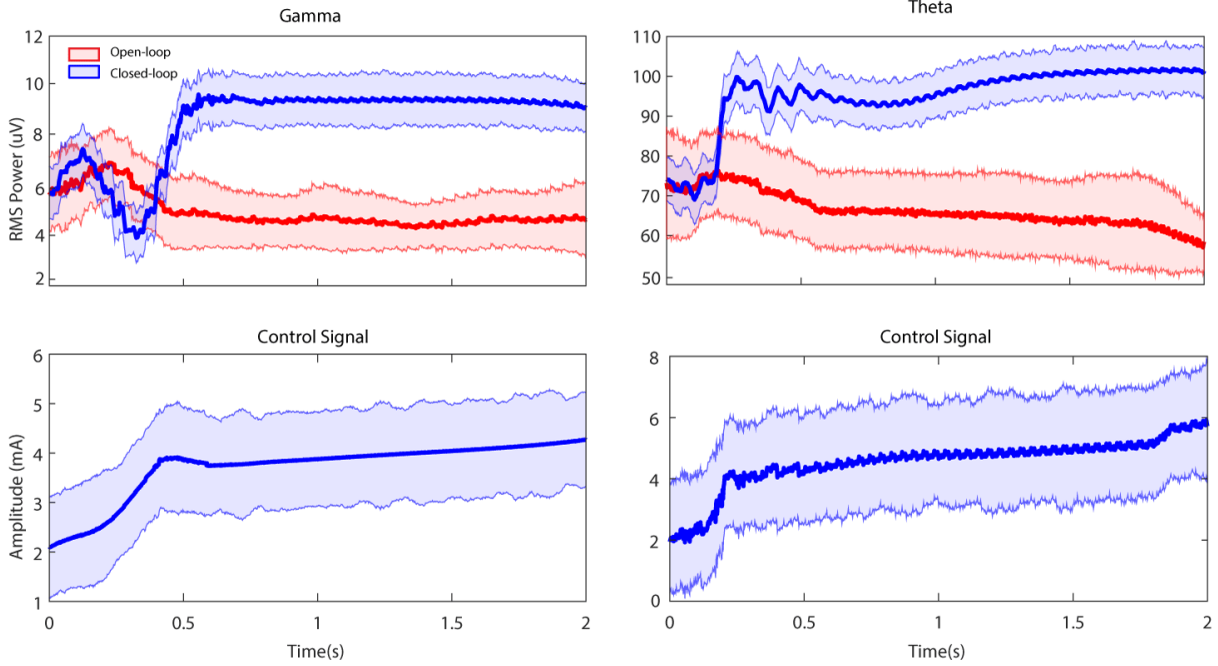


Figure 5.12: Example power trials from closed-loop control versus open-loop control using NARXNN-PID architecture.

In comparison, we constructed a LSSM-PID closed-loop control architecture, where PID controller was tuned by the same approach automatically using the MATLAB Control System Toolbox. We found this LSSM-PID scheme was able to reach a target level but the control signals were saturated at safety boundary and were not as physiologically realistic as the NARXNN-PID architecture, which gradually increased the stimulation amplitude to compensate the intrinsic descent hippocampal power to maintain the desired level (see control signals in Figure 5.12). By selecting a proper setpoint for each subject, we compared the closed-loop control performance for both NARXNN-PID and LSSM-PID frameworks. Here, we computed the averaged RMS power increases across time via closed-loop control versus

experimental power (power increase = $(\bar{P}_{CL} - \bar{P}_{Exp})/\bar{P}_{Exp} \times 100\%$) for each subject using two systems, and we found the capability of both systems in modulating and controlling oscillatory power and confirmed the superior performance using the NARXNN-PID architecture. In all 12 subjects, closed-loop control using the NARXNN-PID exhibited greater gamma power increases versus LSSM-PID under the same safety guideline, and 9 of them were statistically significant ($p < 0.05$). The averaged gamma power increase in the closed-loop control using the NARXNN-PID was $86.25\% \pm 12.3\%$ versus $64.38\% \pm 11.83\%$ using the LSSM-PID. For the theta power, we found that 9 out of 12 subjects had greater power increases using the NARXNN-PID than LSSM-PID (6 were significant, $p < 0.05$) and 2 out of 3 subjects who experienced greater theta power increases using LSSM-PID were significant. The averaged theta power increase in closed-loop control, comparing to the experimental power, was $45.9\% \pm 6.57\%$ using NARXNN-PID versus $40.64\% \pm 6.21\%$ via LSSM-PID. These results are visible in Figure 5.13.

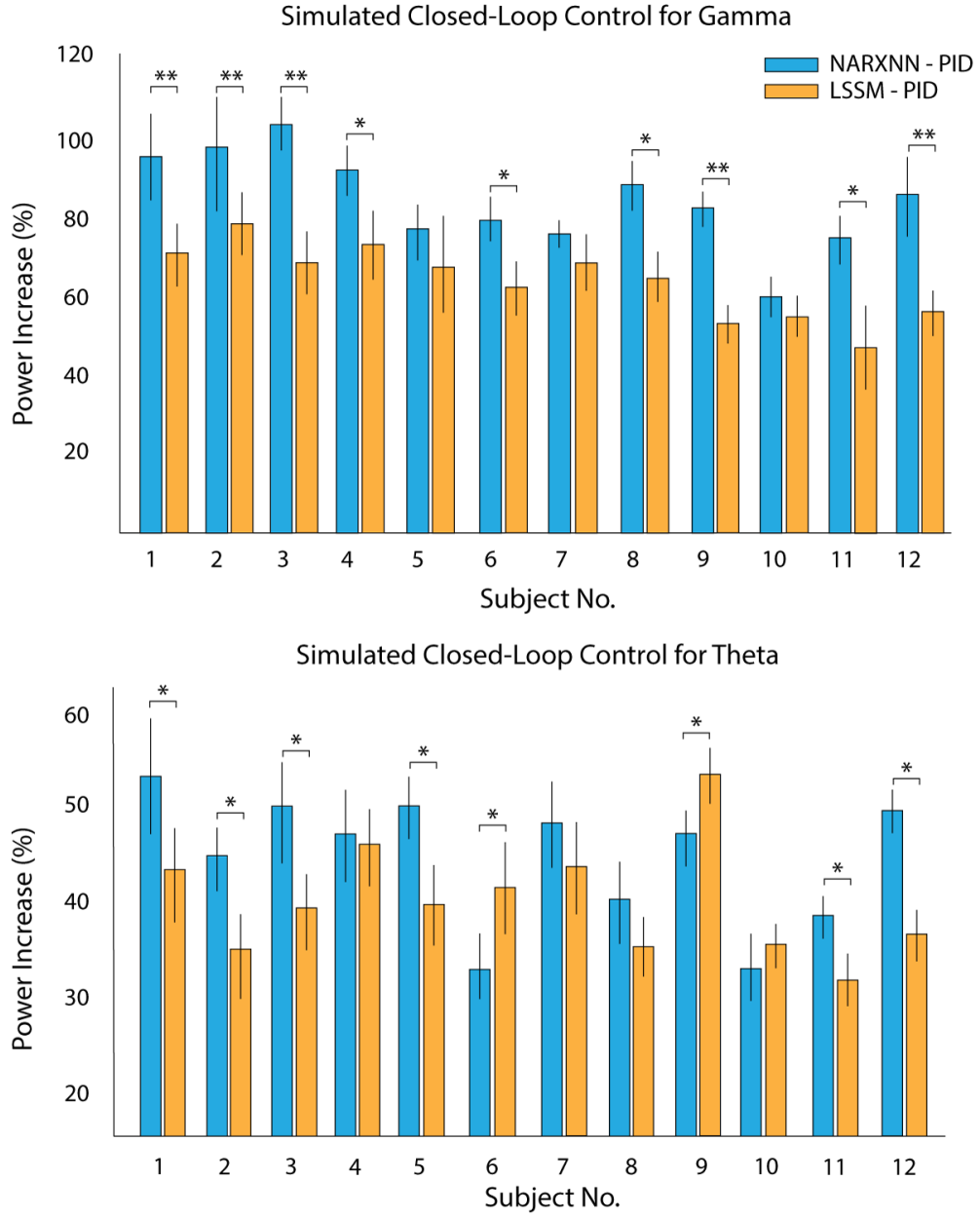


Figure 5.13: Power increases in simulated closed-loop control of hippocampal theta and gamma power using NARXNN-PID versus LSSM-PID. Power increase $= (\bar{P}_{CL} - \bar{P}_{Exp}) / \bar{P}_{Exp} \times 100\%$

5.4. Discussion

We proposed a dynamic model-based brain-computer interface system for modulating hippocampal oscillatory activities, namely, the theta and gamma power, from collected data of open-loop BN-DBS targeting the PCC with observed stimuli-evoked responses in the hippocampus. The theta and gamma rhythms have well-established functional roles in the formation of new memories (Herweg et al., 2020; Shirvalkar et al., 2010; Lin, Rugg, et al., 2017; B. C. Lega, Jacobs, et al., 2012; Lin, Umbach, et al., 2019; J. Miller et al., 2018; Lisman and Jensen, 2013; Åström et al., 2006; Osipova et al., 2006). Thus, the ultimate goal of our proposed BCI system is to restore memory functions and improve memory performance in humans. The choice of the PCC as our DBS targeting site was a consideration on its empirical DBS effects and neurological pathway to the hippocampus. Natu et al. has demonstrated that DBS targeting the PCC brings predicable effects on hippocampal activities in the theta and gamma frequencies (Natu et al., 2019), and the PCC-hippocampal connectivity is critical in predicting memory encoding (B. Lega, Germi, et al., 2017; Wang, Schmitt, et al., 2021). We narrowed down the gamma frequency range to the 30 – 50 Hz low gamma band, which exhibited most stimulation effects, among the rest of gamma frequencies. Besides, processing this frequency band eliminates any line-noise and stimulation artifact leakages via a simple bandpass filter. Because theta oscillatory activities in human exhibit great subject-specific diversity across the 2 – 10 Hz spectra, we selected the 5 – 9 Hz fast theta band (Lin, Rugg, et al., 2017). Our open-loop BN stimulation suggests a diverse power increase in the gamma band within first 400 ms and the theta band within 400 – 800 ms after the onset of stimulation across subjects and the gamma power descended consistently for the rest of stimulation period (Figure 5.7). These stimuli-evoked hippocampal responses not only match Natu et al.’s investigation using the free recall stimulation paradigm but also yield critical temporal information that theta band exhibited a suppressed effect within a particular time span (e.g. 400 – 800 ms). Such a ramping waveform of oscillations has been also demonstrated in both rodents and humans, and this may be beneficial for testing episode

boundaries in the representation of temporal context (Tsao et al., 2018; Umbach et al., 2020; Sols et al., 2017). Although our proposed BCI system is promising for delivering a precise control of DBS amplitude targeting hippocampal dynamical changes, it remains to be shown that this system can improve memory performance across a large number of subjects. For this, we are intended to incorporate a more versatile stimulation paradigm with behavioral memory tasks (e.g. Free-recall tasks) and multiple-noise DBS (i.e. a boarder range of stimulation amplitude and frequencies) due to the individual tolerance and sensitivity to electrical stimulation, in our subsequent experimentation.

We developed our plant models, as the skeleton of the BCI system, on BN stimulation I/O data across 12 participants. We selectively investigated both linear and nonlinear modeling approaches and we were willful to compare the performance across the two. Although a linear ARX model (as examined and discussed in Chapter 4) or a generic polynomial model can be converted into state-space form easily, they are specialized cases of linear state space modeling. So, we followed the more generalized technique that Yang, Connolly, et al.; Shanechi reported in recent studies, where the performance of LSSM demonstrated great potential in modeling such highly nonlinear I/O dynamics (Yang, Connolly, et al., 2018; Yang, Qiao, et al., 2021), and used this LSSM as a benchmark for comparing linear and nonlinear approaches. We preferably chose NARXNN model after our initial investigation of nonlinear modeling using a neural mass model, which exhibited fair accuracy but dramatically less computational efficiency (hours to days via NMM versus tens of minutes via NARXNN in optimizing) and less ability to alter the structure (I. Basu et al., 2018; Jansen and Rit, 1995). Our NARXNN model was able to characterize the stimulation-evoked hippocampal oscillatory activity more accurately especially in the full multi-step-ahead prediction. Such architecture can work as a true physiological plant in the "Parallel" form once identified for forward prediction of the stimuli-driven hippocampal dynamics based on inputs and without further knowledge of past and current measurement. Our use of temporal-wise attention data segmenting technique, inspired by modern CV and NLP tasks, boosted the perfor-

mance of a traditional SISO NARXNN model. This TA approach essentially converted a feature (i.e. instantaneous power at a time point) into a feature of temporal relevant vector for optimizing, and its unparalleled accuracy justified the computational burden. Arguably, this would increase the system latency for a real-time BCI implementation and make the structure into multi-rate system. Thereby, we selected a TA window of 20 (40 samples) to minimize the computational concerns in both system identification and real-time feedback, and used a signal buffer for solving the multi-rate problem, which has been also implemented in real-time BCI applications (Zelmann et al., 2020). Further, the Bayesian regularization optimization demonstrated its robustness, which does not require dedicated validation procedure to prevent over-fitting issues (Foresee and Hagan, 1997; MacKay, 1992), favoring our limited number of subject-specific trials for training a complex nonlinear network.

Reportedly, Yang et al. stated an impaired performance using a wavelet-based nonlinear ARX plant, comparing to an LSSM, and raised a concern about the necessity of using a nonlinear plant. This might due to the fact that the network architecture of their choice was not quite ideal for their desired biomarker (a combination of multiple brain oscillations, representing brain network) and/or for the temporal scale (over 100 s). In our investigation, a NARXNN with proper optimization and data manipulation (e.g. TA technique) would not require a sophisticated architecture (i.e. high model numbers and numerous neurons) for a decent performance, which is intended to converge to a boundary that expanding the model structure does not increase accuracy any drastically. Thus, we believe the superior performance of our implementation of the NARXNN architecture with TA batching and Bayesian regularization facilitated concerns regarding modeling neurological activities using a neural network, or a nonlinear model in general. Moreover, the performance gap in between the NARXNN and LSSM with the same model order may demonstrate the anticipated nonlinearity in the causal relationship how hippocampal oscillations respond to external stimuli to the PCC, and this is more physiologically realistic. Note that a static or feed-forward network might not be ideal for predicting dynamic I/O relationship. But, a dynamic net-

work that depends on the past and current I/O, representing the neurological processing of temporal context, may be very favorable for demodulating of memory-relevant activities. Certainly, using a nonlinear plant in modeling neural signals brings drawbacks in implementation. One limitation of neural networks lies in strict specificity to a brain region or patient. By virtue of how the system parameters are identified in nonlinear models (by empirically fitting system parameters to qualitatively match collected patient neural data via trial-and-error Santaniello et al., 2015; Sritharan and S. V. Sarma, 2014), nonlinear systems hinder the ability to design powerful real-time closed-loop controllers that can be easily generalized across the broad of users (Rosenblum and Pikovsky, 2004). Nonetheless, we are thrilled to witness the booming commercial market of BCI products targeting therapeutic neuromodulation utilize more advanced nonlinear approaches based on machine learning techniques with accesses of big data (Musk et al., 2019; Oxley, Opie, et al., 2016; Oxley, Yoo, et al., 2021; Skarpaas et al., 2019).

In addition, we sought to clarify that both of our LSSM and NARXNN modeling were input-driven (fitted using I/O data during BN stimulation) to capture the stimuli-evoked activity in the hippocampus, which in return might be inadequate for representing the resting-state hippocampal activity when DBS is absent. The development of a comprehensive neural model (linear or nonlinear) that accounts for both stimulation evoked response and intrinsic neural activity remains an activity area of study for neuromodulation and understanding the brain circuitry. One critical questions is “what would the system output be if there was no input (stimulation)”. Ideally, the brain model should be able to duplicate the resting-state electrophysiological activity. However, this is very challenging to accurately reproduce because the resting-state EEG during no-stimulation remains unknown evoked response (e.g. from subject’s movement, thinking, visual and auditory discretion, etc.). To simply this question, one direction is to solely focus on stimulation evoked response. For instance, I. Basu et al.’s neural mass model was only targeting the stimuli-evoked changes of P300 waves in local field potentials across several frequency bands ($10 - 160$ Hz) and the model was fitted

during stimulation. This input-driven modeling has been adopted for a variety of studies on closed-loop DBS and has proven effective and safe for human and non-human subjects (I. Basu et al., 2018; Price and Togneri, 2012; R. Anderson et al., 2020; Bouthour et al., 2019; Miranda et al., 2015; Tsuda et al., 2014). Thus, we kept our focus on the stimulus-evoked hippocampal theta and gamma oscillatory power, rather than a full blueprint of the hippocampus. Furthermore, our use of the BN stimulation facilitated the immediate needs of modeling resting-state oscillatory power (when stimulation is absent). This is because the BN pattern, as discussed in Section 3.4, represents a comprehensive testing signal due to its white spectrum for identifying a system, which essentially derives the impulse response of the hippocampal theta and gamma power as the measure of how RMS power changes from the resting-state (the DC level) (Møller, 1986; Ljung, 2007; H. Tulleken, 1988; H. J. Tulleken, 1990). For this reason, the BN stimulation/testing signal with input-driven modeling has been implemented and recommended for numerous complex industrial control applications (Greiser et al., 2015; Franck and Rake, 1985; Van den Bos, 1967; Miao et al., 2005; I. Henderson and McGhee, 1989; Monmasson et al., 2011). Certainly, neural activity is drastically different from machinery and we would like to bridge the gap in between a precise control of our biomarkers and the sophisticated intrinsic brain states. Thus, our future work will incorporate noise and disturbances into the NARXNN and this will allow us to model the resting-state hippocampal gamma and theta oscillatory power.

We also tested the proposed BCI system in a simulated environment (Simulink) for evaluating of closed-loop design and we currently plan on in vivo testing in our further work. In our design of closed-loop control, we implemented the tried-and-true powerful PID controllers for both LSSM and NARXNN plants. This was because we focused on developing a robust plant model for the subsequent closed-loop control and sought to compare the model performance across linear and nonlinear approaches. The PID controller provide an opportunity for this task due to its independence to the plant model. Moreover, the ease of tuning such a controller makes it a great candidate for testing our plants. As mentioned in Section 5.2.6,

we followed the Ziegler-Nichols’ method in tuning proportional, integral, and derivative gains for both plants. As a result, our PID controller was proved capable of reaching a specific setpoint in a clinically-relevant time scale and staying within stimulation safety guidelines of 9 mA of stimulation amplitude, across all 12 subjects. For both theta and gamma oscillatory power, we noticed that the NARXNN-PID architecture was more capable of maintaining the target power level against the intrinsic neurological decay of stimuli-evoked hippocampal power by gradually increasing the stimulation amplitude over the course of closed-loop control (see Figure 5.13). We believe this was more physiological realistic in resembling the intrinsic dynamics (shown in the experimental data, see Figure 5.5 and 5.7) and the control signal $u(t)$ had much lower amplitudes, compared to LSSM-PID scheme. Given the safety guideline, the NARXNN-PID architecture was also capable of reaching a greater target level of theta and gamma power within a similar time scale as the LSSM-PID. For the gamma band, NARXNN-PID demonstrated the unparalleled performance in modulating power level. However, we found both NARXNN-PID and LSSM-PID struggled in achieving a greater target theta power level. The drastically diverse theta power across subjects, especially within $400 - 800\text{ ms}$, might suppress the overall controllability. With a realistic target level, we were able to achieve power increases in theta using both close-loop control designs in all 12 subjects (11 were statically significant, $p < 0.05$) comparing to the experimental power level, and 9 out of 12 subjects (6 were significant, $p < 0.05$) exhibited greater theta power increases via NARXNN-PID than LSSM-PID. Nonetheless, both closed-loop control schemes showed successful neuromodulation of hippocampal theta power, although they remain exploratory for modulating theta oscillations as a means of memory restoration. We would like to emphasize that simply increasing or decreasing hippocampal theta power might not be sufficient for enhancing memory encoding as it is a much more diverse oscillatory activity and reports have shown theta power decreases during memory encoding (Natu et al., 2019; Klimesch, 1999; Herweg et al., 2020; B. C. Lega, Jacobs, et al., 2012). This may require more deliberate investigation of stimuli-evoked hippocampal theta dynamics in specific temporal frameworks

for improving memory performance. More importantly, our BCI system exhibits a distinct role in studying human memory generally, apart from the goal of enhancing encoding success. Namely, if a specific hippocampal pattern is linked to a feature of episodic memory behavior such as temporal clustering (Griffiths et al., 2019; Manning et al., 2011), then our proposed system provides a mechanism to test how manipulation of this pattern impacts behavior. This may allow human investigations to achieve the sort of specific interventions available to rodents using methods such as optogenetics (Robinson et al., 2016).

To sum up, the proposed closed-loop BCI system takes advantage of dynamic I/O information in the representation of memory-relevant hippocampal biomarkers, resulting in a rich temporal resolution in neuromodulation comparing to other closed-loop systems based on machine learning classifiers and empirical thresholds (Ezzyat et al., 2018; Zelmann et al., 2020). Besides, the NARXNN approach would permit predictions regarding the impact of stimulation across a number of frequency ranges, which in turn would allow us to determine in our framework how stimulation would impact aggregate features that could be used to predict encoding success. Therefore, with proven capability of neuromodulation of our BCI system, modulating memory-relevant hippocampal activities remains an active area of our subsequent investigation. Adjustment of PCC-applied BN stimulation parameters (e.g. number of amplitudes and frequencies) with integration of memory tasks may be an effective approach in testing the BCI system. Given our initial implementation of real-time BCI system, a feasible solution is to acquire a session of open-loop BN stimulation data while participants performing free-recall tasks, where stimulation is applied to the PCC on a list basis (as described in Chapter 3 for FR-stim paradigm), followed by a process of model training then a closed-loop stimulation session with free-recall tasks. This protocol and procedure would take up to 2 hours on the same day during the patients' stay and minimizes the effects of change of brain states and subjects' moods. Improving the architecture and generalizability can be another future work aspect of our design. This may be achieved by a combination of stimuli-evoked hippocampal activities fitting to the NARXNN in a deep

learning framework, or to a more physiologically realistic nonlinear model such as a NMM with groups of neurons. Also, tuning a PID controller might not result in an optimal control even if by following well-established tuning methods, which may in return hinder overall closed-loop control performance. For this reason, a controller with an optimization procedure dedicated to nonlinear dynamics such as a model predictive controller (MPC) may be favorable for this task.

5.5. Conclusion and Significance

Closed-loop neuromodulation of stimuli-evoked hippocampal oscillatory activity in the theta and gamma frequencies would impact the emerging field of therapeutic brain computer interfaces targeting memory restoration. Our experimental data suggests that deep brain stimulation applied to the posterior cingulate cortex may be a fruitful strategy for restoring memory-relevant hippocampal functions, and our binary-noise stimulation paradigm may be an ideal scheme for investigating how DBS parameters affect behavioral functions and for obtaining open-loop data for development of dynamic BCI systems. Compared to a benchmark system based on linear state-space modeling, our choice of NARXNN with modern machine learning techniques provides unparalleled performance in identifying a model that describes nonlinear I/O dynamics between PCC-applied stimulation and hippocampal neural activities, and our NARXNN-PID closed-loop BCI architecture has demonstrated the capability of modulating our biomarkers for memory with exceptional temporal resolutions and clinical safety. We believe our proposed BCI system offers a promising approach for the neuromodulation of memory, and eventually, for restoring memory functions.

APPENDIX A

BN Stimulation Troubleshooting Procedure

Stimulation artifact leakage: excessive high frequency artifacts in LB/LC channels during stimulation. This may indicate:

1. Poor stimulating circuitry: check “dangle” channel 1 and LX1 electrode connection. Their connection should be completely away from the Jackbox. (i.e. once they are connected, no connector should be plugged back in the Jackbox LX1 electrode socket). Same for the LX1’s adjacent channel (LX2), which should be directly connected to the GND on the back of Cerestim.
2. Poor grounding: Make sure the mastoid is connected to the GND on the amplifier and the connection is solid.
3. Improper/no filtering: Make sure LP 250Hz filtering is enabled for Continuous Acquisition.
4. If none of the above procedures helps reduce stimulation artifacts, try enable the referencing using “*BR_stim_10thRef.ccf*” configuration file (under the same folder path) for Central. Tweak the reference electrode if necessary. A bipolar (within the probe) referencing scheme would be helpful (e.g. LB2-LB1, LB3-LB2, \dots , LB1- LB10).

No signal reading: no EEG waveform is shown in the oscilloscope panel or abnormal DC level. This may indicate:

1. Poor cable connection between the N.K. modified cable and the splitter box (a known issue).

2. Poor cable (the blue ribbon cable) connection between the amplifier and the splitter box.
3. EEG signals are filtered out by the line noise cancellation (LNC) algorithm in the Central software for some subjects. Disable LNC in the Central for all channels.

Absence of sync pulses: no sync pulse train in the oscilloscope panel. This may indicate:

1. Stimulation script is not running: make sure MATLAB scripts is running. Scripts stops automatically after preset number of events (default 90 events, 5-15mins depending on event duration).
2. Poor BNC cable connection: make sure the BNC cable has a snug fit on both ends. Swap out with another if necessary. Sync pulses should have a peak amplitude of $4000\ \mu V$ at the beginning of each stimulation event.
3. Note that the oscilloscope is not 100% in real-time so wait a few seconds before any operations. If both channels on the oscilloscope are spotty and looking unusual, switch to another channel then switch back. (This is a known software issue of Central)

Unable to connect Cerestim to PC. Error messages when running *Cerestim_connect.m script*.

1. This often happens when Cerestim was not turned off previously.
2. Turn off the Cerestim by firmly pressing the power button on the front panel of Cerestim (for a few seconds). Then, firmly press the power button again for rebooting. Repeat this a few times if necessary.

BIBLIOGRAPHY

- Agarwal, G. et al. (2014). “Spatially distributed local fields in the hippocampus encode rat position”. In: *Science* 344.6184, pp. 626–630.
- Agnew, W. F. and D. B. McCreery (1990). “Considerations for safety with chronically implanted nerve electrodes”. In: *Epilepsia* 31, S27–S32.
- Anderson, R. et al. (2020). “A novel method for calculating beta band burst durations in Parkinson’s disease using a physiological baseline”. In: *Journal of neuroscience methods* 343, p. 108811.
- Ardalani-Farsa, M. and S. Zolfaghari (2010). “Chaotic time series prediction with residual analysis method using hybrid Elman–NARX neural networks”. In: *Neurocomputing* 73.13-15, pp. 2540–2553.
- Arora, A. et al. (2018). “Comparison of logistic regression, support vector machines, and deep learning classifiers for predicting memory encoding success using human intracranial EEG recordings”. In: *Journal of neural engineering* 15.6, p. 066028.
- Aru, J. et al. (2015). “Untangling cross-frequency coupling in neuroscience”. In: *Current opinion in neurobiology* 31, pp. 51–61.
- Åström, K. J., T. Hägglund, and K. J. Astrom (2006). *Advanced PID control*. Vol. 461. ISA-The Instrumentation, Systems, and Automation Society Research Triangle Park.
- Axmacher, N. et al. (2010). “Cross-frequency coupling supports multi-item working memory in the human hippocampus”. In: *Proceedings of the National Academy of Sciences* 107.7, pp. 3228–3233.

- Bäckman, L., B. J. Small, and L. Fratiglioni (2001). “Stability of the preclinical episodic memory deficit in Alzheimer’s disease”. In: *Brain* 124.1, pp. 96–102.
- Backus, A. R. et al. (2016). “Hippocampal-prefrontal theta oscillations support memory integration”. In: *Current Biology* 26.4, pp. 450–457.
- Baddeley, A. D. and E. K. Warrington (1970). “Amnesia and the distinction between long-and short-term memory”. In: *Journal of verbal learning and verbal behavior* 9.2, pp. 176–189.
- Bai, F. et al. (2009). “Abnormal resting-state functional connectivity of posterior cingulate cortex in amnesic type mild cognitive impairment”. In: *Brain research* 1302, pp. 167–174.
- Basu, I. et al. (2018). “A neural mass model to predict electrical stimulation evoked responses in human and non-human primate brain”. In: *Journal of neural engineering* 15.6, p. 066012.
- Basu, J. and S. A. Siegelbaum (2015). “The corticohippocampal circuit, synaptic plasticity, and memory”. In: *Cold Spring Harbor perspectives in biology* 7.11, a021733.
- Benabid, A. L. (2003). “Deep brain stimulation for Parkinson’s disease”. In: *Current opinion in neurobiology* 13.6, pp. 696–706.
- Blanco, S. et al. (1995). “Stationarity of the EEG series”. In: *IEEE Engineering in medicine and biology Magazine* 14.4, pp. 395–399.
- Bouthour, W. et al. (2019). “Biomarkers for closed-loop deep brain stimulation in Parkinson disease and beyond”. In: *Nature Reviews Neurology* 15.6, pp. 343–352.
- Breit, S., J. B. Schulz, and A.-L. Benabid (2004). “Deep brain stimulation”. In: *Cell and tissue research* 318.1, pp. 275–288.
- Bressler, S. L., R. Coppola, and R. Nakamura (1993). “Episodic multiregional cortical coherence at multiple frequencies during visual task performance”. In: *Nature* 366.6451, pp. 153–156.

- Bullock, T. H. and M. C. McClune (1989). “Lateral coherence of the electrocorticogram: a new measure of brain synchrony”. In: *How do Brains Work?* Springer, pp. 375–396.
- Burgess, N., E. A. Maguire, and J. O’Keefe (2002). “The human hippocampus and spatial and episodic memory”. In: *Neuron* 35.4, pp. 625–641.
- Burke, J. F. et al. (2014). “Theta and high-frequency activity mark spontaneous recall of episodic memories”. In: *Journal of Neuroscience* 34.34, pp. 11355–11365.
- Buschman, T. J. et al. (2012). “Synchronous oscillatory neural ensembles for rules in the prefrontal cortex”. In: *Neuron* 76.4, pp. 838–846.
- Butson, C. R. et al. (2007). “Patient-specific analysis of the volume of tissue activated during deep brain stimulation”. In: *Neuroimage* 34.2, pp. 661–670.
- Buzsáki, G. (2002). “Theta oscillations in the hippocampus”. In: *Neuron* 33.3, pp. 325–340.
- Cabeza, R. et al. (2008). “The parietal cortex and episodic memory: an attentional account”. In: *Nature Reviews Neuroscience* 9.8, pp. 613–625.
- Canolty, R. T., E. Edwards, et al. (2006). “High gamma power is phase-locked to theta oscillations in human neocortex”. In: *science* 313.5793, pp. 1626–1628.
- Canolty, R. T. and R. T. Knight (2010). “The functional role of cross-frequency coupling”. In: *Trends in cognitive sciences* 14.11, pp. 506–515.
- Canto, C. B., F. G. Wouterlood, and M. P. Witter (2008). “What does anatomical organization of entorhinal cortex tell us?” In: *Neural plasticity*.
- Chaieb, L. et al. (2015). “Theta-gamma phase-phase coupling during working memory maintenance in the human hippocampus”. In: *Cognitive neuroscience* 6.4, pp. 149–157.
- Chang, J.-Y. et al. (2012). “Multivariate autoregressive models with exogenous inputs for intracerebral responses to direct electrical stimulation of the human brain”. In: *Frontiers in human neuroscience* 6, p. 317.
- Choi, K. et al. (2020). “Longitudinal differences in human hippocampal connectivity during episodic memory processing”. In: *Cerebral cortex communications* 1.1, tgaa010.

- Coffey, R. J. (2009). “Deep brain stimulation devices: a brief technical history and review”. In: *Artificial organs* 33.3, pp. 208–220.
- Cole, S. and B. Voytek (2019). “Cycle-by-cycle analysis of neural oscillations”. In: *Journal of neurophysiology* 122.2, pp. 849–861.
- Colgin, L. L. (2015). “Theta–gamma coupling in the entorhinal–hippocampal system”. In: *Current opinion in neurobiology* 31, pp. 45–50.
- Colgin, L. L. et al. (2009). “Frequency of gamma oscillations routes flow of information in the hippocampus”. In: *Nature* 462.7271, pp. 353–357.
- Coombes, S. and Á. Byrne (2019). “Next generation neural mass models”. In: *Nonlinear dynamics in computational neuroscience*. Springer, pp. 1–16.
- Corripio, I. et al. (2020). “Deep brain stimulation in treatment resistant schizophrenia: a pilot randomized cross-over clinical trial”. In: *EBioMedicine* 51, p. 102568.
- Dan, Y. and M.-M. Poo (2006). “Spike timing-dependent plasticity: from synapse to perception”. In: *Physiological reviews* 86.3, pp. 1033–1048.
- Daunizeau, J. and K. J. Friston (2007). “A mesostate-space model for EEG and MEG”. In: *NeuroImage* 38.1, pp. 67–81.
- Davila, C. E. (2015). “Signal denoising via quadratic semi-infinite programming”. In: *2015 49th Asilomar Conference on Signals, Systems and Computers*. IEEE, pp. 612–616.
- De Hemptinne, C. et al. (2015). “Therapeutic deep brain stimulation reduces cortical phase-amplitude coupling in Parkinson’s disease”. In: *Nature neuroscience* 18.5, pp. 779–786.
- Deshmukh, S. S. et al. (2010). “Theta modulation in the medial and the lateral entorhinal cortices”. In: *Journal of neurophysiology* 104.2, pp. 994–1006.
- Deuschl, G. and Y. Agid (2013). “Subthalamic neurostimulation for Parkinson’s disease with early fluctuations: balancing the risks and benefits”. In: *The Lancet Neurology* 12.10, pp. 1025–1034.

- Deuschl, G., C. Schade-Brittinger, et al. (2006). “A randomized trial of deep-brain stimulation for Parkinson’s disease”. In: *New England Journal of Medicine* 355.9, pp. 896–908.
- Diaconescu, E. (2008). “The use of NARX neural networks to predict chaotic time series”. In: *Wseas Transactions on computer research* 3.3, pp. 182–191.
- Dostrovsky, J. O. and A. M. Lozano (2002). “Mechanisms of deep brain stimulation”. In: *Movement disorders: official journal of the Movement Disorder Society* 17.S3, S63–S68.
- Eichenbaum, H., G. Schoenbaum, et al. (1996). “Functional organization of the hippocampal memory system”. In: *Proceedings of the National Academy of Sciences* 93.24, pp. 13500–13507.
- Eichenbaum, H., A. P. Yonelinas, and C. Ranganath (2007). “The medial temporal lobe and recognition memory”. In: *Annu. Rev. Neurosci.* 30, pp. 123–152.
- Ekstrom, A. D. (2021). “Regional variation in neurovascular coupling and why we still lack a Rosetta Stone”. In: *Philosophical Transactions of the Royal Society B* 376.1815, p. 20190634.
- Ekstrom, A. D. et al. (2005). “Human hippocampal theta activity during virtual navigation”. In: *Hippocampus* 15.7, pp. 881–889.
- Elger, C. et al. (2000). “Nonlinear EEG analysis and its potential role in epileptology”. In: *Epilepsia* 41, S34–S38.
- Eykhoff, P. et al. (1974). *System identification*. Vol. 14. Wiley London.
- Ezzyat, Y. et al. (2018). “Closed-loop stimulation of temporal cortex rescues functional networks and improves memory”. In: *Nature communications* 9.1, pp. 1–8.
- Feldman, D. E. (2012). “The spike-timing dependence of plasticity”. In: *Neuron* 75.4, pp. 556–571.
- Fell, J. et al. (2011). “Medial temporal theta/alpha power enhancement precedes successful memory encoding: evidence based on intracranial EEG”. In: *Journal of Neuroscience* 31.14, pp. 5392–5397.

- Fisher, R. et al. (2010). “Electrical stimulation of the anterior nucleus of thalamus for treatment of refractory epilepsy”. In: *Epilepsia* 51.5, pp. 899–908.
- Fletcher, P., T. Shallice, and R. J. Dolan (1998). “The functional roles of prefrontal cortex in episodic memory. I. Encoding.” In: *Brain: a journal of neurology* 121.7, pp. 1239–1248.
- Foresee, F. D. and M. T. Hagan (1997). “Gauss-Newton approximation to Bayesian learning”. In: *Proceedings of international conference on neural networks (ICNN’97)*. Vol. 3. IEEE, pp. 1930–1935.
- Foster, B. L. and J. Parvizi (2012). “Resting oscillations and cross-frequency coupling in the human posteromedial cortex”. In: *Neuroimage* 60.1, pp. 384–391.
- Franck, G. and H. Rake (1985). “Identification of a large water-heated crossflow heat exchanger with binary multifrequency signals”. In: *IFAC Proceedings Volumes* 18.5, pp. 1859–1864.
- Fries, P. (2005). “A mechanism for cognitive dynamics: neuronal communication through neuronal coherence”. In: *Trends in cognitive sciences* 9.10, pp. 474–480.
- (2009). “Neuronal gamma-band synchronization as a fundamental process in cortical computation”. In: *Annual review of neuroscience* 32, pp. 209–224.
- Friston, K. et al. (1997). “Psychophysiological and modulatory interactions in neuroimaging”. In: *Neuroimage* 6.3, pp. 218–229.
- Furtak, S. C. et al. (2007). “Functional neuroanatomy of the parahippocampal region in the rat: the perirhinal and postrhinal cortices”. In: *Hippocampus* 17.9, pp. 709–722.
- Galassi, A., M. Lippi, and P. Torroni (2020). “Attention in natural language processing”. In: *IEEE Transactions on Neural Networks and Learning Systems* 32.10, pp. 4291–4308.
- Gatt, A. and E. Krahmer (2018). “Survey of the state of the art in natural language generation: Core tasks, applications and evaluation”. In: *Journal of Artificial Intelligence Research* 61, pp. 65–170.

- Gershenfeld, N. A. and A. S. Weigend (1993). *The future of time series*. Xerox Corporation, Palo Alto Research Center Palo Alto, CA, USA.
- Gillund, G. (2012). “Episodic Memory”. In: *Encyclopedia of Human Behavior (Second Edition)*. Ed. by V. Ramachandran. Second Edition. San Diego: Academic Press, pp. 68–72. URL: <https://www.sciencedirect.com/science/article/pii/B978012375000600152X>.
- Glanzer, M. and A. R. Cunitz (1966). “Two storage mechanisms in free recall”. In: *Journal of verbal learning and verbal behavior* 5.4, pp. 351–360.
- Golub, G. H. and C. F. Van Loan (1996). *Matrix Computations*. Third. The Johns Hopkins University Press.
- Gordon, B. et al. (1990). “Parameters for direct cortical electrical stimulation in the human: histopathologic confirmation”. In: *Electroencephalography and clinical neurophysiology* 75.5, pp. 371–377.
- Goyal, A. et al. (2020). “Functionally distinct high and low theta oscillations in the human hippocampus”. In: *Nature communications* 11.1, pp. 1–10.
- Greenberg, B. D. et al. (2006). “Three-year outcomes in deep brain stimulation for highly resistant obsessive–compulsive disorder”. In: *Neuropsychopharmacology* 31.11, pp. 2384–2393.
- Greiser, S. et al. (2015). “Results of the pilot assistance system “Assisted Low-Level Flight and Landing on Unprepared Landing Sites” obtained with the ACT/FHS research rotorcraft”. In: *Aerospace Science and Technology* 45, pp. 215–227.
- Griffiths, B. J. et al. (2019). “Directional coupling of slow and fast hippocampal gamma with neocortical alpha/beta oscillations in human episodic memory”. In: *Proceedings of the National Academy of Sciences* 116.43, pp. 21834–21842.
- Halevi, Y. (1994). “Stable LQG controllers”. In: *IEEE Transactions on Automatic Control* 39.10, pp. 2104–2106.

- Han, Y. et al. (2021). “Dynamic neural networks: A survey”. In: *IEEE Transactions on Pattern Analysis and Machine Intelligence*.
- Hasselmo, M. E. (2005). “What is the function of hippocampal theta rhythm?—Linking behavioral data to phasic properties of field potential and unit recording data”. In: *Hippocampus* 15.7, pp. 936–949.
- (2011). *How we remember: brain mechanisms of episodic memory*. MIT press.
- Hasselmo, M. E., C. Bodelón, and B. P. Wyble (2002). “A proposed function for hippocampal theta rhythm: separate phases of encoding and retrieval enhance reversal of prior learning”. In: *Neural computation* 14.4, pp. 793–817.
- Henderson, C. R. (1973). “Sire evaluation and genetic trends”. In: *Journal of Animal Science* 1973.Symposium, pp. 10–41.
- Henderson, I. and J. McGhee (1989). “Maxent binary identification of a warm air system”. In: *IMEKO Symposium on Microprocessors in Temperature and Thermal Measurement*.
- Herweg, N. A., E. A. Solomon, and M. J. Kahana (2020). “Theta oscillations in human memory”. In: *Trends in cognitive sciences* 24.3, pp. 208–227.
- Hescham, S. et al. (2013). “Deep brain stimulation of the forniceal area enhances memory functions in experimental dementia: the role of stimulation parameters”. In: *Brain stimulation* 6.1, pp. 72–77.
- Hickey, P. and M. Stacy (2016). “Deep brain stimulation: a paradigm shifting approach to treat Parkinson’s disease”. In: *Frontiers in neuroscience*, p. 173.
- Hill, P. F., D. R. King, et al. (2020). “Comparison of fMRI correlates of successful episodic memory encoding in temporal lobe epilepsy patients and healthy controls”. In: *Neuroimage* 207, p. 116397.
- Hill, P. F., S. E. Seger, et al. (2021). “Distinct neurophysiological correlates of the fMRI BOLD signal in the hippocampus and neocortex”. In: *Journal of Neuroscience* 41.29, pp. 6343–6352.

- Hoang, K. B. et al. (2017). “Biomarkers and stimulation algorithms for adaptive brain stimulation”. In: *Frontiers in Neuroscience* 11, p. 564.
- Hodgkin, A. L. and A. F. Huxley (1952). “A quantitative description of membrane current and its application to conduction and excitation in nerve”. In: *The Journal of physiology* 117.4, p. 500.
- Hornberger, M. and O. Piguet (2012). “Episodic memory in frontotemporal dementia: a critical review”. In: *Brain* 135.3, pp. 678–692.
- Hyman, J. M. et al. (2005). “Medial prefrontal cortex cells show dynamic modulation with the hippocampal theta rhythm dependent on behavior”. In: *Hippocampus* 15.6, pp. 739–749.
- Insausti, R. et al. (2019). “Cytoarchitectonic Areas of the Gyrus ambiens in the Human Brain”. In: *Frontiers in neuroanatomy* 13, p. 21.
- Izhikevich, E. M. (2007). *Dynamical systems in neuroscience*. MIT press.
- Jacobs, J. (2014). “Hippocampal theta oscillations are slower in humans than in rodents: implications for models of spatial navigation and memory”. In: *Philosophical Transactions of the Royal Society B: Biological Sciences* 369.1635, p. 20130304.
- Jacobs, J., B. Lega, and A. J. Watrous (2017). “Human hippocampal theta oscillations: distinctive features and interspecies commonalities”. In: *The hippocampus from cells to systems*. Springer, pp. 37–67.
- Jacobs, J., J. Miller, et al. (2016). “Direct electrical stimulation of the human entorhinal region and hippocampus impairs memory”. In: *Neuron* 92.5, pp. 983–990.
- Jansen, B. H. and V. G. Rit (1995). “Electroencephalogram and visual evoked potential generation in a mathematical model of coupled cortical columns”. In: *Biological cybernetics* 73.4, pp. 357–366.
- Jantz, J., A. Molnar, and R. Alcaide (2017). “A brain-computer interface for extended reality interfaces”. In: *ACM SIGGRAPH 2017 VR Village*, pp. 1–2.

- Jensen, O. and J. E. Lisman (2000). “Position reconstruction from an ensemble of hippocampal place cells: contribution of theta phase coding”. In: *Journal of neurophysiology* 83.5, pp. 2602–2609.
- Jeong, J. (2004). “EEG dynamics in patients with Alzheimer’s disease”. In: *Clinical neurophysiology* 115.7, pp. 1490–1505.
- Jones, M. W. and M. A. Wilson (2005). “Phase precession of medial prefrontal cortical activity relative to the hippocampal theta rhythm”. In: *Hippocampus* 15.7, pp. 867–873.
- Kailath, T. (1998). *Linear Systems*. Prentice-Hall information and system sciences series. Prentice Hall International.
- Kannathal, N. et al. (2005). “Characterization of EEG—a comparative study”. In: *Computer methods and Programs in Biomedicine* 80.1, pp. 17–23.
- Kay, S. M. (1988). *Modern Spectral Estimation*. Prentice Hall.
- Kerr, K. M. et al. (2007). “Functional neuroanatomy of the parahippocampal region: the lateral and medial entorhinal areas”. In: *Hippocampus* 17.9, pp. 697–708.
- Khalsa, S. et al. (2014). “The structural and functional connectivity of the posterior cingulate cortex: Comparison between deterministic and probabilistic tractography for the investigation of structure–function relationships”. In: *Neuroimage* 102, pp. 118–127.
- Klimesch, W. (1999). “EEG alpha and theta oscillations reflect cognitive and memory performance: a review and analysis”. In: *Brain research reviews* 29.2-3, pp. 169–195.
- Knierim, J. J. (2015). “The hippocampus”. In: *Current Biology* 25.23, R1116–R1121.
- Kota, S., M. D. Rugg, and B. C. Lega (2020). “Hippocampal theta oscillations support successful associative memory formation”. In: *Journal of Neuroscience* 40.49, pp. 9507–9518.
- Kringelbach, M. L. et al. (2007). “Translational principles of deep brain stimulation”. In: *Nature Reviews Neuroscience* 8.8, pp. 623–635.
- Kucewicz, M. T. et al. (2018). “Evidence for verbal memory enhancement with electrical brain stimulation in the lateral temporal cortex”. In: *Brain* 141.4, pp. 971–978.

- Lachaux, J.-P. et al. (1999). “Measuring phase synchrony in brain signals”. In: *Human brain mapping* 8.4, pp. 194–208.
- Lakatos, P. et al. (2005). “An oscillatory hierarchy controlling neuronal excitability and stimulus processing in the auditory cortex”. In: *Journal of neurophysiology* 94.3, pp. 1904–1911.
- Lamus, C. et al. (2012). “A spatiotemporal dynamic distributed solution to the MEG inverse problem”. In: *NeuroImage* 63.2, pp. 894–909.
- Laxton, A. W. and A. M. Lozano (2013). “Deep brain stimulation for the treatment of Alzheimer disease and dementias”. In: *World neurosurgery* 80.3-4, S28–e1.
- Laxton, A. W., D. F. Tang-Wai, et al. (2010). “A phase I trial of deep brain stimulation of memory circuits in Alzheimer’s disease”. In: *Annals of neurology* 68.4, pp. 521–534.
- Lega, B., J. Burke, et al. (2014). “Slow-theta-to-gamma phase–amplitude coupling in human hippocampus supports the formation of new episodic memories”. In: *Cerebral Cortex* 26.1, pp. 268–278.
- Lega, B., J. Germi, and M. D. Rugg (2017). “Modulation of oscillatory power and connectivity in the human posterior cingulate cortex supports the encoding and retrieval of episodic memories”. In: *Journal of cognitive neuroscience* 29.8, pp. 1415–1432.
- Lega, B. C., C. H. Halpern, et al. (2010). “Deep brain stimulation in the treatment of refractory epilepsy: update on current data and future directions”. In: *Neurobiology of disease* 38.3, pp. 354–360.
- Lega, B. C., J. Jacobs, and M. Kahana (2012). “Human hippocampal theta oscillations and the formation of episodic memories”. In: *Hippocampus* 22.4, pp. 748–761.
- Lega, B. C., M. Kahana, et al. (2011). “Neuronal and oscillatory activity during reward processing in the human ventral striatum”. In: *Neuroreport* 22.16, p. 795.
- Leontaritis, I. and S. A. Billings (1985). “Input-output parametric models for non-linear systems part I: deterministic non-linear systems”. In: *International journal of control* 41.2, pp. 303–328.

- Lilly, J. M. and S. C. Olhede (2012). “Generalized Morse wavelets as a superfamily of analytic wavelets”. In: *IEEE Transactions on Signal Processing* 60.11, pp. 6036–6041.
- Lin, J.-J., M. D. Rugg, et al. (2017). “Theta band power increases in the posterior hippocampus predict successful episodic memory encoding in humans”. In: *Hippocampus* 27.10, pp. 1040–1053.
- Lin, J.-J., G. Umbach, et al. (2019). “Gamma oscillations during episodic memory processing provide evidence for functional specialization in the longitudinal axis of the human hippocampus”. In: *Hippocampus* 29.2, pp. 68–72.
- Lisman, J. E. and O. Jensen (2013). “The theta-gamma neural code”. In: *Neuron* 77.6, pp. 1002–1016.
- Ljung, L. (2020). *System Identification Toolbox User’s Guide*. MathWorks.
- Ljung, L. (1999). *System Identification (2nd Ed.): Theory for the User*. USA: Prentice Hall PTR.
- (2007). *Practical issues of system identification*. Linköping University Electronic Press.
- Lozano, A. M. et al. (2016). “A phase II study of fornix deep brain stimulation in mild Alzheimer’s disease”. In: *Journal of Alzheimer’s Disease* 54.2, pp. 777–787.
- Lozano-Soldevilla, D., N. ter Huurne, and R. Oostenveld (2016). “Neuronal oscillations with non-sinusoidal morphology produce spurious phase-to-amplitude coupling and directionality”. In: *Frontiers in computational neuroscience* 10, p. 87.
- Maass, A. et al. (2015). “Functional subregions of the human entorhinal cortex”. In: *Elife* 4, e06426.
- MacDonald, D. B. (2002). “Safety of intraoperative transcranial electrical stimulation motor evoked potential monitoring”. In: *Journal of clinical neurophysiology* 19.5, pp. 416–429.
- MacKay, D. J. (1992). “Bayesian interpolation”. In: *Neural computation* 4.3, pp. 415–447.
- Malone Jr, D. A. et al. (2009). “Deep brain stimulation of the ventral capsule/ventral striatum for treatment-resistant depression”. In: *Biological psychiatry* 65.4, pp. 267–275.

- Mankin, E. A. and I. Fried (2020). “Modulation of Human Memory by Deep Brain Stimulation of the Entorhinal-Hippocampal Circuitry”. In: *Neuron* 106.2, pp. 218–235.
- Manning, J. R. et al. (2011). “Oscillatory patterns in temporal lobe reveal context reinstatement during memory search”. In: *Proceedings of the National Academy of Sciences* 108.31, pp. 12893–12897.
- Manns, J. R. et al. (2007). “Hippocampal CA1 spiking during encoding and retrieval: relation to theta phase”. In: *Neurobiology of learning and memory* 87.1, pp. 9–20.
- Marinescu, R. et al. (2019). “BrainPainter: A software for the visualisation of brain structures, biomarkers and associated pathological processes”. In: *arXiv preprint arXiv:1905.08627*.
- MathWorks (2020). *MATLAB System Identification Toolbox 2020a*. Natick, Massachusetts: The MathWorks Inc.
- Mayberg, H. S. et al. (2005). “Deep brain stimulation for treatment-resistant depression”. In: *Neuron* 45.5, pp. 651–660.
- McNaughton, N., M. Ruan, and M.-A. Woodnorth (2006). “Restoring theta-like rhythmicity in rats restores initial learning in the Morris water maze”. In: *Hippocampus* 16.12, pp. 1102–1110.
- Menezes Jr, J. M. P. and G. A. Barreto (2008). “Long-term time series prediction with the NARX network: An empirical evaluation”. In: *Neurocomputing* 71.16-18, pp. 3335–3343.
- Miao, B., R. Zane, and D. Maksimovic (2005). “System identification of power converters with digital control through cross-correlation methods”. In: *IEEE Transactions on Power Electronics* 20.5, pp. 1093–1099.
- Miller, J. et al. (2018). “Lateralized hippocampal oscillations underlie distinct aspects of human spatial memory and navigation”. In: *Nature communications* 9.1, pp. 1–12.
- Miranda, R. A. et al. (2015). “DARPA-funded efforts in the development of novel brain–computer interface technologies”. In: *Journal of neuroscience methods* 244, pp. 52–67.

- Møller, A. R. (1986). “Systems identification using pseudorandom noise applied to a sensorineural system”. In: *Computers & Mathematics with Applications* 12.6, pp. 803–814.
- Monmasson, E. et al. (2011). “FPGAs in industrial control applications”. In: *IEEE Transactions on Industrial informatics* 7.2, pp. 224–243.
- Mormann, F. et al. (2005). “Phase/amplitude reset and theta–gamma interaction in the human medial temporal lobe during a continuous word recognition memory task”. In: *Hippocampus* 15.7, pp. 890–900.
- Musk, E. et al. (2019). “An integrated brain-machine interface platform with thousands of channels”. In: *Journal of medical Internet research* 21.10, e16194.
- Natu, V. S. et al. (2019). “Stimulation of the posterior cingulate cortex impairs episodic memory encoding”. In: *Journal of Neuroscience* 39.36, pp. 7173–7182.
- Negrón-Oyarzo, I. et al. (2018). “Coordinated prefrontal–hippocampal activity and navigation strategy-related prefrontal firing during spatial memory formation”. In: *Proceedings of the National Academy of Sciences* 115.27, pp. 7123–7128.
- Ngo, H.-V. V. et al. (2013). “Auditory closed-loop stimulation of the sleep slow oscillation enhances memory”. In: *Neuron* 78.3, pp. 545–553.
- Nolde, S. F., M. K. Johnson, and C. L. Raye (1998). “The role of prefrontal cortex during tests of episodic memory”. In: *Trends in cognitive sciences* 2.10, pp. 399–406.
- Norgaard, M. et al. (2000). *Neural networks for modelling and control of dynamic systems: a practitioner’s handbook*. Springer.
- Norman, K. A. and R. C. O’Reilly (2003). “Modeling hippocampal and neocortical contributions to recognition memory: a complementary-learning-systems approach.” In: *Psychological review* 110.4, p. 611.
- Nune, G. et al. (2019). “Treatment of drug-resistant epilepsy in patients with periventricular nodular heterotopia using RNS® System: Efficacy and description of

- chronic electrophysiological recordings”. In: *Clinical Neurophysiology* 130.8, pp. 1196–1207.
- Nyhus, E. and T. Curran (2010). “Functional role of gamma and theta oscillations in episodic memory”. In: *Neuroscience & Biobehavioral Reviews* 34.7, pp. 1023–1035.
- Ojemann, G. A., N. F. Ramsey, and J. Ojemann (2013). “Relation between functional magnetic resonance imaging (fMRI) and single neuron, local field potential (LFP) and electrocorticography (ECoG) activity in human cortex”. In: *Frontiers in human neuroscience* 7, p. 34.
- Onslow, A. C., R. Bogacz, and M. W. Jones (2011). “Quantifying phase–amplitude coupling in neuronal network oscillations”. In: *Progress in biophysics and molecular biology* 105.1-2, pp. 49–57.
- Oppenheim, A. V. and R. W. Shafer (1989). *Discrete-Time Signal Processing*. Prentice Hall.
- Oppenheim, A. V., N. S. Hamid, and A. S. Willsky (1997). *Fourier series representation of periodic signals*. Prentice Hall.
- Osipova, D. et al. (2006). “Theta and gamma oscillations predict encoding and retrieval of declarative memory”. In: *Journal of neuroscience* 26.28, pp. 7523–7531.
- Oxley, T. J., N. L. Opie, et al. (2016). “Minimally invasive endovascular stent-electrode array for high-fidelity, chronic recordings of cortical neural activity”. In: *Nature biotechnology* 34.3, pp. 320–327.
- Oxley, T. J., P. E. Yoo, et al. (2021). “Motor neuroprosthesis implanted with neurointerventional surgery improves capacity for activities of daily living tasks in severe paralysis: first in-human experience”. In: *Journal of neurointerventional surgery* 13.2, pp. 102–108.
- Paller, K. A. and A. D. Wagner (2002). “Observing the transformation of experience into memory”. In: *Trends in cognitive sciences* 6.2, pp. 93–102.

- Perlmutter, J. S. and J. W. Mink (2006). “Deep brain stimulation”. In: *Annu. Rev. Neurosci.* 29, pp. 229–257.
- Pinheiro, J. C. and D. M. Bates (1996). “Unconstrained parametrizations for variance-covariance matrices”. In: *Statistics and computing* 6.3, pp. 289–296.
- Poppenk, J. et al. (2013). “Long-axis specialization of the human hippocampus”. In: *Trends in cognitive sciences* 17.5, pp. 230–240.
- Pradhan, C. et al. (2012). “Higher-order spectrum in understanding nonlinearity in EEG rhythms”. In: *Computational and mathematical methods in medicine* 2012.
- Preston, A. R. and H. Eichenbaum (2013). “Interplay of hippocampus and prefrontal cortex in memory”. In: *Current Biology* 23.17, R764–R773.
- Price, G. W. and R. Togneri (2012). “System identification of the EEG transformation due to TMS pulses: a novel method for a synchronous brain computer interface.” In: *2012 Spring Congress on Engineering and Technology*. IEEE, pp. 1–5.
- Rami, M. A. and X. Y. Zhou (2000). “Linear matrix inequalities, Riccati equations, and indefinite stochastic linear quadratic controls”. In: *IEEE Transactions on Automatic Control* 45.6, pp. 1131–1143.
- Ranganath, C. and M. Ritchey (2012). “Two cortical systems for memory-guided behaviour”. In: *Nature Reviews Neuroscience* 13.10, pp. 713–726.
- Richman, J. S. and J. R. Moorman (2000). “Physiological time-series analysis using approximate entropy and sample entropy”. In: *American Journal of Physiology-Heart and Circulatory Physiology* 278.6, H2039–H2049.
- Ritchey, M., L. A. Libby, and C. Ranganath (2015). “Cortico-hippocampal systems involved in memory and cognition: the PMAT framework”. In: *Progress in brain research*. Vol. 219. Elsevier, pp. 45–64.
- Robinson, J. et al. (2016). “Optogenetic activation of septal glutamatergic neurons drive hippocampal theta rhythms”. In: *Journal of Neuroscience* 36.10, pp. 3016–3023.

- Rosenblum, M. G. and A. S. Pikovsky (2004). “Controlling synchronization in an ensemble of globally coupled oscillators”. In: *Physical Review Letters* 92.11, p. 114102.
- Rutishauser, U., I. B. Ross, et al. (2010). “Human memory strength is predicted by theta-frequency phase-locking of single neurons”. In: *Nature* 464.7290, p. 903.
- Rutishauser, U., S. Ye, et al. (2015). “Representation of retrieval confidence by single neurons in the human medial temporal lobe”. In: *Nature neuroscience* 18.7, pp. 1041–1050.
- Santaniello, S. et al. (2015). “Therapeutic mechanisms of high-frequency stimulation in Parkinson’s disease and neural restoration via loop-based reinforcement”. In: *Proceedings of the National Academy of Sciences* 112.6, E586–E595.
- Schlichting, M. L. and A. R. Preston (2015). “Memory integration: neural mechanisms and implications for behavior”. In: *Current opinion in behavioral sciences* 1, pp. 1–8.
- Schomburg, E. W. et al. (2014). “Theta phase segregation of input-specific gamma patterns in entorhinal-hippocampal networks”. In: *Neuron* 84.2, pp. 470–485.
- Scoville, W. B. and B. Milner (1957). “Loss of recent memory after bilateral hippocampal lesions”. In: *Journal of neurology, neurosurgery, and psychiatry* 20.1, p. 11.
- Sederberg, P. B., L. V. Gauthier, et al. (2006). “Oscillatory correlates of the primacy effect in episodic memory”. In: *NeuroImage* 32.3, pp. 1422–1431.
- Sederberg, P. B., M. J. Kahana, et al. (2003a). “Theta and gamma oscillations during encoding predict subsequent recall”. In: *Journal of Neuroscience* 23.34, pp. 10809–10814.
- (2003b). “Theta and gamma oscillations during encoding predict subsequent recall”. In: *Journal of Neuroscience* 23.34, pp. 10809–10814.
- Sederberg, P. B., A. Schulze-Bonhage, et al. (2007). “Hippocampal and neocortical gamma oscillations predict memory formation in humans”. In: *Cerebral Cortex* 17.5, pp. 1190–1196.

- Shallice, T. and E. K. Warrington (1970). “Independent functioning of verbal memory stores: A neuropsychological study”. In: *The Quarterly journal of experimental psychology* 22.2, pp. 261–273.
- Shaneshi, M. M. (2019). “Brain–machine interfaces from motor to mood”. In: *Nature neuroscience* 22.10, pp. 1554–1564.
- Shirvalkar, P. R., P. R. Rapp, and M. L. Shapiro (2010). “Bidirectional changes to hippocampal theta–gamma comodulation predict memory for recent spatial episodes”. In: *Proceedings of the National Academy of Sciences* 107.15, pp. 7054–7059.
- Siapas, A. G., E. V. Lubenov, and M. A. Wilson (2005). “Prefrontal phase locking to hippocampal theta oscillations”. In: *Neuron* 46.1, pp. 141–151.
- Skarpaas, T. L., B. Jarosiewicz, and M. J. Morrell (2019). “Brain-responsive neurostimulation for epilepsy (RNS® System)”. In: *Epilepsy research* 153, pp. 68–70.
- Solomon, E. et al. (2017). “Widespread theta synchrony and high-frequency desynchronization underlies enhanced cognition”. In: *Nature communications* 8.1, pp. 1–14.
- Sols, I. et al. (2017). “Event boundaries trigger rapid memory reinstatement of the prior events to promote their representation in long-term memory”. In: *Current Biology* 27.22, pp. 3499–3504.
- Squire, L. R. (1992). “Memory and the hippocampus: a synthesis from findings with rats, monkeys, and humans.” In: *Psychological review* 99.2, p. 195.
- Sritharan, D. and S. V. Sarma (2014). “Fragility in dynamic networks: application to neural networks in the epileptic cortex”. In: *Neural computation* 26.10, pp. 2294–2327.
- Stam, C. et al. (1996). “Diagnostic usefulness of linear and nonlinear quantitative EEG analysis in Alzheimer’s disease”. In: *Clinical Electroencephalography* 27.2, pp. 69–77.
- Stam, C. J. (2005). “Nonlinear dynamical analysis of EEG and MEG: review of an emerging field”. In: *Clinical neurophysiology* 116.10, pp. 2266–2301.

- Staudigl, T. and S. Hanslmayr (2013). “Theta oscillations at encoding mediate the context-dependent nature of human episodic memory”. In: *Current biology* 23.12, pp. 1101–1106.
- Steinvorth, S. et al. (2010). “Human entorhinal gamma and theta oscillations selective for remote autobiographical memory”. In: *Hippocampus* 20.1, pp. 166–173.
- Stephan, K. E. et al. (2010). “Ten simple rules for dynamic causal modeling”. In: *Neuroimage* 49.4, pp. 3099–3109.
- Stone, S. S., C. M. Teixeira, L. M. DeVito, et al. (2011). “Stimulation of entorhinal cortex promotes adult neurogenesis and facilitates spatial memory”. In: *Journal of Neuroscience* 31.38, pp. 13469–13484.
- Stone, S. S., C. M. Teixeira, K. Zaslavsky, et al. (2011). “Functional convergence of developmentally and adult-generated granule cells in dentate gyrus circuits supporting hippocampus-dependent memory”. In: *Hippocampus* 21.12, pp. 1348–1362.
- Suthana, N. et al. (2012). “Memory enhancement and deep-brain stimulation of the entorhinal area”. In: *New England Journal of Medicine* 366.6, pp. 502–510.
- Tinkhauser, G. et al. (2017). “The modulatory effect of adaptive deep brain stimulation on beta bursts in Parkinson’s disease”. In: *Brain* 140.4, pp. 1053–1067.
- Toda, H. et al. (2008). “The regulation of adult rodent hippocampal neurogenesis by deep brain stimulation”. In: *Journal of neurosurgery* 108.1, pp. 132–138.
- Tort, A. B., R. Komorowski, et al. (2010). “Measuring phase-amplitude coupling between neuronal oscillations of different frequencies”. In: *Journal of neurophysiology* 104.2, pp. 1195–1210.
- Tort, A. B., R. W. Komorowski, et al. (2009). “Theta–gamma coupling increases during the learning of item–context associations”. In: *Proceedings of the National Academy of Sciences* 106.49, pp. 20942–20947.
- Tsao, A. et al. (2018). “Integrating time from experience in the lateral entorhinal cortex”. In: *Nature* 561.7721, pp. 57–62.

- Tsuda, M., Y. Lang, and H. Wu (2014). “Analysis and identification of the EEG signals from visual stimulation”. In: *Procedia Computer Science* 35, pp. 1292–1299.
- Tulleken, H. J. (1990). “Generalized binary noise test-signal concept for improved identification-experiment design”. In: *Automatica* 26.1, pp. 37–49.
- Tulleken, H. (1988). “A generalised binary noise test-signal concept for improved identification-experiment design”. In: *IFAC Proceedings Volumes* 21.9, pp. 577–585.
- Tulving, E. (1972). “12. Episodic and Semantic Memory”. In: *Organization of memory/Eds E. Tulving, W. Donaldson, NY: Academic Press*, pp. 381–403.
- (1983). “Elements of episodic memory”. In:
- (2002). “Episodic memory: From mind to brain”. In: *Annual review of psychology* 53.1, pp. 1–25.
- Turnbull, I. M. et al. (1985). “Stimulation of the basal nucleus of Meynert in senile dementia of Alzheimer’s type”. In: *Stereotactic and Functional Neurosurgery* 48.1-6, pp. 216–221.
- Umbach, G. et al. (2020). “Time cells in the human hippocampus and entorhinal cortex support episodic memory”. In: *bioRxiv*.
- Van den Bos, A. (1967). “Construction of binary multifrequency test signals”. In: *Proc. 1st IFAC Symp. on System Identification in Automatic Control Systems*.
- Vaz, A. P. et al. (2017). “Dual origins of measured phase-amplitude coupling reveal distinct neural mechanisms underlying episodic memory in the human cortex”. In: *Neuroimage* 148, pp. 148–159.
- Vidal, J. J. (1977). “Real-time detection of brain events in EEG”. In: *Proceedings of the IEEE* 65.5, pp. 633–641.
- Vidal, J. J. and V. JJ (1973). “Toward direct brain-computer communication”. In:
- Vugt, M. K. van et al. (2010). “Hippocampal gamma oscillations increase with memory load”. In: *Journal of Neuroscience* 30.7, pp. 2694–2699.

- Wagner, A. D. et al. (2005). “Parietal lobe contributions to episodic memory retrieval”. In: *Trends in cognitive sciences* 9.9, pp. 445–453.
- Wang, D. X. and C. E. Davila (2019). “Subspace averaging of auditory evoked potentials”. In: *2019 41st Annual International Conference of the IEEE Engineering in Medicine and Biology Society (EMBC)*. IEEE, pp. 656–659.
- Wang, D. X., K. Schmitt, et al. (2021). “Cross-regional phase amplitude coupling supports the encoding of episodic memories”. In: *Hippocampus* 31.5, pp. 481–492.
- Watrous, A. J. et al. (2013). “A comparative study of human and rat hippocampal low-frequency oscillations during spatial navigation”. In: *Hippocampus* 23.8, pp. 656–661.
- Wechsler, D. (1945). “Wechsler memory scale.” In:
- Wheeler, M. A., D. T. Stuss, and E. Tulving (1995). “Frontal lobe damage produces episodic memory impairment”. In: *Journal of the International Neuropsychological Society* 1.6, pp. 525–536.
- (1997). “Toward a theory of episodic memory: the frontal lobes and autonoetic consciousness.” In: *Psychological bulletin* 121.3, p. 331.
- Witter, M. P. et al. (2000). “Anatomical organization of the parahippocampal-hippocampal network”. In: *Annals of the New York Academy of Sciences* 911.1, pp. 1–24.
- Xie, H., H. Tang, and Y.-H. Liao (2009). “Time series prediction based on NARX neural networks: An advanced approach”. In: *2009 International conference on machine learning and cybernetics*. Vol. 3. IEEE, pp. 1275–1279.
- Yang, Y., A. T. Connolly, and M. M. Shanechi (2018). “A control-theoretic system identification framework and a real-time closed-loop clinical simulation testbed for electrical brain stimulation”. In: *Journal of neural engineering* 15.6, p. 066007.
- Yang, Y., S. Qiao, et al. (2021). “Modelling and prediction of the dynamic responses of large-scale brain networks during direct electrical stimulation”. In: *Nature biomedical engineering* 5.4, pp. 324–345.

- Yao, M. et al. (2021). “Temporal-wise Attention Spiking Neural Networks for Event Streams Classification”. In: *Proceedings of the IEEE/CVF International Conference on Computer Vision*, pp. 10221–10230.
- Yonelinas, A. P. et al. (2005). “Separating the brain regions involved in recollection and familiarity in recognition memory”. In: *Journal of Neuroscience* 25.11, pp. 3002–3008.
- Young, T. et al. (2018). “Recent trends in deep learning based natural language processing”. In: *ieee Computational intelligence magazine* 13.3, pp. 55–75.
- Zelmann, R. et al. (2020). “CLoSES: A platform for closed-loop intracranial stimulation in humans”. In: *NeuroImage* 223, p. 117314.
- Zhang, H. and J. Jacobs (2015). “Traveling theta waves in the human hippocampus”. In: *Journal of Neuroscience* 35.36, pp. 12477–12487.
- Zhou, C. et al. (2018). “A systematic review and meta-analysis of deep brain stimulation in treatment-resistant depression”. In: *Progress in Neuro-Psychopharmacology and Biological Psychiatry* 82, pp. 224–232.
- Ziegler, J. G., N. B. Nichols, et al. (1942). “Optimum settings for automatic controllers”. In: *trans. ASME* 64.11.
- Zion-Golumbic, E., M. Kutas, and S. Bentin (2010). “Neural dynamics associated with semantic and episodic memory for faces: evidence from multiple frequency bands”. In: *Journal of Cognitive Neuroscience* 22.2, pp. 263–277.